Quantum Tunnelling and Disorder in Two-Dimensional Ultracold Bose Gases



Erik Rydow

Somerville College

University of Oxford

A thesis submitted for the degree of

Doctor of Philosophy

Trinity 2026

Abstract

Thermal fluctuations, the microscopic fluctuations of things due to their temperature, counteract order in many-body systems. Thermal fluctuations often lead to high-temperature disordered phases and low-temperature ordered ones. In lower dimensions, thermal fluctuations are relatively stronger with two-dimensional materials being just on the brink of thermal fluctuations destroying their order. Two-dimensional materials therefore display unique behaviour, for example undergoing a superfluid phase transition driven by point-like topological defects.

In this work, we realise two-dimensional bosonic quantum gases of the isotope Rb-87 in precisely controlled potentials to study how quantum-tunnelling and spatially disordered potentials affect the phases of matter they form. We also present a new scheme for cooling quantum gases directly in the finely tuned radio-frequency-dressed traps confining the gases in our experiments.

To study tunnel-coupled gases, this work utilises a novel method to read out information from bilayer quantum gas experiments by analysing noise patterns arising from interference effects. We find that quantum-tunnelling between the two layers in a bilayer system can cause both layers to remain superfluid at higher temperatures than without quantum tunnelling. We compare our results to predictions using renormalisation-group theory and numerical simulations. We experimentally observe the predicted double-layer superfluid phase, a novel phase where the U(1) symmetry of the relative phase is broken and relative excitations are suppressed.

Separately, we investigate the topological Berezinskii-Kosterlitz-Thouless phase transition in disordered two-dimensional Bose gases. We find that such systems can be driven across this phase transition by increasing the strength of an applied disordered potential. We experimentally map out the phase diagram for a continuous 2D Bose gas in the presence of disorder, which has not previously been carried out to the best of our knowledge. We find that the presence of disorder increases the number of topological defects at a given temperature while reducing the rate at which the number of defects increases with temperature. The experimental results for 2D disordered Bose gases are in qualitative agreement with numerical simulations for the parameter regime studied.

The following publications include work to which I contributed during my DPhil research:

- **E. Rydow**, V. Singh, A. Beregi, E. Chang, L. Mathey, C. Foot, S. Sunami, "Observation of a Bilayer Superfluid with Interlayer Coherence"
  Nature Communications 16 7201 (2025).

- S. Sunami, V. Singh, **E. Rydow**, A. Beregi, E. Chang, L. Mathey, C. Foot, "Detecting Phase Coherence of 2D Bose Gases via Noise Correlations."
  Physical Review Letters 134 (2025): 183407.

- M. Sesodia, S. Sunami, E. Chang, **E. Rydow**, C. Foot, A. Beregi. "CNN-Based Vortex Detection in Atomic 2D Bose Gases in the Presence of a Phononic Background"
  Machine Learning: Science and Technology 6.1 (2025): 015067.

- E. Chang, V. Singh, A. Beregi, **E. Rydow**, C. Foot, S. Sunami, "Coupling-induced universal dynamics in bilayer two-dimensional Bose gases" arXiv preprint arXiv:2510.23600 (2025).

- A. Beregi, E. Chang, **E. Rydow**, C. Foot, S. Sunami, "Universal non-Gaussian order parameter statistics in two-dimensional superfluids" arXiv preprint arXiv:2601.16204 (2026).

Acknowledgements

I would first like to thank my supervisor Professor Christopher Foot for taking me on as a student and for the support and guidance as well as independence he has provided throughout the DPhil. I have been fortunate to get to work alongside the incredible people in his ultracold matter research group. I would like to especially acknowledge Abel Beregi for teaching me the ropes; his knowledge, enthusiasm, and seemingly infinite patience, made it a joy to be in the lab throughout. It was also a privilege to work with En 'Oscar' Chang, his meticulous attention to detail and wish to dig deep into the theoretical details of the physics was always enjoyable and served as an inspiration. I am also grateful to Abel and Oscar for generously taking their time to help troubleshoot some of the more interesting issues with the experiment.

I would also like to thank Shinichi Sunami for his guidance both with research questions and paper writing, data analysis and for encouraging me to study bilayers and density noise. It has also been great to work with the younger graduate students, Yao-Chih Kuo and Ziyue Jin, who I am sure will take the work much further. Apart from the people on the Rb-experiment, my other colleagues in the office, Jesse Schelfhout and Kenneth Hughes also made my time as a DPhil student enjoyable.

In addition, I want to thank our theory collaborators especially Ludwig Mathey and Vijay Singh. I am also grateful for the discussions with John Chalker who graciously offered some of his time to help us with the theoretical interpretation of our results. Furthermore, the ongoing collaboration with Taufiq Murthado has been enjoyable and illuminating.

However, none of this work would have been accomplished without the support I received from my family, in particular my parents, Jonas and Lena and my grandparents. Especially my maternal grandfather Ulf who always encouraged my curiosity. I also want to thank my brother Thomas who kept my spirits high.

Finally, I would like to thank Beatrice for her unwavering encouragement and support throughout the DPhil and many years before.

Contents

List of Figures **8**

1 Introduction **11**

1.1 Contents of the Thesis 12

2 Preparation of Ultracold Bose Gases **16**

2.1 Experimental Sequences 16

2.2 RF-dressed Traps 21

2.2.1 Multiple-RF dressed potentials 24

3 Evaporative cooling to quantum degeneracy in an RF-dressed potential **26**

3.1 Results 27

3.2 Conclusion 32

4 Two-dimensional Bose Gases **34**

4.1 Statistical Mechanics in Two-dimensions 34

4.1.1 Degenerate Bose gases 36

4.1.2 The Berezinskii-Kosterlitz-Thouless transition 37

4.1.3 Renormalisation-group theory 40

4.2 Numerical Methods 43

4.2.1 Monte Carlo and the Metropolis algorithm 43

5 Density Noise Readout **47**

5.1 Motivation 48

5.2 Experimental Readout from Density Noise 50

5.2.1 Noise correlations of expanded bilayer 2D Bose gases 53
5.2.2 Experimental results 57
5.3 Outlook 63
5.3.1 Reconstruction using images at different times 63

6 Coupled Two-Dimensional Bilayers **65**
6.1 Theoretical Background 66
6.1.1 Renormalisation-group analysis 68
6.2 Experimental Procedure 70
6.3 Results 74
6.4 Summary 77
6.5 Experimental Details 80
6.5.1 Experimentally realising ultracold bilayers 80
6.5.2 Image analysis for relative-phase detection 82
6.5.3 Image analysis for common-phase detection 84
6.5.4 Estimation of Josephson coupling J 86
6.5.5 Monte Carlo simulation of tunnel-coupled bilayers 86

7 Implementing a Speckle Disorder Potential **89**
7.1 Implementing a Repeatable Speckle Potential 89
7.1.1 Speckle patterns 90
7.1.2 Stick-slip servo 92
7.1.3 Optical setup for green light 94
7.1.4 Characterising the optical speckle potential 94
7.1.5 Characterising the disorder strength 96

8 Disordered Bose Gases **101**
8.1 Theory of Disordered Bose Gases 101
8.2 Experimental Results 105
8.3 Numerical Simulations 113
8.4 Summary and Outlook 119

9 Conclusion and Outlook **121**

Appendices

A Detailed Bilayer Density Noise Calculation **125**

A.0.1 Simplifying Out-of-plane Components 129

A.0.2 Effect of Relative Phase 132

A.0.3 Change of Integration Variables 135

References **137**

List of Figures

2.1 Illustration of the stages in the experimental sequence of the older generation apparatus. 17
2.2 Illustration of the stages in the experimental sequence of the new apparatus. 17
2.3 Example of a numerically computed MRF-potential. 25

3.1 Evaporative cooling in an RF-dressed potential. 28
3.2 Evaporative cooling ramp. 31
3.3 Matter-wave interference fringes from shell condensed degenerate Bose gas. 33

5.1 Illustration of relation between density noise and phase gradients. . 50
5.2 Noise interferometry of 2D Bose gases. 52
5.3 Effect of relative mode phase fluctuations on density noise. 58
5.4 Expansion scaling behaviour. 60
5.5 Noise correlations of single layer and bilayer 2D Bose gases across the BKT transition. 61
5.6 The BKT crossover in 2D Bose gases. 62

6.1 Renormalisation-group results for the phase stiffness in bilayers. . . 70
6.2 Formation of a bilayer quasi-2D Bose gas and its characterisation by matter-wave interferometry. 73
6.3 Phase coherence of the relative mode in the coupled bilayer. 75
6.4 Phase coherence of the common mode. 77
6.5 Phase diagram of the coupled bilayer 2D Bose gas. 78
6.6 Vortex suppression in the relative mode. 79

6.7 Matter-wave interference patterns and their spectra 83
6.8 Density noise-correlation functions across the critical point. 85
6.9 Analysis of numerical simulations 88

7.1 The rotation mount used to allow for distinct and repeatable disorder realisations. 92
7.2 In-situ density distribution with 10 different instances of the speckle pattern disorder. 93
7.3 Schematic showing power modulation of blue detuned beams used for optical potential. 94
7.4 Image of speckle pattern generated with diffusive plate. 95
7.5 Spatial correlation of the speckle pattern. 95
7.6 Distinct speckle realisations. 96
7.7 Relation between the amplitude of the AOM driving frequency and the power in the beam going to the diffusive plate to generate the disorder potential. 97
7.8 Example of speckle pattern generated numerically. 98
7.9 Simulation results for the change in kinetic energy imparted when pulsing a speckle potential. 99
7.10 Effect of initial temperature on the potential strength calibration. . 100
7.11 Experimental results for the change in temperature when pulsing a speckle potential. 100

8.1 Illustration of the effect of disorder on bosons and their eigenenergy spectra. 103
8.2 Thermodynamic properties of gas when varying the disorder strength and temperature. 106
8.3 Region of temperature and disorder phase diagram probed. 107
8.4 Phase correlation functions, g_1, when varying temperature and disorder strength. 108
8.5 Algebraic and exponential decay rates of g_1 functions 109

8.6 Compilation of the different signals indicating superfluid or normal regime. 110
8.7 Phase identification shown in terms of thermodynamic variables. . . 111
8.8 Effect of disorder strength on vortex density. 111
8.9 Vortex proliferation rate as a function of disorder strength. 112
8.10 Thermodynamic properties of the Monte Carlo simulated fields. . . 114
8.11 Phase correlation functions from simulations, g_1, when varying PSD and disorder strength. 115
8.12 Algebraic and exponential decay rates of g_1 functions 116
8.13 Different signals indicating superfluid or normal regime from simulation. 117
8.14 Effect of disorder strength on vortex number from simulation. . . . 118
8.15 Vortex decay exponent with increasing PSD as a function of disorder strength from simulation. 118

A.1 The term in Eq. A.33, approximations in Eq. A.37 and Eq. A.39 evaluated and compared for 7000 relative phase profiles in the superfluid regime. 134
A.2 The term in Eq. A.33, approximations in Eq. A.37 and Eq. A.39 evaluated and compared for 500 relative phase profiles from Monte Carlo simulations in the normal regime. 134

1 Introduction

It is famously difficult to precisely predict the behaviour of more than a few interacting particles. In general, even just three objects interacting gravitationally give rise to chaotic and intractable dynamics. Despite this, it is possible to make confident predictions of the collective properties such as temperature and pressure for systems made up of large numbers of particles. Translating between the microscopic laws governing the constituents of a system, such as the atoms in a material, and their collective properties relies upon physically motivated approximations. Experiments are therefore imperative to study novel physical systems with many interacting parts, both to ascertain the emergent properties such as phases of matter and to inform theoretical predictions.

Ultracold gas experiments are excellent for realising prototypical examples of physical systems with many interacting parts. These experiments provide a tuneable platform for studying many-body physics in an idealised setting. Ultracold gas experiments can be used to study the effect of cleanly varying select properties of a system over a large range as such tunability can be difficult to achieve for the solid samples studied in more traditional condensed matter experiments.

The study of ultracold gases began with Bose and Einstein's prediction that when gases of indistinguishable particles are cooled to very low temperatures the lowest energy quantum state will be occupied by a macroscopic number of particles [1,

2]. Indistinguishable particles that can occupy the same quantum state are called bosons and the state of matter where a macroscopic number of bosons occupy the same quantum state is called a Bose-Einstein condensate. Following the theoretical prediction of Bose-Einstein condensates, significant experimental refinement was required to reach the low temperatures where such condensation occurs. The first Bose-Einstein condensation of a dilute atomic gas was achieved in 1995 when a gas of ^{87}Rb was cooled to a temperature below 170 nK [3]. The quantum-wave nature of Bose-Einstein condensates being a macroscopically occupied quantum state manifests in experiments in that spatially separated condensates produce interference fringes when they overlap, analogous to those in Young's double-slit experiment [4]. Matter-wave interference between Bose-Einstein condensates provides a versatile experimental technique for probing their properties [5, 6].

Cold atomic gas experiments provide a platform for engineering and probing many-body physical systems with desirable properties. Crucially, the behaviour of ultracold gases can be understood within the framework of the laws of quantum mechanics, where in many important cases exact calculations using this physical theory for large numbers of particles become prohibitively computationally expensive. Ultracold gas experiments are therefore a powerful experimental tool for investigating how quantum mechanical effects, such as quantum tunnelling, and disorder-induced localisation, affects the collective properties of many-body systems.

1.1 Contents of the Thesis

This work studies properties of two-dimensional bosonic many-body quantum systems. Two-dimensional systems are of interest since the effect of thermal fluctuations, the microscopic fluctuations of things due to their temperature, get relatively stronger in lower dimensions. Thermal fluctuations act to prevent systems from becoming ordered and often lead to high-temperature disordered phases and low-temperature ordered ones, for example ice having an ordered crystal structure while liquid water does not. Two-dimensional materials can be just at the brink of thermal fluctuations destroying their order even at $T = 0$ and

therefore display unique behaviour. Additionally, topology, the mathematics of continuously deformable shapes, plays a unique role in two-dimensional systems. In systems with two spatial dimensions and a time-dimension, one-dimensional objects can form knots as they evolve, whereas in 3+1D all knots are trivial [7]. A hallmark of two-dimensional systems are excitations in the form of topological defects, e.g. vortices with a quantised flow around them. Thermally excited topological defects cause certain two-dimensional systems to feature a distinct type of phase transition unique to two-dimensions. This 'topological phase transition' is called the Berezinskii-Kosterlitz-Thouless phase transition.

In general, two-dimensional materials can feature unique properties. Graphene, an atomic monolayer of graphite and the subject of the 2010 Nobel Prize in Physics, might be the most well known. In addition to single layers of two-dimensional materials, bilayer systems where two two-dimensional materials interact along their surfaces have been found to exhibit interesting emergent properties. One such bilayer-system is twisted-bilayer graphene, where two layers of graphene placed above one another become superconducting only if there is a precise angle between the two layers [8]. Two-dimensional planes in the crystal structure of some high-temperature superconductors also form bilayer systems [9]. Quantum tunnelling between such planes is a mechanism of interest for certain superconducting materials, including materials whose superconducting properties are enhanced when illuminated with a laser [10, 11].

In addition to the unique behaviour of two-dimensional systems, we are interested in the collective properties of particles in spatially disordered potentials. Quantum mechanics leads to behaviour fundamentally different from classical physics in how disorder affects particles. Most strikingly, a single quantum particle can be trapped in a spatially disordered energy landscape even if a classical particle would not. This stems from the fact that a classical particle having a well defined position and momentum will move in only one direction at every instant. On the other hand, wave-particle duality causes a quantum particle to evolve as a wavepacket; spreading out in every direction. When this quantum wave reflects off and diffracts

around the disorder at different locations it can lead to destructive interference at long distances, localising the wave and therefore the particle. In two-dimensional many-body systems the interplay between the disorder-induced localisation and the topological phase transition is expected to lead to rich behaviour [12].

In the experiments reported in this thesis we modify the potentials experienced by the atoms in two-dimensional ultracold gases of bosons to experimentally map out the phase diagram of two types of many-body quantum systems. The systems we study using ultracold gas experiments are: two-dimensional bilayers of bosons with tunable quantum tunnelling between the layers, and two-dimensional layers of bosons in spatially disordered potentials.

Apart from engineering the ultracold gases to display novel behaviour, probing the gases in our experiments to obtain useful information also presents an important challenge. This includes both inferring the collective properties of the gases and characterising the environment they experience giving rise to those properties.

In this thesis I present a novel theoretical and experimental technique allowing the statistics of excitations occurring in both layers of bilayer systems to be extracted from ultracold gas experiments. This new technique is used to study the symmetric and antisymmetric excitations as the propensity for particles to quantum mechanically tunnel between two two-dimensional layers is varied. In this experiment we identify a predicted double-layer superfluid phase, where the system is superfluid due to quantum tunnelling between the layers. In the double-layer superfluid phase quantum tunnelling breaks the $U(1)$ symmetry of the relative excitations, making the relative phase-field massive and suppressing relative excitations. In addition, we upgrade the experiment to generate statistically equivalent, but distinct and repeatable, disordered potentials. We use this new experimental capability to study how the presence of a spatially disordered potential affects the properties of two-dimensional bosonic systems, specifically how it affects the Berezinskii-Kosterlitz-Thouless phase transition.

The thesis is structured as follows, in Ch. 2 we describe the techniques employed in our two separate experimental apparatus to cool and trap the gases to realise

the ultracold quantum gases. Ch. 3 details a novel method for cooling the gas to quantum degeneracy in our new apparatus and characterising the excitations in the resulting clouds. Ch. 4 contains background on the behaviour of Bose gases in two-dimensions and the topological Berezinskii-Kosterlitz-Thouless phase transition which is a feature of these systems. Ch. 5 introduces the novel readout method where we study the interference patterns of two-dimensional bilayers after a short period of free expansion to obtain information about the symmetric excitations in bilayer systems. In Ch. 6 we realise and study the phase diagram of two-dimensional bilayer systems where the strength of the tunnel-coupling between the layers is varied. Ch. 7 details how we implement our disordered potential and also how we characterise its statistical, spatial properties and its magnitude. Ch. 8 contains an experimental investigation of how disorder affects the properties of the system including when the two-dimensional system undergoes a phase transition this is compared to numerical simulations. Finally, Ch. 9 concludes with a summary of the findings and an outlook for future research.

2

Preparation of Ultracold Bose Gases

To perform experiments with cold atomic gases one needs methods to confine and cool them. This chapter outlines how this is done in the experimental apparatus used to obtain the data reported in this thesis. Two sets of apparatus were used, one called the 'previous generation apparatus' and one called the 'new generation apparatus'. In this chapter we provide an overview of how the experimental procedure differs between the older apparatus and the newer apparatus [13, 14] which is expanded upon in Ch. 3.

2.1 Experimental Sequences

The experimental results reported in Ch. 5, Ch. 6 and Ch. 8 were obtained using the previous generation experiment described in earlier theses [13–17]. The capabilities of this apparatus were upgraded with the ability to realise a set of distinct disordered potentials as described in Ch. 7. The older experiment features a sequence of optical cooling and trapping methods followed by magnetic ones, with the approximate: timing, temperature and atom number, summarised in Fig. 2.1. Fig. 2.1 aims to convey the stages of the experimental sequence that is currently used on the older experiment as well as when various cooling and trapping techniques are applied.

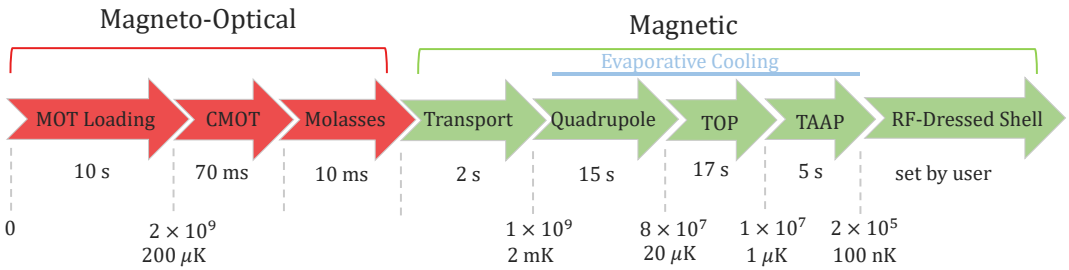


Figure 2.1: Illustration of the stages in the experimental sequence as currently used on the older generation apparatus. The figure shows the approximate atom numbers and temperatures at the main stages of the sequence, alongside the duration of the different stages (the numbers are ballpark estimates as precise values depend both on the degree of optimisation and the physics studied). A quantum degenerate Bose gas is achieved at the end of the interval marked as evaporative cooling which takes place for the duration indicated by the blue line.

In addition to using the previous generation apparatus in the sections listed above, work was also performed on the continued construction of a newer apparatus. This is something earlier students initiated and the plan is described in Abel Beregi's thesis [18] with early stages of construction described in David Garrick's thesis [13]. The new apparatus utilises a conceptually simpler experimental sequence to create Bose-Einstein condensates, shown pictorially in Fig. 2.2.

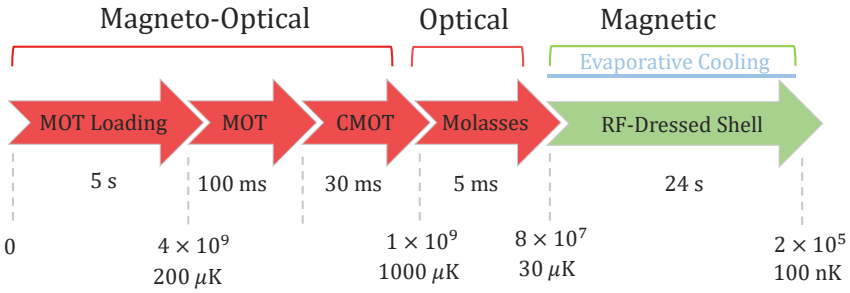


Figure 2.2: Illustration of the stages in the experimental sequence of the new apparatus. The figure shows the approximate atom number and temperature at the main stages of the sequence, below the associated steps alongside the duration of the different steps, the numbers are ballpark estimates as precise values depend both on the degree of optimisation and the physics studied. A degenerate Bose gas is obtained at the end of the stage marked RF-dressed shell where the evaporative cooling ends.

The new apparatus is described further in Ch. 3 where the advantages of its simplified experimental sequences are discussed.

The different stages shown in Fig. 2.1 and Fig. 2.2 are covered in detail in previous theses from the group [15, 16, 18, 19]. As such, we just provide an overview of principles behind the different steps in the experimental sequences here, noting that extensive detail can be found in earlier work.

Magneto-Optical Trap (MOT)

Both experiments realise a MOT using laser beams with a mix of light driving the $F = 2 \rightarrow F' = 3$, cooling transition and $F = 1 \rightarrow F' = 2$ repumping transition of the D_2 line of ^{87}Rb. A MOT uses pairs of counter-propagating laser beams along each spatial direction with frequencies below the transition to apply a velocity dependent force (as for atoms moving towards a beam the frequency of the light is Doppler-shifted and closer to the transition) slowing the atoms, alongside a non-uniform magnetic field to confine the atoms. A MOT therefore both cools and confines atoms. The cooling in a MOT is limited by the linewidth of the cooling transition Γ. The lowest possible temperature is called the Doppler-limit which is given by $T_D = \hbar\Gamma/2k_B$. For ^{87}Rb the natural linewidth of the D_2 line, used in this work, gives a Doppler-limit temperature of $T_D = 146\,\mu$K [20].

In the old apparatus the 6 MOT beams are generated by illuminating a pyramidal mirror with a large, 5 cm diameter, beam with a power of 300 mW, with the cooling component being frequency detuned by 22 MHz [16] below the transition and static magnetic quadrupole field

$$\boldsymbol{B} = B'(x\hat{\boldsymbol{e}}_x + y\hat{\boldsymbol{e}}_y + 2z\hat{\boldsymbol{e}}_z) \tag{2.1}$$

with a gradient (in the weaker radial direction) of $B' = 13.9\,$G/cm [15]. From first order perturbation theory the energies of the different Zeeman states are

$$E_{M_F} = M_F g_F \mu_B |\boldsymbol{B}| \tag{2.2}$$

in terms of the Landé g-factor, g_F and the Bohr magneton μ_B. In the new experiment the MOT is realised using the traditional configuration with 6 counter-propagating beams, each having an intensity of 5 mW with a magnetic quadrupole gradient of

$B' = 21\,\mathrm{G/cm}$ [18]. These 6 MOT beams are power stabilised using proportional-integral-derivative (PID) loops controlling LCD wave-plates [18].

Compressed Magneto-Optical Trap (CMOT)

A compressed magneto-optical trap, where the magnetic field and the detuning of the cooling light in a MOT are ramped over a short period of time is used in both experiments to increase the density of the atomic clouds. In the older experiment the CMOT is achieved by increasing the frequency detuning to $-74\,\mathrm{MHz}$ to decrease the re-radiation of resonant photons causing heating and expansion. Alongside the increased detuning the quadrupole gradient is reduced to $5\,\mathrm{G/cm}$ to allow sub-Doppler mechanisms to act over a larger region. In the new experiment the CMOT is realised by ramping the radial quadrupole gradient and frequency detunings non-linearly, going from the quadrupole gradient in the MOT to $100\,\mathrm{G/cm}$ and then further up to $200\,\mathrm{G/cm}$ and back down again to $29\,\mathrm{G/cm}$ to compress the MOT, while the detuning is ramped from $20\,\mathrm{MHz}$ to $40\,\mathrm{MHz}$ and then down to $20\,\mathrm{MHz}$. The non-linear CMOT ramp for the new experiment was found using the Gaussian optimisation machine learning protocol described in Abel Beregi's DPhil thesis [18].

Optical Molasses

Optical molasses is a laser cooling technique which works best without the presence of a magnetic field, or with only a weak non-uniform magnetic field $B < 0.1\,\mathrm{G}$. Optical molasses allows for laser cooling to temperatures below the Doppler-limit set by the transition linewidth [21, 22]. On the older experiment the pyramidal mirror and lack of suitable bias fields mean that the beam powers cannot be balanced to the degree needed for an optimal molasses without bias fields. As such in the older experiment the magnetic quadrupole field is kept on but at a low value to achieve additional cooling [15]. The 6 beam configuration on the new experiment does allow for sufficient power balancing to realise a sub-Doppler optical molasses when no current is driven through the quadrupole coils and the bias coils are set to cancel out static stray magnetic fields.

Magnetic Transport

On the older experiment a magnetic transport rail *(Parker Hannifin 404 XR)* holding coils in an anti-Helmholtz configuration [15] creates a magnetic quadrupole trapping the atoms. The magnetic transport rail on which the coils are mounted moves the atoms from the side of the experiment containing the atomic source to the ultra-high vacuum (UHV) science side. The process of moving the atoms into and out of the quadrupole trap in the moving stage as well as to shift their vertical position while the magnetic transport stage is travelling requires precise timing of the currents passing through several auxiliary coils, as described in Tiffany Harte's thesis [16]. The currents passing through these coils are optimised using a machine learning algorithm (Bayesian optimisation) to maximise the number of atoms which arrive at the UHV side.

There is substantial heating and atom loss during the magnetic transport which increases the subsequent amount of cooling required in the magnetic trap. However, a significant advantage of a transport stage is that it allows for only using magnetic trapping and cooling in the UHV science glass cell meaning that the optical access around the cell is not reduced by the laser beams needed for optical cooling and trapping.

Quadrupole Trap

The quadrupole trap on the older experiment is implemented using anti-Helmholtz coils surrounding the UHV science cell. This confines the atoms in the low-field seeking states to near the minimum of the quadrupole and the evaporative cooling starts in this trap. The evaporative cooling is implemented by applying an RF field to drive transitions of energetic atoms at the edges of the cloud to the untrapped state. The selective removal of the energetic atoms lowers the temperature of the remaining gas and is discussed further in Ch. 3.

Time-Orbiting Potential (TOP) Trap

Spin-flip losses occurring near the minimum of the magnetic quadrupole field become problematic as the atoms get colder and thus are more likely to be in the low magnetic field region. One way to avoid this is the time-orbiting potential (TOP) trap, in which bias fields move the quadrupole field minimum in a circle in the horizontal plane with a frequency of 7 kHz. This orbiting frequency is lower than the Larmor frequency meaning the internal states of atoms follow the field adiabatically but greater than the atomic motion, which results in the atoms experiencing an effective time-averaged potential where they do not spend significant time in the region where the magnetic field is weak and they would be likely to spin-flip and become untrapped.

Time-averaged Adiabatic Potential (TAAP) Trap

The time-averaged adiabatic potential is formed by combining an RF-dressed shell as described below, with time-varying bias fields as in the TOP trap. The TAAP was proposed in Ref. [23] and demonstrated in Ref. [24]. It was found to be advantageous for evaporative cooling because it offers high collision rates due to high radial trap frequencies [17], a TAAP also provides a natural way to go between the TOP and RF-dressed shell traps used for our science applications. The older generation experiment produces a degenerate Bose gas via evaporative cooling in a TAAP trap, the condensate is then loaded into the RF-dressed shell trap, by ramping down the rotating bias field.

2.2 RF-dressed Traps

At the end of the preparation using either of the two different series of cooling stages shown in Fig. 2.1 or Fig. 2.2 we produce a degenerate Bose gas confined in a radio-frequency (RF) dressed potential.

RF-dressed traps were proposed by Oliver Zobay and Barry Garraway [25]. They feature both a static and an oscillating magnetic field which together allow for trapping along an iso-magnetic surface away from the minima of the static magnetic

field. Due to the iso-magnetic trapping surface which is topologically equivalent to a sphere such traps are also referred to as 'bubble traps' [26], or 'shell traps'.

Consider an oscillating magnetic field

$$\boldsymbol{B}_{RF} = \boldsymbol{B}_{RF_0}\cos(\omega t). \tag{2.3}$$

where the magnetic dipole selection rules, relevant for RF fields, are [27]

$$\Delta F = 0, \pm 1 \text{ (but not } 0 \to 0), \tag{2.4}$$

$$\Delta M_F = 0, \pm 1 \ (\Delta F = 0 = \Delta M_F \text{ gives no transition}). \tag{2.5}$$

As such we will consider ^{87}Rb, $F = 1$, as this is the state the atoms in our experiment decay to without the repumping light. The dressed-atom picture considers the Hamiltonian consisting of the sum of the atomic internal energy, the RF field mode energy, and the atom-RF-field mode coupling [28]

$$H = H_A + H_L + H_{AL}. \tag{2.6}$$

Where

$$\hat{H}_A = \mu_B g_F B_0 \hat{F}_z, \tag{2.7}$$

$$H_L = \hbar\omega(\hat{a}^\dagger\hat{a} + \frac{1}{2}), \tag{2.8}$$

with $\hat{F}_z$ being the operator for the total angular momentum along the z-direction, which we align with the direction of the static field $\boldsymbol{B_0}$ without loss of generality, and $\hat{a}^{(\dagger)}$ being the annihilation (creation) operators for the radiation field. Thus it is apparent that in the absence of atom-light interaction the eigenstates will be tensor products of the M_f states $|M_f = 0, \pm 1\rangle$ and the number states of the radiation field $|N\rangle$. These are called 'dressed states' and will be grouped according to N, and separated by $\hbar\omega$ [28]. The dressed states can be labelled as $|N, M_F\rangle$. The atom-RF interaction will connect dressed states which differ by the number of absorbed photons and corresponding angular momentum depending on the polarization.

For an RF field interacting with the lower hyperfine level of ^{87}Rb the atom-light term can be written as

$$H_{AL} = \lambda_{\sigma^+}(\hat{F}_+\hat{a} + \hat{F}_-\hat{a}^\dagger) + \lambda_{\sigma^-}(\hat{F}_+\hat{a}^\dagger + \hat{F}_-\hat{a}) + \lambda_\pi\hat{F}_z(\hat{a}^\dagger + \hat{a}), \tag{2.9}$$

where the coefficients $\lambda_{\sigma^-}, \lambda_{\sigma^+}, \lambda_\pi$ depend on the polarization and population of the RF field [19], and $\hat{F}_\pm = \hat{F}_x \pm i\hat{F}_y$. To diagonalise the Hamiltonian exactly with this interaction within the subspace of a manifold of coupled states we consider only the example of a circularly polarised RF field. This leaves

$$H = \mu_B g_F B_0 \hat{F}_z + \hbar\omega(\hat{a}^\dagger \hat{a} + \frac{1}{2}) + \lambda_{\sigma^-}(\hat{F}_+ \hat{a}^\dagger + \hat{F}_- \hat{a}). \tag{2.10}$$

It is clear the eigenstates of this will be a linear combination of the dressed states $|N+1,+1\rangle, |N,0\rangle, |N-1,-1\rangle$. We therefore diagonalise the Hamiltonian in this subspace, ignoring multi-photon processes which couple different manifolds. In this basis the Hamiltonian acts on the basis states as

$$\begin{aligned}
\hat{H}|N+1,1\rangle &= \mu_B g_F B_0 |N+1,1\rangle + \hbar\omega(N+1-\frac{1}{2})|N+1,1\rangle + \lambda_{\sigma^-}\sqrt{2}\sqrt{N+1}\,|N,0\rangle, \\
\hat{H}|N,0\rangle &= \hbar\omega(N-\frac{1}{2})|N,0\rangle + \lambda_{\sigma^-}\sqrt{2}\sqrt{N+1}\,|N+1,1\rangle + \lambda_{\sigma^-}\sqrt{2}\sqrt{N}\,|N-1,-1\rangle, \\
\hat{H}|N-1,-1\rangle &= -\mu_B g_F B_0 |N-1,-1\rangle + \hbar\omega(N-1-\frac{1}{2})|N-1,-1\rangle + \lambda_{\sigma^-}\sqrt{2}\sqrt{N}\,|N,0\rangle.
\end{aligned}$$

Giving the Hamiltonian in matrix representation as

$$H = \begin{pmatrix} \mu_B g_F B_0 + \hbar\omega(N+\frac{3}{2}) & \lambda_{\sigma^-}\sqrt{2}\sqrt{N+1} & 0 \\ \lambda_{\sigma^-}\sqrt{2}\sqrt{N+1} & \hbar\omega(N+\frac{1}{2}) & \lambda_{\sigma^-}\sqrt{2}\sqrt{N} \\ 0 & \lambda_{\sigma^-}\sqrt{2}\sqrt{N} & -\mu_B g_F B_0 + \hbar\omega(N-\frac{1}{2}) \end{pmatrix}. \tag{2.11}$$

Making the approximation of large photon populations $\sqrt{N} \approx \sqrt{N+1}$, ignoring the constant zero-point energy offset of the photon field, and parametrising the detuning as $\delta = \omega - \mu_B g_F B_0/\hbar$, the Hamiltonian can be written as

$$H = \begin{pmatrix} \hbar\omega N + \delta & \lambda_{\sigma^-}\sqrt{2N} & 0 \\ \lambda_{\sigma^-}\sqrt{2N} & \hbar\omega N & \lambda_{\sigma^-}\sqrt{2N} \\ 0 & \lambda_{\sigma^-}\sqrt{2N} & \hbar\omega N - \delta \end{pmatrix}. \tag{2.12}$$

We identify the Rabi frequency as $\Omega = 2\lambda_{\sigma^-}\sqrt{N}$ and the eigenenergies of Eq. 2.12 are

$$E_{\tilde{N},\tilde{M}_F} = \tilde{N}\hbar\omega + \tilde{M}_F \hbar\sqrt{\delta^2 + \Omega^2}. \tag{2.13}$$

Where $\tilde{N} \in \mathbb{N}$ and $\tilde{M}_F \in \{-1, 0, +1\}$ label the new eigenstates when including the atom-light interaction. The fact that states with $\tilde{M}_F = 1$ have a minimum of

energy where the magnetic field and frequency of the RF field gives $\delta = 0$ causes RF-dressed traps to confine atoms along an iso-magnetic surface away from the minimum of the static magnetic field. Due to gravity the atoms reside at the bottom of this trapping surface in our experiment.

2.2.1 Multiple-RF dressed potentials

To realise a double well configuration of the type used in the experimental work reported in this thesis, both to study bilayer physics and also for interferometric readout, we use multiple-RF dressed potentials. As the name implies, this refers to RF dressing with multiple tones in the RF field, where the intuition follows from the single tone case in Sec. 2.2 above. In analogy with the single-RF case in Eq. 2.13, each additional tone in the RF serves to add a 'bend' (avoided crossing) in the potential at a position determined by the frequency of the tone, as shown in Fig. 2.3. Thus one needs $2n-1$ tones in the RF to realise an MRF-dressed potential with n minima.

Analytical solutions are not generally possible in the case of multiple dressing frequencies, and we use Floquet techniques to numerically compute the potential for MRF dressing [16]. These techniques stipulate that for a Hamiltonian with a certain periodicity in time, the eigenstates must share this periodicity, in analogy with Bloch's theorem for periodicity in space [29].

Floquet's theorem states that if $H(t) = H(t+T)$, then

$$|\psi(t)\rangle = e^{iE't/\hbar} |\phi(t)\rangle \tag{2.14}$$

where $\phi(t) = \phi(t+T)$. The energies of the eigenstates can therefore be found by finding the eigenvalues of the time evolution operator evolving the state for an interval T

$$U(T) |\phi(0)\rangle = e^{iE'T/\hbar} |\phi(0)\rangle \,, \tag{2.15}$$

where we solve for the eigenvalues of $U(T)$ by time-evolving the dressed states for a period T numerically using the time-dependent Schrödinger equation. We then obtain $U(T)$ in the basis of dressed states. Since the eigenvalue of the $U(T)$ operator cannot depend on the basis, we obtain the eigenenergies E' by diagonalising the $U(T)$ we found in the basis of dressed states.

Thus, to use Floquet techniques we require that the different frequency components share a common denominator, i.e. that they are commensurate. There is a technical reason for using commensurate RF-dressing frequencies, namely that intermodulation products of non-commensurate RF components in the RF-amplifier create harmonics which cause atom loss [19]. These frequencies used in the experiment must be commensurate in binary when represented on the *AD9910* 14-bit DAC of the Sinara Urukul, which is the digital signal synthesizer we use for generating the RF field. For illustrative purposes Fig. 2.3 shows a numerically calculated potential for an MRF potential with frequency components 4.92 MHz, 5.02 MHz and 5.12 MHz.

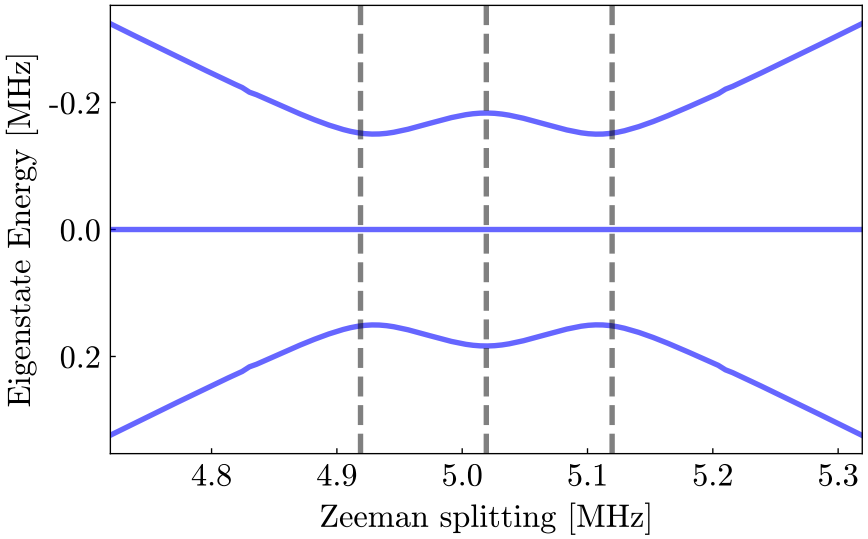


Figure 2.3: Example of a numerically computed MRF-potential. The black dashed lines indicate the values of the three frequency components in the dressing RF field.

3

Evaporative cooling to quantum degeneracy in an RF-dressed potential

Cold atomic gases have been proposed as a platform for a range of quantum technologies, such as sensing and quantum simulation. One reason for this is that when sufficiently cooled the collective properties of atomic gases are strongly affected by quantum mechanical effects. To manipulate and study such ultracold gases they must be held in place with the use of a so-called trap, examples of which are described in Ch. 2. The properties of the trap are chosen depending on the scientific application, for example sensing such as accelerometery relies on smooth finely tuned traps to infer the forces acting on the atoms from their velocity response, meanwhile in analogue quantum simulation smooth stable traps reduce the rate at which the atoms heat up in the trap; this heating rate limits the timescale on which ultracold gas experiments can study low-temperature quantum phenomena. As seen in Ch. 2 atoms tend to first be cooled using optical techniques such as magneto-optical traps and optical molasses. However, optical cooling techniques are generally not able to reach the low temperatures and high densities at which quantum degeneracy within a trapped gas becomes significant. To reach the low temperatures required the standard technique with a few exceptions [30, 31] is evaporative cooling, in which highly energetic atoms are selectively ejected from

the trap. In our case this is done by applying RF radiation, which we call the evaporative 'knife'. The remaining atoms have less energy on average and due to collisions they re-thermalise to a colder temperature.

RF dressing, as described in Sec. 2.2 is a popular technique for trapping atoms in a magnetic field as it allows for traps with smooth and controllable geometries. Among other things these precisely tunable potentials can be used to realise two-dimensional (2D) bubbles [14, 26, 32, 33] and tunable tunnel-coupling [34, 35] as in Ch. 6. In addition, the well characterised potentials are generated by macroscopic coils, and not significantly sensitive to microscopic alignment. To reach the low temperatures needed to create ultracold gases in the quantum degenerate regime in an RF-dressed trap one has hitherto had to rely on trapping methods in addition to RF dressing to confine the gas when performing evaporative cooling, as in our previous generation experiment shown in Fig. 2.1, with some results indicating that evaporation in RF-dressed traps is prohibitively inefficient due to ineffective thermalisation [36, 37]. When evaporatively cooling the atoms in a different trap from the RF-dressed trap used in the science application, loading the RF-dressed trap inevitably excites sloshing and breathing modes. Such excitations inject energy into the system and unavoidable random excitations generally detract from the scientific purpose of having well-controlled ultracold gases.

3.1 Results

In this chapter we outline, to the best of our knowledge, the first creation of a Bose-Einstein condensate (BEC) in a shell trap by performing evaporative cooling to quantum degeneracy entirely in an RF-dressed shell trap (work which was done together with Abel Beregi and is also outlined in his thesis [14]). In addition to the previously reported work using a circularly polarised RF field, where losses are expected to be lower [19], to form a shell, I achieved evaporative cooling to Bose condensation in a linearly polarised RF shell. The use of a linearly polarised shell facilitates significantly easier splitting of the condensate, and as a result we achieved the first splitting of the condensate in the new experiment. This allows us

to characterise the excited modes in the BEC prepared directly in the RF-dressed trap using matter-wave interferometric readout. We show that evaporating in the RF-dressed trap directly results in a three-dimensional condensate without the significant excitations stemming from loading the shell trap after evaporating in a different trap. The ability to realise cold atoms in tunable RF-dressed potentials with fewer excitations is a significant technical achievement with broad relevance for quantum technologies which utilise cold atoms. Ultracold gases with minimal excitations might for example be useful for proposals which leverage different phonon modes in BECs for sensing [38, 39].

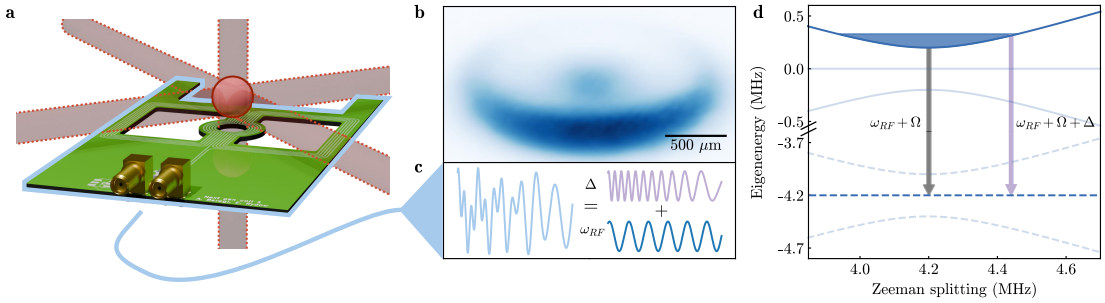


Figure 3.1: Evaporative cooling in an RF-dressed potential. a. The geometry of the trap, the location of the atoms in the magneto-optical trap and molasses is denoted by the sphere with a red outline in the centre, the MOT beams are shown with dashed red outlines. While not used during optical cooling and trapping the location of the printed circuit board (PCB) coil used for RF-dressing to create the shell trap is shown with a blue outline situated under the quadrupole node. **b**. Absorption image showing the atoms in the RF-dressed shell before evaporation, with the atoms trapped in the node of the quadrupole field visible in the centre of the shell. **c**. Schematic representation of the combined RF signal sent to the PCB coil for evaporative cooling, consisting of the dressing frequency ω_{RF} and the evaporation signal Δ. **d**. Diagram showing the dressed atom picture and the evaporation signal shown as a purple arrow, with dressed states corresponding to different numbers of photons absorbed separated by $\hbar\omega_{RF}$. The location occupied by the atoms in the shell is indicated by the blue shaded region.

In the new experimental apparatus, we load a three-dimensional (3D) MOT with ^{87}Rb using a 2D pyramidal source [40], we then perform a compressed MOT and optical molasses where the magnetic quadrupole field is turned off. The schematic of the optical trapping setup used to realise the MOT and optical molasses is shown schematically in Fig. 3.1a. After performing optical molasses the optical cooling and trapping is complete so the lasers are shuttered and the magnetic

quadrupole field is turned on again together with the dressing RF field to realise the RF-dressed trap. The oscillating RF-field is generated using a coil of the design shown in Fig. 3.1a. The RF dressing creates a smooth potential minimum around an iso-magnetic surface away from the minimum of the static magnetic field, as seen in Fig. 3.1b and d. The optically cooled atoms after they have been loaded into the RF-dressed shell can be seen in Fig. 3.1b, where the atoms located at the quadrupole node and in the shell are both visible. To apply the RF fields used for forming the shell trap and for applying the tone which acts as the RF knife during evaporative cooling, we use a coil made using a printed circuit board (PCB) as this results in an exact and stable geometry that is easy to simulate. These coils were designed by Abel Beregi and are described in more detail in his thesis [18]. The PCB coil is placed below the atoms. The RF field can be circularly or linearly polarized by applying fields along the x and y directions (horizontal plane) with a $\pi/2$ phase difference (giving $\cos(\omega t)$ and $\pm\sin(\omega t)$ respectively). However, using linear polarization easily facilitates the addition of more tones to modify the trap geometry. Adding the two additional tones needed to form a double well would require 3 more amplitudes and 3 more phases which need to be calibrated and controlled if using circular polarisation. When loaded into the shell trap the optically cooled atoms have a temperature on the order of a few tens of μK. We then add a second tone to our RF to act as an evaporative knife, as shown schematically in Fig. 3.1b. The frequency detuning of the RF knife during our evaporative ramp is shown in Fig. 3.2a. The RF knife selectively ejects the most energetic atoms during our evaporative cooling ramp, reducing both the atom number and the temperature, leading to Bose-Einstein condensation as seen in Fig. 3.2a.

The evaporative cooling of the atoms from $\sim$10 μK to the $\sim$100 nK required to form a condensate takes place over 24.3 s. The temperature, atom number and phase-space density evolve as seen in Fig. 3.2 during the evaporation ramp. The 3D phase-space density (PSD) is the number of particles within one unit volume of the thermal de Broglie wavelength $\lambda_{th} = \sqrt{2\pi\hbar^2/(mk_BT)}$, in terms of the reduced Planck constant $\hbar$, the Boltzmann constant k_B, the mass of the particles m and

temperature T. The phase-space density is therefore $D = n_{3D}\lambda_{th}^3$ where n_{3D} is the 3D number density of particles.

Evaporative cooling in an RF-dressed trap is significant as it was previously thought to be prohibitively inefficient [36]. The reason for this belief is that evaporative cooling in the shell trap suffers from a few fundamental inefficiencies. Firstly, to the lowest order, the trap is harmonic along all 3 spatial dimensions. The scaling of the density and the collision rate with atom number make harmonic potentials inferior to linear potentials realised in the quadrupole trap [41] for so-called 'runaway' evaporation since if the collision rate drops as evaporation proceeds then the process can fail to reach low temperatures. However this comparison must be considered carefully since in the hypothetical case of no other losses so that evaporation can take infinitely long then a harmonic trap conserves more atoms for a given temperature reduction. The efficiency of evaporative cooling is further reduced by the high trap anisotropy, as the atoms predominantly cross the evaporation surface along the vertical direction. This is expected to result in an effective evaporation dimension of one [42]. We characterise the evaporative cooling ramp in the following way. We release the atoms allowing them to expand freely for a time-of-flight (TOF) duration of $t_{\mathrm{TOF}} = 17\,\mathrm{ms}$ and then perform fitting with the theoretical model (sum of Thomas-Fermi distribution and a poly-logarithmic distribution [43]) of their spatial distribution at this time, as seen in Fig. 3.2a. Absorption images of the clouds after TOF at 40% through the evaporative ramp and at the end of the ramp are shown in the insets in Fig. 3.2a, the green and orange lines above the insets show the fitted theoretical models used to extract temperature and number of atoms from the clouds after the TOF expansion [18].

Fig. 3.2d shows a linear trend which implies an approximately constant value of $d(\log T)/d(\log N) = 1.00(1)$. As well as offering a simpler experimental protocol, evaporation in the RF-dressed shell trap has the great benefit of avoiding the excitations from transferring the condensate into the shell trap.

To study the long-range excitations in the condensate when evaporating in the dressed shell trap we performed matter-wave interferometry to study the phase

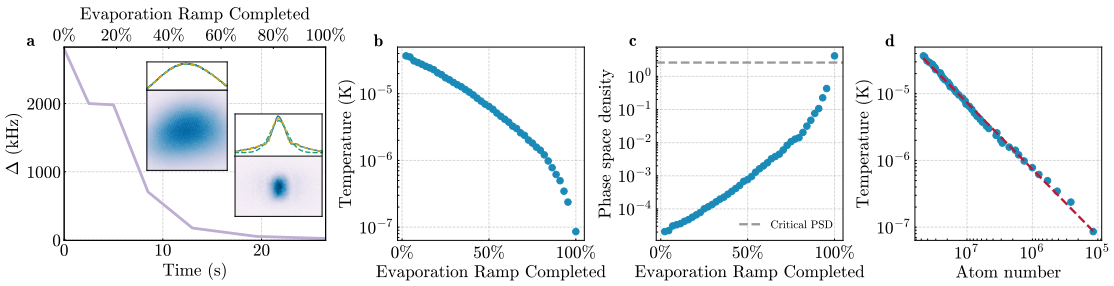


Figure 3.2: Evaporative cooling in a dressed RF potential. a. The frequency ramp of the evaporative signal over time, alongside TOF images of the atoms after 17 ms TOF at 40% through the evaporation ramp the distribution of which, shown above the image, is well fitted by the green poly-log fit and at the end of the evaporative cooling ramp, whose density distribution is instead fitted by the bimodal distribution shown by the orange line indicating that there is a significant degree of quantum degeneracy within the Bose gas. **b** and **c**, the temperature and phase-space density are shown as a function of the evaporation ramp percentage. **d**. Showing the evolution of temperature and atom number during the evaporative cooling to determine the evaporation efficiency, the dashed red line corresponds to a gradient of -1.

fluctuations in the degenerate cloud. This is done by adding two additional RF tones to realise a double-well potential, as described in Sec. 2.2.1, thus splitting the cloud in two. In this case the RF frequencies used to form the double well are: 4.92, 5.02 and 5.12 MHz. When the clouds are released and allowed to expand freely for 15 ms the relative phase fluctuations in-situ can be extracted from the phase fluctuations across the fringes as the density distribution after TOF has the form [43]

$$\rho_x(z) = \rho_0 \exp\left(-z^2/2\sigma^2\right)\left[1 + c_0 \cos(kz + \theta(x))\right]. \tag{3.1}$$

The phase $\theta(x)$ is extracted by taking the Fourier transform of each column of the image to obtain the phase [34]. The phase is extracted in this way within the central 50% of the Thomas-Fermi radius, to avoid fluctuations due to the reduced density near the edge of the cloud. The interference fringes after TOF expansion are shown in Fig. 3.3a, with the phase of the periodic interference pattern within the extracted range indicated with the red line. The apparent flatness of the fringes, seen from the small phase fluctuations corresponds to a lack of significant excitations within the condensates, as shown from the distribution of the phase profiles in Fig. 3.3b obtained from 150 repetitions of the experiment. As the Bose gas is three-dimensional in this case, the fluctuations arise from splitting

and are not inherent thermal fluctuations which would be present in 2D or 1D Bose gases. Fig. 3.3c shows the distribution of the standard deviation of the phase profiles shown in Fig. 3.3b. The exceptionally flat fringes showcase the suitability of using evaporative cooling in the RF-dressed shell trap for the preparation of atoms for precision interferometry measurements, thus presenting significant benefit for quantum simulation [44] and atom interferometry.

3.2 Conclusion

In this chapter we demonstrate the feasibility of using evaporative cooling to achieve a degenerate quantum gas in an RF-dressed quadrupole potential. Providing a novel way to prepare cold atoms in a well characterised smooth trap with minimal excitations. We highlight the advantages of this cooling technique by showing that the resulting condensates lack the long wavelength fluctuations arising from transferring the atoms following evaporation in another trap into an RF-dressed potential. Our result opens the way for simpler cold-atom apparatus as the evaporative cooling can be done with the same hardware as the trapping. Our results therefore represent a significant technical advance with direct relevance for quantum technologies which rely on ultracold atoms in dressed potentials, such as quantum simulation and sensing.

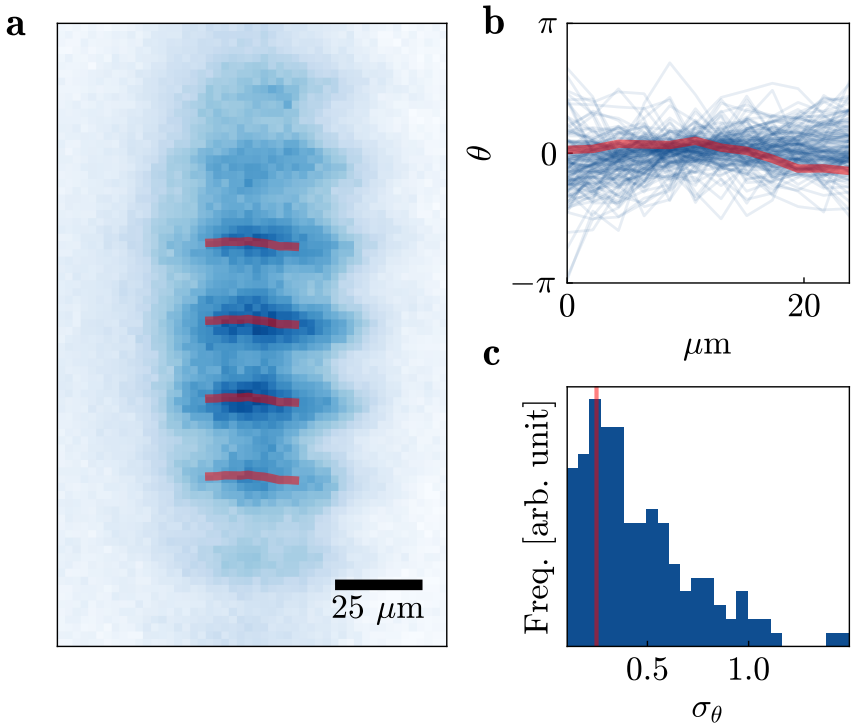


Figure 3.3: Matter-wave interference fringes from shell condensed degenerate Bose gas. a. Example of an absorption image showing matter-wave interference between two Bose gases, the phase of the interference fringes θ in the image is overlaid as red lines. **b.** The phase profiles $\theta(x)$ from 150 experimental repetitions with their mean subtracted to centre them around 0, the phase profile highlighted in panel a is once again highlighted in red. **c.** The distribution of the standard deviations of the 150 phase profiles shown in panel b, the red vertical line corresponds to the standard deviation of the highlighted phase profile shown in panels a and b.

4
Two-dimensional Bose Gases

This thesis concerns experimental investigations of bilayers of ultracold two-dimensional bosonic gases where much of the interesting behaviour arises from the low dimensionality of the systems. This chapter outlines the relevant phenomena emerging in two-dimensional systems and introduces background physics relevant to the experiments covered in Ch. 5, Ch. 6 and Ch. 8. The complex field description of Bose gases is introduced as well as the motivation behind the renormalisation-group theory used to interpret the experimental results in Ch. 6.

4.1 Statistical Mechanics in Two-dimensions

In two-dimensional systems with short-ranged interactions thermal fluctuations break continuous symmetries at any finite temperature: this is formalised as the Mermin-Wagner theorem. This stems from that in lower dimensions each point in a system will have fewer adjacent points and thus is expected to be less energetically constrained by its neighbours. The absence of spontaneous symmetry breaking of continuous symmetries in certain two-dimensional systems means that the standard Landau framework, in which phase transitions arise from spontaneous symmetry breaking does not fully capture phase transitions in two-dimensions. Phase transitions do still occur in two-dimensional systems with

continuous symmetries and short-range interactions, but they do not arise from symmetry-breaking, the phase transitions are instead topological in nature. The prototypical model for a two-dimensional system with a continuous symmetry which nonetheless undergoes a phase transition is the classical XY model. This classical spin model features spins of uniform magnitude, similar to the Ising model, but where each spin can point in any direction in a two-dimensional plane. There is an energy cost associated with spins being misaligned with their neighbours and the model is described by the Hamiltonian

$$H_{XY} = -J \sum_{\langle i,j \rangle} S_i \cdot S_j = -J \sum_{\langle i,j \rangle} cos(\theta_i - \theta_j) \tag{4.1}$$

where $\sum_{\langle i,j \rangle}$ denotes a sum over nearest neighbours. The two-dimensional XY model thus has a $U(1)$ symmetry. A relevant class of excitations for this Hamiltonian are smooth wavelike fluctuations, called phonons. These phonons are gapless in the limit of large system size. This is motivated by the fact that in lower dimensions long wavelength fluctuations cost little energy due to the reduced number of neighbours as the dimensionality decreases. To see this consider a two-dimensional system with N sites in each linear direction, with a slow precession of θ accumulating an angle of ϕ across the system, where we let ϕ be a free parameter which controls the rate of rotation of the spins from one side to another. Such a precession of the spins incurs an angular difference of ϕ/N at each site, so using the small angle approximation in Eq. 4.1 the deviation from the ground state energy caused by this long wavelength fluctuation is

$$E_{phonon} - E_0 = J \sum_{<i,j>} (\phi/N)^2 \propto N^2(\phi/N)^2 = \phi^2. \tag{4.2}$$

The energy cost of this long wavelength phononic excitation can therefore be chosen to be arbitrarily small but finite, making the phonons gapless. For a three-dimensional system the same analysis will give an energy for any long wavelength phonons proportional to the number of sites and thus diverges with system size, i.e. in the thermodynamic limit. As the phonon spectrum of the XY model in the thermodynamic limit is gapless, any finite energy density leads to

phonons being excited preventing the system from being in a perfectly ordered state at any finite temperature.

4.1.1 Degenerate Bose gases

In a degenerate Bose gas, a Bose-Einstein condensate, there is a macroscopic occupation of a single quantum state, as the bosonic particles in this state are identical and indistinguishable they must, from symmetry, have the same probability distribution - with the differing outcomes when observing the identical particles stemming purely from the probabilities inherent in quantum mechanics. Hence we associate a macroscopic condensate wavefunction with the bosons in the multiply occupied state. This wavefunction is a complex valued field, normalised to the total number of particles in the degenerate gas.

To arrive at a semi-classical theory it is customary to write the collective wavefunction in terms of real density $n(\boldsymbol{r})$ and phase $\theta(\boldsymbol{r})$ fields as

$$\Psi(\boldsymbol{r}) = \sqrt{n(\boldsymbol{r})}e^{i\theta(\boldsymbol{r})}. \tag{4.3}$$

The Hamiltonian for the macroscopic wavefunction contains a kinetic term, a potential term and a term associated with contact interactions and can be written as

$$H = \int dr \frac{\hbar^2}{2m}\nabla\Psi^*(\boldsymbol{r})\nabla\Psi(\boldsymbol{r}) + V(\boldsymbol{r})\Psi^*(\boldsymbol{r})\Psi(\boldsymbol{r}) + \frac{g}{2}\Psi^*(\boldsymbol{r})\Psi^*(\boldsymbol{r})\Psi(\boldsymbol{r})\Psi(\boldsymbol{r}). \tag{4.4}$$

The Hamiltonian has a $U(1)$ symmetry in that it is invariant under constant offsets of the complex phase of the macroscopic wavefunction. We often consider the case where the external potential is uniform,

$$H = \int dr^2 \frac{\hbar^2}{2m}\nabla\Psi^*(\boldsymbol{r})\nabla\Psi(\boldsymbol{r}) + \frac{g}{2}\Psi^*(\boldsymbol{r})\Psi^*(\boldsymbol{r})\Psi(\boldsymbol{r})\Psi(\boldsymbol{r}). \tag{4.5}$$

To see how the density is expected to behave we can consider fluctuations around the mean value $n(\boldsymbol{r}) = n(1 + 2\delta n(\boldsymbol{r}))$. Expanding around the mean density and assuming small density fluctuations we obtain

$$H = \int dr^2 \frac{n\hbar^2}{2m}(\nabla\theta(\boldsymbol{r}))^2 + \frac{n\hbar^2}{2m}(\nabla\delta n(\boldsymbol{r}))^2 + 2gn^2(\delta n(\boldsymbol{r}))^2. \tag{4.6}$$

A two-dimensional degenerate Bose gas has a characteristic small length-scale called the healing length $\xi = \hbar/\sqrt{ngm} = 1/\sqrt{\tilde{g}n}$ and a characteristic velocity given by the speed of sound $c = \sqrt{gn/m}$. From Eq. 4.6 one can read off that the energy is minimised when the density fluctuations vanish everywhere and that only gradients in the complex phase then affect the energy. By considering the Fourier transform of the phase and density fields and the equipartition theorem one sees that

$$\begin{aligned} \langle \theta_{\boldsymbol{k}}^2 \rangle &= k_B T (\tfrac{n\hbar^2}{2m}|k|^2)^{-1} \\ \langle \delta n_{\boldsymbol{k}}^2 \rangle &= k_B T (\tfrac{n\hbar^2}{2m}|k|^2 + 2gn^2)^{-1} \end{aligned} \quad . \tag{4.7}$$

This shows that density fluctuations are significantly suppressed compared to phase fluctuations for low energy and therefore long wavelength excitations. Hence the density is often approximated as constant at low temperatures. Making the constant density approximation we obtain

$$H = \int dr^2 \frac{n\hbar^2}{2m} (\nabla\theta(\boldsymbol{r}))^2. \tag{4.8}$$

Eq. 4.8 is the continuum form of the two-dimensional XY Hamiltonian in Eq. 4.1 making the identification $J = n\hbar^2/m$. This shows why two-dimensional degenerate Bose gases exhibit the physics of the two-dimensional XY model, with the angle of the spins being analogous to the values of the complex phase of the wavefunction.

4.1.2 The Berezinskii-Kosterlitz-Thouless transition

One of the most significant features of the two-dimensional XY model is that it undergoes a topological phase transition, called the Berezinskii-Kosterlitz-Thouless (BKT) transition. The BKT transition is a phase transition between a quasi-long-range ordered phase and a disordered phase. Unlike the phase-transitions due to symmetry-breaking described by Landau-theory there is no order parameter which is zero in the disordered phase and non-zero in the ordered phase in the BKT transition. The phases of either side of the BKT transition in the XY model are distinguished by the behaviour of the spin correlations, also called phase correlations, which are defined as

$$C(x, x') = \mathrm{Re}[\langle e^{i[\theta(x)-\theta(x')]} \rangle]. \tag{4.9}$$

In the case of a degenerate Bose gas, or the two-dimensional XY model, the phase correlations take two different functional forms corresponding to two distinct thermodynamic phases of the system. The functional forms are either algebraically decaying, or exponentially decaying, depending on if the temperature is below or above a critical temperature T_c.

$$C(\boldsymbol{r}) = \mathrm{Re}[\langle e^{i[\theta(\tilde{\boldsymbol{r}})-\theta(\boldsymbol{r})]}\rangle_{\tilde{\boldsymbol{r}}}] \sim \begin{cases} |\boldsymbol{r}|^{-\eta} & \text{if } T < T_c \text{ (quasi-long-range ordered phase)} \\ e^{-|\boldsymbol{r}|/r_0} & \text{if } T > T_c \text{ (disordered phase)} \end{cases}. \tag{4.10}$$

Here $\tilde{\boldsymbol{r}}$ is a spatial coordinate which is averaged over, η is the algebraic exponent, and r_0 is the correlation length. The mechanism behind the BKT transition is the proliferation of vortices, points in the system around which the spins in the two-dimensional XY model or the complex phase of the macroscopic wavefunction in a two-dimensional Bose gas winds by $\pm 2\pi$. The presence of these quantised vortices scrambles the phase, destroying the quasi-long-range order. Due to conservation of angular momentum, thermodynamic fluctuations can only create the vortices in pairs with opposite winding. Members of such pairs with opposite winding are conventionally called vortices and anti-vortices. The interaction energy between vortices falls off logarithmically with their separation. Furthermore, pairs with opposite vorticity attract and pairs with the same vorticity repel. This arises because when vortex-pairs with the same vorticity are closer to one another the superfluid flow/phase gradient between them increases, twisting the phase more rapidly and costing more energy, while the phase gradient between a vortex and an anti-vortex cancels to some extent, reducing the energy cost of a pair of vortices with the opposite circulation. The interactions between vortices and anti-vortices mimic those of a two-dimensional Coulomb gas. A simple argument motivating why there is a phase transition driven by vortices can be found by considering the probability of a configuration featuring a single isolated vortex anywhere in the system at a given temperature

$$P_{\text{vortex}} = \sum_{\text{configurations}} e^{-\beta E_{\text{vortex}}}, \tag{4.11}$$

expressed using the inverse temperature $\beta = 1/k_B T$. Considering the classical two-dimensional XY model on a lattice, with lattice spacing a and linear length L, there are $(L/a)^2$ equivalent micro-states where the vortex could be placed. This leads to a probability for a free vortex to exist anywhere in the system of

$$P_{\text{vortex}} = \Omega e^{-\beta E_{\text{vortex}}} = e^{-\beta(E_{\text{vortex}} + T k_B \ln(\Omega))} = e^{-\beta(E_{\text{vortex}} - TS)} = e^{-\beta F_{\text{vortex}}}. \quad (4.12)$$

Showing how the Helmholtz free energy, $F = E - TS$, captures the competition between entropy and energy as a function of temperature which underlies most classical phase-transitions, where there is often a low-temperature more ordered phase and a high-temperature less ordered phase. We can obtain an expression for the vortex energy by considering that for the phase to be well defined it must go from 0 to 2π when going around a circle at radius r from the core of a vortex. This gives $|\nabla\theta| = 2\pi/(2\pi r) = 1/r$ and hence an energy

$$E_{\text{vortex}} = \frac{n\hbar^2}{2m} \int_a^L dr 2\pi r \frac{1}{r^2} = \frac{n\hbar^2 \pi}{m} \ln\left(\frac{L}{a}\right). \quad (4.13)$$

Since both the entropy and the energy diverge logarithmically with system size we obtain a free energy of the form

$$F_{\text{vortex}} = \left(\frac{n\hbar^2\pi}{m} - 2k_B T\right) \ln\left(\frac{L}{a}\right). \quad (4.14)$$

The free energy thus diverges logarithmically either to positive or to negative infinity in the thermodynamic limit, and we identify a critical temperature $T_c = \frac{n\hbar^2\pi}{m k_B 2}$. This has the consequence that isolated vortices are very unlikely for $T < T_c$, and become highly probable for $T > T_c$. This simple argument for the two-dimensional classical XY model motivates the existence of a temperature above which vortices proliferate freely but below which they are bound. This phase transition is called the Berezinskii-Kosterlitz-Thouless transition and is a topological phase transition as the order-parameter does not spontaneously break a symmetry and acquire a non-zero value but instead it develops topological defects above a critical temperature.

4.1.3 Renormalisation-group theory

Renormalisation-group (RG) theory consists of integrating over the short wavelength fluctuations of a field in its Hamiltonian, incorporating the effect of the short wavelength fluctuations in the parameters of the Hamiltonian. By performing such integration iteratively, a procedure called coarse-graining, the parameters in the Hamiltonian describing the field change iteratively as larger and larger length-scales are considered, this causes the parameters in the Hamiltonian to 'flow' as a function of the length-scale under consideration. In this way the renormalisation-group allows one to transform statistical mechanics problems into problems concerning differential equations, whose solutions give a flow describing the large scale properties of a system.

For example given an arbitrary Hamiltonian describing a field $m(\boldsymbol{r})$

$$H(m(\boldsymbol{r})) = \int d\boldsymbol{r}^d h(m(\boldsymbol{r})), \tag{4.15}$$

where the functional h is the Hamiltonian density of the field. Consider the field in the frequency basis

$$m(\boldsymbol{r}) = \int_0^\Lambda \frac{d\boldsymbol{k}^d}{(2\pi)^d} e^{-i\boldsymbol{k}\cdot\boldsymbol{r}} m(\boldsymbol{k}), \tag{4.16}$$

where Λ is a physically motivated large momentum cutoff, such as inverse lattice spacing or healing length. Denoting the Hamiltonian density in frequency space by $\tilde{h}$ we get

$$H(m(\boldsymbol{k})) = \int d\boldsymbol{k}^d \tilde{h}(m(\boldsymbol{k})). \tag{4.17}$$

One then considers the field's short wavelength and long wavelength fluctuations, by separating it into

$$m(\boldsymbol{r}) = m_>(\boldsymbol{r}) + m_<(\boldsymbol{r}), \tag{4.18}$$

which we call the two terms the 'fast modes' and 'slow modes' respectively. Where in frequency space

$$m(\boldsymbol{k}) = \begin{cases} m_>(\boldsymbol{k}) & \text{if } \Lambda > |\boldsymbol{k}| > \Lambda/b \\ m_<(\boldsymbol{k}) & \text{if } \Lambda/b > |\boldsymbol{k}| > 0 \end{cases}. \tag{4.19}$$

One then performs the integral over the fast modes to get

$$\tilde{h}_<(m_<(\boldsymbol{k})) = \int_{\Lambda>|\boldsymbol{k}|>\Lambda/b} d\boldsymbol{k}^d \tilde{h}(m_<(\boldsymbol{k}), m_>(\boldsymbol{k})), \tag{4.20}$$

which leaves a consistent coarse-grained Hamiltonian density for a coarse-grained field. For the new Hamiltonian to describe the same energy scales as the old the momentum has to be rescaled as $\boldsymbol{k'} = s\boldsymbol{k}$ after coarse-graining. One must then introduce the renormalised field as $m'(\boldsymbol{k'}) = m_<(\boldsymbol{k'})/z$, where z is chosen to keep a coupling constant in h invariant under the RG transformation. The trick is then to make the coupling constants before and after the RG transformation the same by comparing $\tilde{h}(m'(\boldsymbol{k'})) \approx \tilde{h}(m(\boldsymbol{k}))$. By making this identification for infinitesimal coarse-graining steps and the resulting rescalings give a set of coupled differential equations for the coupling constants under coarse-graining.

Simple example RG calculation

For concreteness, consider the Hamiltonian density in a Gaussian theory where

$$H = \int d\boldsymbol{r}^d h(m(\boldsymbol{r})) = \int d\boldsymbol{r}^d J_1(\nabla m(\boldsymbol{r}))^2 - J_2 m(\boldsymbol{r})^2. \tag{4.21}$$

In momentum space this becomes

$$H = \int_{\Lambda>|\boldsymbol{k}|>0} \frac{d\boldsymbol{k}^d}{(2\pi)^d} (J_1 k^2 - J_2)|m(k)|^2. \tag{4.22}$$

Since the different k modes are decoupled the range of integration can be split into two parts (as in Eq. 4.19)

$$\begin{aligned} H &= \int_{\Lambda/b>|\boldsymbol{k}|>0} \tfrac{d\boldsymbol{k}^d}{(2\pi)^d} h_<(m(\boldsymbol{k})) = \int_{\Lambda>|\boldsymbol{k}|>0} \tfrac{d\boldsymbol{k}^d}{(2\pi)^d} \tilde{h}(m_<(\boldsymbol{k}), m_>(\boldsymbol{k})) \\ &= \int_{\Lambda/b>|\boldsymbol{k}|>0} \tfrac{d\boldsymbol{k}^d}{(2\pi)^d} (J_1 k^2 - J_2)|m_<(\boldsymbol{k})|^2 + \int_{\Lambda>|\boldsymbol{k}|>\Lambda/b} \tfrac{d\boldsymbol{k}^d}{(2\pi)^d} (J_1 k^2 - J_2)|m_>(\boldsymbol{k})|^2 \\ &= \int_{\Lambda/b>|\boldsymbol{k}|>0} \tfrac{d\boldsymbol{k}^d}{(2\pi)^d} (J_1 k^2 - J_2)|m_<(\boldsymbol{k})|^2 + C. \end{aligned} \tag{4.23}$$

C is a constant energy offset which does not affect the physics so we drop it. After the aforementioned rescaling of momentum and the field this gives

$$H = \int_{\Lambda>|\boldsymbol{k}'|>0} \frac{d\boldsymbol{k}'^d}{(2\pi)^d} b^{-d} z^2 (b^{-2} J_1 \boldsymbol{k}'^2 - J_2) |m'(\boldsymbol{k}')|^2. \tag{4.24}$$

Comparing Eq. 4.24 with the expression before the coarse-graining in Eq. 4.22 we can see that the coarse-graining associated with RG has the effect of changing the couplings in the Hamiltonian to

$$\begin{aligned} J_1' &= b^{-d-2} z^2 J_1, \\ J_2' &= b^{-d} z^2 J_2. \end{aligned} \tag{4.25}$$

The neat thing is that since the form of the Hamiltonian before and after RG is the same (or in practice for less trivial Hamiltonians we aim to make them approximately the same to some order), the procedure can be applied iteratively. With the couplings iteratively 'flowing' as described by Eq. 4.25. To complete the procedure we choose $z = b^{1+d/2}$ to keep J_1 the same to keep the magnitude of fluctuations constant. This gives the flow $J_2' = b^2 J_2$. Finally it is customary to consider infinitesimal steps in b parametrised in terms of $b = e^l$, to allow considering a continuous flow, i.e., the infinitesimal step $b = e^{\delta l}$, which means that before the coarse-graining the length-scale is l and after the coarse-graining the lengthscale is $l + \delta l$. Considering the couplings to be functions of the lengthscale they correspond to, from Eq. 4.25 we have $J_2' = J_2(l + \delta l)$ and $J_2 = J_2(l)$ resulting in the differential

$$J_2(l + \delta l) = J_2(l) b^2 = J_2(l)(e^{\delta l})^2 = J_2(l) + 2\delta l J_2(l) + O(\delta l^2). \tag{4.26}$$

Dropping second order terms, and higher, we can rearrange this into the form of a derivative by taking the limit

$$\lim_{\delta l \to 0} \frac{J_2(l + \delta l) - J_2(l)}{\delta l} = \frac{dJ_2}{dl} = 2J_2(l). \tag{4.27}$$

This way differential equations are found from RG analysis. For more complicated Hamiltonians such as that of coupled bilayer system of two-dimensional Bose gases in Section 5.2.1, this procedure leads to a system of coupled differential equations. By numerically integrating such systems of RG flow equations we can find what the macroscopic properties of the system are for a given set of microscopic conditions, this allows one to theoretically map out a phase diagram for a Hamiltonian as parameters are varied.

4.2 Numerical Methods

To investigate the properties of many-body systems at thermal equilibrium we utilise Monte Carlo techniques - specifically the Metropolis-Hastings algorithm. This numerical technique for statistical physics is used to simulate the coupled bilayer system in Sec. 6 and also the presence of disorder in a two-dimensional system in Sec. 8. These techniques allow us to obtain an ensemble of microstates which are consistent with finite temperature fluctuations of a field given its Hamiltonian. The methodology underpinning Monte Carlo sampling is outlined below.

4.2.1 Monte Carlo and the Metropolis algorithm

Consider a discrete configuration space where each member of the space C_i is a different configuration of the system

$$\{C\} = C_1, C_2, ..., C_{\mathcal{N}}. \tag{4.28}$$

Where $\mathcal{N}$ might be very large or even infinite for continuous systems. The expectation value of a quantity for a system whose possible microstates are the elements of this configuration space can be found as

$$\langle A \rangle = \frac{\sum_{i=1}^{\mathcal{N}} A(C_i)W(C_i)}{\sum_{i=1}^{\mathcal{N}} W(C_i)}. \tag{4.29}$$

Where $W(C_i)$ is the statistical weighting of the configuration, thus dividing by the summed weighting normalises it. If $\mathcal{N}$ is finite it would be possible to evaluate this sum explicitly and obtain an exact answer. However, considering even a calculation for the simple case of a 10 by 10 lattice with classical spins up or down reveal that summing over all the configurations is very time-consuming. To avoid performing the sum explicitly we use a technique based on random sampling of configurations, such methods are called Monte Carlo methods. The Monte Carlo algorithm is based on sampling a representative set of configurations based on known rules for their probability. W can thus be rewritten as a normalised probability distribution $P(C_i)$

$$\langle A \rangle = \sum_{i=1}^{\mathcal{N}} A(C_i) P(C_i). \tag{4.30}$$

One then needs to generate a sequence of configurations which results in the desired probability distribution. One solution is to start with an arbitrary allowed configuration and then update the configuration according to a stochastic process following rules so that the ensemble of configurations are distributed according to P. As the probability of going from one element in the sequence to the next is independent of the earlier configurations this sequence of configurations will be a Markov chain

$$\{C\} = C_{i_1}, C_{i_2}, ... \tag{4.31}$$

where the index i determines the specific sequence of configurations. An algorithm is needed for assigning the probability of going from any arbitrary configuration C_i to another C_j, $P(C_i \to C_j)$ such that their distribution is given by $P(C)$. Denoting the order in which the updates occur by a time we obtain that the time evolution of the probability of the system being in configuration C_i is given by

$$\frac{\partial P(C_i, t)}{\partial t} = \sum_{i \neq j} P(C_j, t) P(C_j \to C_i) - P(C_i, t) P(C_i \to C_j). \tag{4.32}$$

This can be understood heuristically as the first term representing an increase in C_i as another state is changed into C_i and the second term representing the probability of a state going from C_i to C_j. It may be useful to think of this as the number of times C_i appears in the sequence, which would be given by $N(C_i)$ and remember this is related to the probability by a constant $P(C_i) = N(C_i)/N_{tot}$, where N_{tot} are the number of terms in the sequence. However, as the probability distribution should remain constant with respect to time the RHS of Eq. (4.32) must equal zero. One solution that satisfies this and leaves the probability distribution constant in time is the following 'detailed balance equation'

$$\frac{P(C_j \to C_i)}{P(C_i \to C_j)} = \frac{P(C_i)}{P(C_j)}. \tag{4.33}$$

The detailed balance equation connects the Markov chain probabilities to the probability distribution the configurations should converge to. It is therefore the key equation to take into account when designing an update scheme for a system with a known probability distribution. The detailed balance equation does not give a unique $P(C_i \to C_j)$ and there are many different algorithms for determining $P(C_i \to C_j)$. Generating the Markov chain in this way means that the effect of the highest probability configurations are investigated earliest, thus the result will converge over time as opposed to generating all the configurations deterministically.

In the numerical simulations in this work we use the Metropolis-Hastings algorithm [45, 46] to generate the sequence of configurations that satisfy the balance equation for a thermodynamic system. For a classical system in thermodynamic equilibrium the relative probability of different configurations will be given by the Boltzmann distribution, thus

$$P(C_i) = \frac{1}{Z} e^{-\frac{E(C_i)}{k_B T}}. \tag{4.34}$$

with Z denoting the partition function. From Eq. (4.34) and Eq. (4.35) the update scheme must then satisfy

$$\frac{P(C_j \to C_i)}{P(C_i \to C_j)} = e^{-\frac{E(C_i)-E(C_j)}{k_B T}}. \tag{4.35}$$

The Metropolis algorithm splits $P(C_i \to C_j)$ into the probability of selecting the update multiplied by the probability of accepting the update

$$P(C_j \to C_i) = P^{select}(C_j \to C_i) P^{accept}(C_j \to C_i). \tag{4.36}$$

The selection of the configuration to change is random, thus $P^{select}(C_j \to C_i)$ cancels out from the top and bottom of the balance equation and the only remaining choice is the probability of accepting a configuration change. The detailed balance equation thus reduces to

$$\frac{P^{accept}(C_j \to C_i)}{P^{accept}(C_i \to C_j)} = e^{-\frac{E(C_i)-E(C_j)}{k_B T}} \equiv R. \tag{4.37}$$

The acceptance probabilities in the Metropolis algorithm are then chosen as

$$P(C_j \to C_i) = \begin{cases} R, & \text{if } R < 1 \\ 1, & \text{if } R \geq 1 \end{cases} \tag{4.38}$$

$$P(C_i \to C_j) = \begin{cases} 1, & \text{if } R \leq 1 \\ 1/R, & \text{if } R > 1. \end{cases} \tag{4.39}$$

By inspection this satisfies Eq. (4.37) and combined with randomly selecting the proposed configuration to update to means the Metropolis algorithm satisfies the detailed balance equation. This algorithm can thus be used to investigate ensemble properties of thermodynamic systems. It is used to investigate the equilibrium phase-diagram of tunnel-coupled bilayers in Ch. 6 and the effect of disorder on two-dimensional Bose gases in Ch. 8. For these cases the Hamiltonians used and details of the implementation can be found in the respective chapters.

5
Density Noise Readout

The work in this chapter was featured in the published work [47].

For bilayer systems with tunnel-coupling between the layers the Hamiltonian can naturally be expressed in terms of relative and common excitations in the two layers, these are expected to behave qualitatively differently [48]. As such to study bilayer systems with coupling, as is done in Ch. 6 we need a way to probe both the relative and common degrees of freedom. For independent condensates the images of matter-wave interference fringes taken from the side after TOF gives information about relative phase fluctuations. The matter-wave interference fringes can be used to infer the statistics of the two layers on the assumption that they are statistically independent. However, if there is quantum mechanical tunnelling between the two layers they are no longer independent. Because of this, for tunnel-coupled bilayers, the relative phase information does not capture the statistics of the fluctuations within each layer but just their relative fluctuations. This is what motivated studying density noise after a short TOF expansion to possibly get some information about the common mode fluctuations. While the density noise patterns arising from self-interference within a single Bose gas have been studied before [49–53]; my novel contribution is extending the theoretical description to bilayer systems to establish

a way to analyse the resulting spatial features of the density noise patterns from bilayers to probe the phase coherence of the common phase.

One obstacle hampering previous experimental studies of density noise patterns from 2D Bose gases were issues focusing the imaging system on the density noise pattern [54]. If the density noise patterns are not in focus their features will not appear correct leading to features in the patterns not arising from the in-situ properties of the cloud. A solution to this problem was found by Shinichi Sunami, using a thin horizontal repumper slice to image only the part of the cloud within the focal depth of the imaging system. Focusing the system by looking at the smallest spatial features of the density noise pattern in the repumped slice as its distance from the objective lens is adjusted, i.e., moving the sheet of light to pick out different slices within the cloud of atoms; further details are given in the supplementary material of [47]. This chapter first outlines the motivation behind studying density noise, then the data from the experimental investigation is analysed using different analysis techniques to verify that the new common mode readout technique gives results consistent with our other ways of establishing spatial coherence of the phases of 2D Bose gases. This provides confidence in the density noise analysis as a technique for common-mode readout before applying it to the coupled bilayer system in Ch. 6.

5.1 Motivation

In our experiment, matter-wave interference fringes are formed when two clouds of atoms are imaged from the side after a $\sim$17 ms TOF expansion. Such patterns are analogous to the straight line fringe patterns seen in the far field of the double slit experiment. These fringes arise from interference between two spatially separated degenerate quantum gases independently of whether, or not, there is a fixed relative phase between the two interfering condensates [44].

However, even within a single two-dimensional condensate the different regions will interfere with one another after TOF, and this self-interference gives rise to less clearly structured patterns called density noise. These patterns arise from the initial in-situ phase fluctuations even if the in-situ density is uniform as seen in

Fig. 5.2. The density noise patterns therefore encode information about the in-situ phase fluctuations in the condensate. The density-noise patterns are analogous to near-field diffraction in light. This comes from the evolution of the bosonic field after free propagation for some duration of TOF and the evolution of a light field after propagating some distance along an optical axis being mathematically equivalent [55], the implications of this are expanded upon in Sec. 5.3.

A complementary viewpoint to interference, to interpret the density patterns observed after a short duration of free expansion, can be found from the connection between phase gradients and the superfluid velocity in a BEC. In a superfluid the velocity field is related to the gradient of the complex phase of the macroscopic wavefunction by

$$\boldsymbol{v}_s = \frac{\hbar}{m}\nabla\theta(\boldsymbol{r}). \tag{5.1}$$

Since density fluctuations are suppressed in the low-temperature limit, as described in Section 4 and seen in Fig. 5.2b, assuming a uniform in-situ density is a reasonable initial condition so if the density increases in one region after a short TOF this indicates that the velocity field in-situ nearby had a net flux towards that region of increased density after TOF. By this argument the density pattern contains information about the phase-field. This intuition is the basis for a successful method of phase reconstruction from density noise in 1D Bose gases in Ref. [56]; work which appeared after the work this chapter is based on was published [47]. Furthermore, based on discussions with the first author of Ref. [56], reconstruction of the initial phase field turns out to be easier in 1D as the velocity field there is effectively a scalar, whereas in 2D it is a vector field.

Using this intuition we can reason that if the phase-field and its gradients are random and uncorrelated the velocity field will also be disordered and we therefore expect the density field after TOF to lack significant spatial structure, as the velocity field will average out within a shorter distance. However, if there are slower phase gradients, corresponding to a more spatially ordered phase, then after a short TOF the atom cloud will have a distinct spatial structure, as shown in Fig. 5.2b.

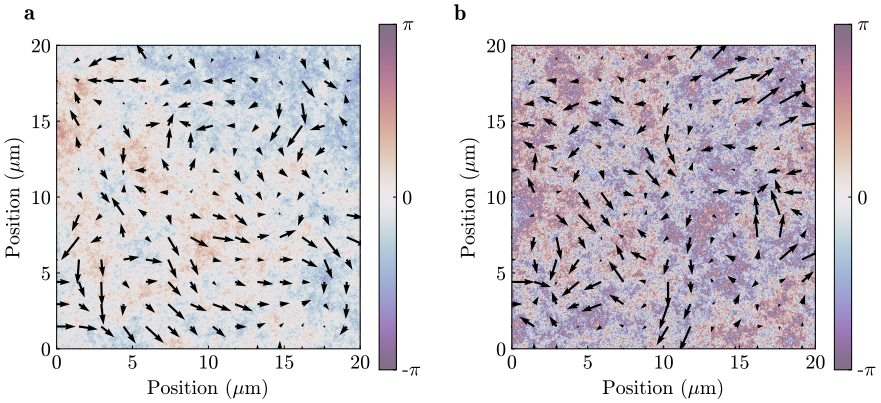


Figure 5.1: Illustration of relation between density noise and phase gradients. This toy example shows phase fields and velocity fields (black arrows) for (**a**) 2D Bose gases with relatively ordered (low-temperature) phase profiles, and (**b**) for a relatively disordered (high-temperature) phase profile. The phase profiles feature the phononic phase fluctuations expected in thermal equilibrium and are generated using an Ornstein-Uhlenbeck process as described in En Chang's DPhil thesis [48]. The velocity fields are calculated using Eq. 5.1. Observe that if the spatial structure of the phase field is smaller, as in panel **b** compared to panel **a**, the spatial coherence of the velocity field is also reduced, this in turn reduces the spatial structure of the density noise patterns arising after short TOF expansion.

Furthermore, as derived in Section 5.2.1 of this chapter, in the parameter regime studied in this thesis the density noise arising from bilayer systems is primarily sensitive to symmetric excitations in both layers. The density noise patterns provide valuable information about the phase coherence of the symmetric mode of the system- complementary to the information captured by the interference fringes which primarily reveal information about the relative excitations.

In the following section we apply the density noise technique to our experiment, and benchmark it against interference measurements for independent bilayers, and single layers.

5.2 Experimental Readout from Density Noise

For low-dimensional quantum gases consisting of two constituent systems, the correlation properties of the relative and common phase modes are crucial observables characterising the difference and sum of two fluctuating fields. While relative modes can be probed by matter-wave interferometry [6, 57], there had

previously not been a direct method for measuring the coherence of common modes. To understand novel phases of matter predicted in coherently coupled pairs of low-dimensional systems, described in Ch. 6, such as antisymmetric superfluid order in strongly coupled 2D systems [58, 59], it is crucial to extend measurement capabilities to common-mode correlations.

In this chapter we report the measurement of the noise correlations of expanded single and decoupled bilayer 2D Bose gases. This is done using novel theoretical work for density noise readout from bilayers which provides information about common-mode phase fluctuations. Using analytical models we determine the superfluid exponent η for a wide range of the phase-space densities across the BKT transition. The results are consistent for single and decoupled bilayer systems, as expected in the absence of interlayer coupling. We benchmark these results with those determined from measurement of the relative phase of our bilayer system using local matter-wave interferometry [6].

We prepare 2D degenerate Bose gases of ^{87}Rb atoms in a cylindrically-symmetric trap with strong confinement along the z direction. In this work, we create single-well or double-well vertical confinement using either a single-RF or multiple-RF dressing technique as described in Ch. 2. In both cases, near the minimum of each well the vertical oscillation frequencies of atoms are around $\omega_z/2\pi = 1.2\,\mathrm{kHz}$ giving a dimensionless 2D interaction strength $\tilde{g} = \sqrt{8\pi}a_s/\ell_0 = 0.08$, where a_s is the 3D scattering length, $\ell_0 = \sqrt{\hbar/(m\omega_z)}$ is the harmonic oscillator length along z for an atom of mass m and $\hbar$ is the reduced Planck constant. We impose additional optical trapping in the horizontal plane using a ring-shaped strong off-resonant laser beam at 532 nm to realise near-homogeneous 2D systems [47]. This blue detuned beam is shaped using a digital micromirror device (DMD). We load atoms into the trap at a temperature $T = 50\,\mathrm{nK}$, set by forced evaporation. For double-well potentials we equalise the population N in each layer by maximising the matter-wave interference contrast [6, 60]. For the bilayers realised in this chapter the large inter-well separation of $7\,\mu\mathrm{m}$ gives a decoupled bilayer system. We vary N to cover a broad range of the 2D phase-space density (PSD) $\mathcal{D} = nh^2/(2\pi m k_B T)$ which is the

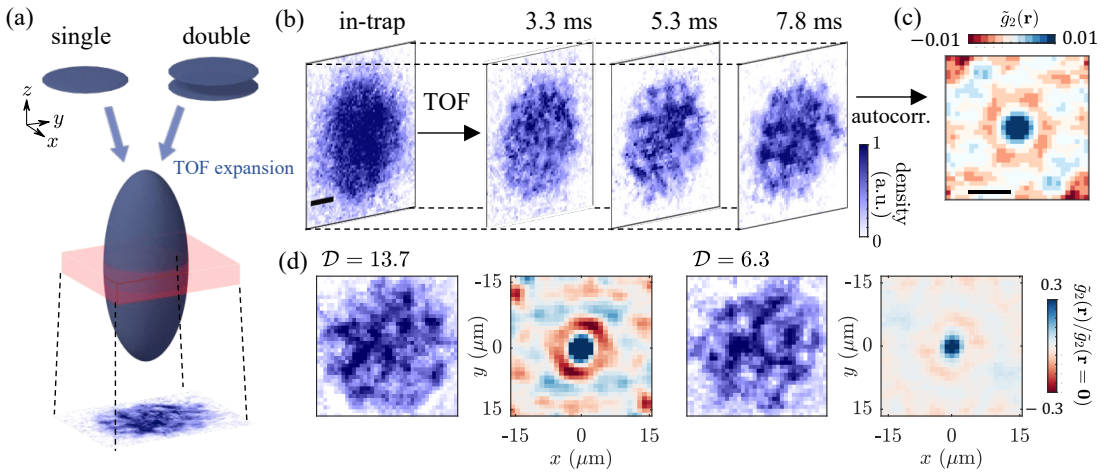


Figure 5.2: Noise interferometry of 2D Bose gases. (a) Sketch of the density noise detection scheme. We trap single- or double-layer ultracold 2D Bose gases with tight vertical confinement, and release them for a time-of-flight (TOF) expansion of duration t. The tight vertical confinement results in a fast vertical expansion of the cloud without significant expansion in the radial direction. We record a slice of the density distribution using absorption imaging with a selective optical repumping technique (red transparent sheet), this is necessary since the depth of field of the high-resolution imaging apparatus is smaller than the vertical extent of the expanded cloud. (b) Single-shot images of the density distribution of trapped single-layer clouds with no expansion (in-situ) and at $t = 3.3$, 5.3 and 7.8 ms. (c) The noise correlation function $\tilde{g}_2(\boldsymbol{r})$, obtained by calculating the density-density correlations and averaging over experimental repeats; see text. A characteristic ring structure emerges at distance $|\boldsymbol{r}| \sim 7$ µm due to density modulations that are present in the expanded cloud at $t = 7.8$ ms. The black bars in panels (b) and (c) denote 10 µm. (d) Typical single-shot density distribution and $\tilde{g}_2(\boldsymbol{r})$ shown after $t = 5.3$ ms for decoupled bilayer systems with phase-space densities of $\mathcal{D} = 13.7$ and 6.3.

dimensionless thermodynamic quantity relevant to the emergent properties of 2D Bose gases. We study phase-space densities between 5 and 24. For all parameters studied in this chapter, the quasi-2D conditions $\hbar\omega_z > k_B T$ and $\hbar\omega_z > \mu$ are satisfied, where μ is the chemical potential [47].

The detection scheme is illustrated in Fig. 5.2a. The trap is abruptly turned off to release the 2D gas for a time-of-flight (TOF) expansion of duration t between 3.3 and 7.8 ms [6], starting with either one or two clouds. Once released, the clouds expand ballistically along the z direction with negligible expansion in the radial direction. We image a slice of the expanded clouds with thickness $L_z = 10$ µm along the z direction which is much smaller than the extent of the expanded cloud in this direction, as illustrated in Fig. 5.2a. This ensures that the imaged sample is thin

compared to the depth of field of the high-resolution imaging system [47]; further, we carefully focus the imaging system using the density-noise patterns as described in [47]. This minimises the systematic effect of imperfect imaging on the density pattern measurements [52, 61]. Examples of the density distribution after several values of the TOF duration t, including the in-situ density distribution at $t = 0$, are shown in Fig. 5.2b. The system is deep in the superfluid regime with peak PSD of $\mathcal{D} = 24$ [6, 47]. Compared to the in-situ density distribution, the expanded cloud shows the formation of density modulations with a length scale growing with t, because for self-interference of the cloud the interference occurs at distances that depend on t [50, 52, 53]. As a result, initial phase fluctuations transform into the density modulations we analyse. We autocorrelate the normalised density distribution in each cloud and then average the density-density correlations over at least 20 repetitions. Thus, we obtain the density noise correlation function [47, 53]

$$g_2(\boldsymbol{r}, t) = \frac{\langle \Psi^\dagger(\boldsymbol{r}, t)\Psi^\dagger(\boldsymbol{0}, t)\Psi(\boldsymbol{r}, t)\Psi(\boldsymbol{0}, t)\rangle}{n(\boldsymbol{r}, t)n(\boldsymbol{0}, t)}. \tag{5.2}$$

5.2.1 Noise correlations of expanded bilayer 2D Bose gases

To read out information regarding the in-situ properties of the clouds from the density-noise we need to relate the form of the density-noise correlation functions of the fields after a TOF with duration t (shown in Eq. 5.2 and experimentally in Fig. 5.2c and d) to properties of the fields in-situ. To establish the relation between the in-situ correlations and the density noise correlations for bilayer systems we need a theoretical description capturing the interference between the clouds and self-interference effects. The derivation in this chapter shares similarities with the derivation for the single-layer Bose gases in Refs. [53, 54], with the complete details of the derivation included in Appendix A. We consider a bilayer system with two layers $i = 1, 2$ initially separated by $2d$, in the z direction where $2d = 7\,\mu\text{m}$ for the experiments reported in this chapter. We express the two layers using bosonic field operators $\Psi_i(\boldsymbol{r})$, $i = 1, 2$. We take the initial 3D wavefunction of

the bilayer system to be of the form

$$\hat{\mathbf{\Psi}}_0(\boldsymbol{r}_{2D}, z; t) = [\hat{\mathbf{\Psi}}_1(\boldsymbol{r})\delta(d-z) + \hat{\mathbf{\Psi}}_2(\boldsymbol{r})\delta(d+z)]/\sqrt{2}, \tag{5.3}$$

and analyse its expansion dynamics. Free expansion of the bosonic field operator is given by

$$\hat{\mathbf{\Psi}}(\boldsymbol{r}, t) = \int d^3\boldsymbol{r}' G_3(\boldsymbol{r}-\boldsymbol{r}', t)\hat{\mathbf{\Psi}}(\boldsymbol{r}', 0), \tag{5.4}$$

where the 3D Green's function is

$$G_3(\boldsymbol{r}-\boldsymbol{r}', t) = G_1(x-x', t)G_1(y-y', t)G_1(z-z', t), \tag{5.5}$$

and

$$G_1(r, t) = \sqrt{\frac{m}{2\pi i\hbar t}} e^{\frac{im}{2\hbar t}r^2}. \tag{5.6}$$

Combining the prefactors into $A = \frac{m}{2\pi\hbar t}$, the density distribution after the TOF expansion is

$$\hat{n}(\boldsymbol{r}, t) = A^3 \int d^3\boldsymbol{v} \int d^3\boldsymbol{w}\; e^{\frac{-im}{2\hbar t}(\boldsymbol{r}-\boldsymbol{v})^2} \hat{\mathbf{\Psi}}^\dagger(\boldsymbol{v}, 0) e^{\frac{im}{2\hbar t}(\boldsymbol{r}-\boldsymbol{w})^2} \hat{\mathbf{\Psi}}(\boldsymbol{w}, 0). \tag{5.7}$$

Following the procedure in Ref. [53], denoting the spatial coordinates in the xy-plane by the subscript $\parallel$ and coordinates perpendicular to it (i.e. in the z direction) by the subscript $\perp$, the density-density correlation function is

$$\begin{aligned} g_2^{\mathrm{3D}}(\boldsymbol{r}_1, \boldsymbol{r}_2, t) =& \frac{A^4}{4n_0^2} \int d^2\boldsymbol{r} \int d^2\boldsymbol{r}' \int ds_\perp \int dS_\perp \int du_\perp \int dU_\perp \\ & \times e^{\frac{-im}{4\hbar t}\left[\boldsymbol{r}^2 - \boldsymbol{r}'^2 - 2\boldsymbol{r}_{\parallel 12}\cdot(\boldsymbol{r}-\boldsymbol{r}')\right]} \times e^{\frac{-im}{\hbar t}\left[(S_\perp - \frac{r_{\perp 12}}{2})s_\perp + (U_\perp + \frac{r_{\perp 12}}{2})u_\perp - R_{\perp 12}(s_\perp + u_\perp)\right]} \\ & \times \left\langle \hat{\mathbf{\Psi}}_0^\dagger(\frac{\boldsymbol{r}}{2}, S_\perp + \frac{s_\perp}{2}) \hat{\mathbf{\Psi}}_0^\dagger(-\frac{\boldsymbol{r}}{2}, U_\perp + \frac{u_\perp}{2}) \hat{\mathbf{\Psi}}_0(\frac{\boldsymbol{r}'}{2}, S_\perp - \frac{s_\perp}{2}) \hat{\mathbf{\Psi}}_0(-\frac{\boldsymbol{r}'}{2}, U_\perp - \frac{u_\perp}{2}) \right\rangle, \end{aligned} \tag{5.8}$$

where we use centre-of-mass coordinates, $\boldsymbol{r}_{12} = \boldsymbol{r}_1 - \boldsymbol{r}_2$ and $\boldsymbol{R}_{12} = (\boldsymbol{r}_1 + \boldsymbol{r}_2)/2$. The superscript 3D in Eq. 5.8 is used to distinguish this quantity from the g_2 extracted experimentally and to maintain consistent notation with the single layer case [53], which are functions of 2D spatial coordinates. With integration along the z direction over a sufficient integration width, equivalent to the imaging procedure in the

experiment reported in the main text (see Ref. [47] supplementary material section B.4 for how integration-width affects g_2), we obtain in terms of 2D coordinates,

$$g_2(\boldsymbol{r}_{1,2D},\boldsymbol{r}_{2,2D}) = \int dr_{1z}\int dr_{2z} g_2^{3D}(\boldsymbol{r}_{1,3D},\boldsymbol{r}_{2,3D}), \tag{5.9}$$

where the integration over r_{1z}, r_{2z} (or $R_{\perp 12}$ and $r_{\perp 12}$), gives delta functions for $u_\perp$ and $s_\perp$. The delta functions result in $s_\perp = -u_\perp$ and $s_\perp = u_\perp = 0$ and thus modify the prefactor, such that

$$g_2(\boldsymbol{r}_{1,2D},\boldsymbol{r}_{2,2D}) = \frac{A^2}{4n_0^2}\int d^2\boldsymbol{r}\int d^2\boldsymbol{r}'\int dS_\perp\int dU_\perp e^{\frac{-im}{4\hbar t}\left[\boldsymbol{r}^2-\boldsymbol{r}'^2-2\boldsymbol{r}_{\parallel 12}\cdot(\boldsymbol{r}-\boldsymbol{r}')\right]} \times\left\langle\hat{\boldsymbol{\Psi}}_0^\dagger(\frac{\boldsymbol{r}}{2},S_\perp)\hat{\boldsymbol{\Psi}}_0^\dagger(-\frac{\boldsymbol{r}}{2},U_\perp)\hat{\boldsymbol{\Psi}}_0(\frac{\boldsymbol{r}'}{2},S_\perp)\hat{\boldsymbol{\Psi}}_0(-\frac{\boldsymbol{r}'}{2},U_\perp)\right\rangle. \tag{5.10}$$

We now reintroduce the original z spatial variables, $S_\perp = (z_1+z_2)/2$, $s_\perp = z_1 - z_2$ and $U_\perp = (z_3+z_4)/2$, $u_\perp = z_3 - z_4$. With the delta functions for $s_\perp$ and $u_\perp$ described above we have $S_\perp = z_1$, $U_\perp = z_3$, so that

$$g_2(\boldsymbol{r}_{1,2D},\boldsymbol{r}_{2,2D}) = \frac{A^2}{4n_0^2}\int d^2\boldsymbol{r}\int d^2\boldsymbol{r}'\int dz_1\int dz_3 e^{\frac{-im}{4\hbar t}\left[\boldsymbol{r}^2-\boldsymbol{r}'^2-2\boldsymbol{r}_{\parallel 12}\cdot(\boldsymbol{r}-\boldsymbol{r}')\right]} \times\left\langle\hat{\boldsymbol{\Psi}}_0^\dagger(\frac{\boldsymbol{r}}{2},z_1)\hat{\boldsymbol{\Psi}}_0^\dagger(-\frac{\boldsymbol{r}}{2},z_3)\hat{\boldsymbol{\Psi}}_0(\frac{\boldsymbol{r}'}{2},z_1)\hat{\boldsymbol{\Psi}}_0(-\frac{\boldsymbol{r}'}{2},z_3)\right\rangle. \tag{5.11}$$

To simplify notation we introduce

$$\rho_{ijkl}(\boldsymbol{r},\boldsymbol{r}') = \left\langle\hat{\boldsymbol{\Psi}}_i^\dagger(\frac{\boldsymbol{r}}{2})\hat{\boldsymbol{\Psi}}_j^\dagger(-\frac{\boldsymbol{r}}{2})\hat{\boldsymbol{\Psi}}_k(\frac{\boldsymbol{r}'}{2})\hat{\boldsymbol{\Psi}}_l(-\frac{\boldsymbol{r}'}{2})\right\rangle. \tag{5.12}$$

Substituting Eq. 5.3 into Eq. 5.11 and evaluating the z_1 and z_2 integrals,

$$g_2(\boldsymbol{r}_{1,2D},\boldsymbol{r}_{2,2D}) = \frac{A^2}{4n_0^2}\int d^2\boldsymbol{r}\int d^2\boldsymbol{r}' e^{\frac{-im}{4\hbar t}\left[\boldsymbol{r}^2-\boldsymbol{r}'^2-2\boldsymbol{r}_{\parallel 12}\cdot(\boldsymbol{r}-\boldsymbol{r}')\right]} \times\frac{1}{4}\Big[\rho_{1111}(\boldsymbol{r},\boldsymbol{r}')+\rho_{2121}(\boldsymbol{r},\boldsymbol{r}')+\rho_{1212}(\boldsymbol{r},\boldsymbol{r}')+\rho_{2222}(\boldsymbol{r},\boldsymbol{r}')\Big]. \tag{5.13}$$

Using the density-phase representation of the bosonic field in the trap, $\Psi(\boldsymbol{r}) \simeq \sqrt{n}\exp(i\phi(\boldsymbol{r}))$, applicable for our case of quasicondensates [62], Eq. 5.12 can be represented by the phase fluctuation as $\rho_{ijkl}(\boldsymbol{r},\boldsymbol{r}') \sim n_0^2\left\langle e^{i[\theta_i(\boldsymbol{r}/2)+\theta_j(-\boldsymbol{r}/2)-\theta_k(\boldsymbol{r}'/2)-\theta_l(-\boldsymbol{r}'/2)]}\right\rangle$ where $\theta(\boldsymbol{r}) = (\phi_1(\boldsymbol{r})-\phi_2(\boldsymbol{r}))/2$, $\varphi(\boldsymbol{r}) = (\phi_1(\boldsymbol{r})+\phi_2(\boldsymbol{r}))/2$ are the antisymmetric

and symmetric phase modes. Writing the complex exponentials using cosines, the density-density correlation function of the expanded cloud is

$$g_2(\boldsymbol{r}_{1,2D},\boldsymbol{r}_{2,2D}) = \frac{A^2}{4n_0^2}\int d^2\boldsymbol{r}\int d^2\boldsymbol{r}' e^{\frac{-im}{4\hbar t}\left[\boldsymbol{r}^2-\boldsymbol{r}'^2-2\boldsymbol{r}_{\parallel 12}\cdot(\boldsymbol{r}-\boldsymbol{r}')\right]} \times \rho_\varphi(\boldsymbol{r},\boldsymbol{r}')\Big\langle \cos(\Delta\theta(\boldsymbol{r},\boldsymbol{r}'))\cos(\Delta\theta(-\boldsymbol{r},-\boldsymbol{r}'))\Big\rangle, \tag{5.14}$$

where $\rho_\varphi(\boldsymbol{r},\boldsymbol{r}') = n_0^2\left\langle e^{i[\varphi(\boldsymbol{r}/2)+\varphi(-\boldsymbol{r}/2)-\varphi(\boldsymbol{r}'/2)-\varphi(-\boldsymbol{r}'/2)]}\right\rangle$ expresses the common-mode phase correlation which is the dominant contribution to the measured density-noise correlation; the final term containing $\Delta\theta(\boldsymbol{r},\boldsymbol{r}') = \theta(\boldsymbol{r}/2)-\theta(\boldsymbol{r}'/2)$ encapsulates the effect of finite mixing of relative phase on g_2. Introducing the shorthand notation $\Delta\theta(\pm) = \Delta\theta(\pm\boldsymbol{r},\pm\boldsymbol{r}')$, this term can be expressed as exponentials

$$\Big\langle \cos(\Delta\theta(+))\cos(\Delta\theta(-))\Big\rangle = \frac{1}{4}\Big\langle e^{i[\Delta\theta(+)+\Delta\theta(-)]} + e^{i[\Delta\theta(+)-\Delta\theta(-)]} + e^{i[-\Delta\theta(+)+\Delta\theta(-)]} + e^{i[-\Delta\theta(+)-\Delta\theta(-)]}\Big\rangle, \tag{5.15}$$

assuming Gaussian phase fluctuations, as in the case for a single-layer, we get $\left\langle e^{i[\theta(r)+\theta(r')]}\right\rangle = e^{-\frac{1}{2}\left\langle[\theta(r)+\theta(r')]^2\right\rangle}$. Defining the relative-phase correlation function

$$\mathcal{F}_{\rm rel}(\boldsymbol{r}-\boldsymbol{r}') \equiv \left\langle e^{i[\theta(\boldsymbol{r})-\theta(\boldsymbol{r}')]}\right\rangle \simeq \langle\hat\Psi_1^\dagger(\boldsymbol{r},0)\hat\Psi_2(\boldsymbol{r},0)\hat\Psi_2^\dagger(\boldsymbol{0},0)\hat\Psi_1(\boldsymbol{0},0)\rangle/n_0^2 \tag{5.16}$$

and expanding the exponents for each term in Eq. 5.15,

$$\Big\langle \cos(\Delta\theta(+))\cos(\Delta\theta(-))\Big\rangle \approx \mathcal{F}_{\rm rel}([\boldsymbol{r}-\boldsymbol{r}']/2)^2, \tag{5.17}$$

to linear order in $\langle\Delta\theta(-)\Delta\theta(+)\rangle$. Thus the density correlation function is

$$g_2(\boldsymbol{r}_{1,2D},\boldsymbol{r}_{2,2D}) \approx \frac{A^2}{4n_0^2}\int d^2\boldsymbol{r}\int d^2\boldsymbol{r}' e^{\frac{-im}{4\hbar t}\left[\boldsymbol{r}^2-\boldsymbol{r}'^2-2\boldsymbol{r}_{\parallel 12}\cdot(\boldsymbol{r}-\boldsymbol{r}')\right]}\rho_\varphi(\boldsymbol{r},\boldsymbol{r}')\mathcal{F}_{\rm rel}([\boldsymbol{r}-\boldsymbol{r}']/2)^2. \tag{5.18}$$

Following the procedure for the case of a single layer [53] we perform a change of variables, $\boldsymbol{q} = (m/2\hbar t)(\boldsymbol{r}-\boldsymbol{r}')$, $\boldsymbol{R} = (\boldsymbol{r}+\boldsymbol{r}')/2$, effectively resulting in a Fourier transform. Rewriting the result using $\mathcal{F}_{\rm com}(\boldsymbol{r})$ and $\boldsymbol{q}_t$ defined as $\mathcal{F}_{\rm com}(\boldsymbol{r})^2 \simeq \langle\Psi_1^\dagger(\boldsymbol{r})\Psi_2^\dagger(\boldsymbol{r})\Psi_1(\boldsymbol{0})\Psi_2(\boldsymbol{0})\rangle/n^2$ and $\boldsymbol{q}_t = \hbar\boldsymbol{q}t/m$, where t is the TOF duration, gives

$$g_2(\boldsymbol{r},t) \approx \frac{1}{(2\pi)^2}\int d^2\boldsymbol{q}\int d^2\boldsymbol{R}\cos(\boldsymbol{q}\cdot\boldsymbol{r})\cos(\boldsymbol{q}\cdot\boldsymbol{R})\frac{\mathcal{F}_{\rm com}(\boldsymbol{q}_t)^2\mathcal{F}_{\rm com}(\boldsymbol{R})^2}{\mathcal{F}_{\rm com}(\boldsymbol{R}-\boldsymbol{q}_t)\mathcal{F}_{\rm com}(\boldsymbol{R}+\boldsymbol{q}_t)}\mathcal{F}_{\rm rel}(\boldsymbol{q}_t)^2. \tag{5.19}$$

One way to understand the behaviour of Eq. 5.19 is to look at the terms inside the integral and reason that we expect oscillating behaviour due to the trigonometric functions, however the oscillating behaviour is damped as the distance increases because of the decaying correlation functions. The degree of damping of the oscillatory behaviour in the density-noise autocorrelations after TOF is then related to the degree of coherence of the complex phases of the condensates in-situ. This heuristic view of Eq. 5.19 is broadly consistent with the velocity-field picture seen in Fig. 5.1 in that the degree of spatial correlations in the phase/velocity field will be reflected in the degree of the spatial correlations in the positions of the particles after TOF.

In Fig. 5.3, we compare Eq. 5.19 and Eq. 5.20, the density-noise correlation functions for the single-layer and bilayer systems. The difference between the two models becomes pronounced deep in the normal regime where the correlation length r_0 is much smaller than the system size used in the experiment, $\sim 30\,\mu\text{m}$. Physically, this is due to the fact that if the relative phase is correlated, the final term in Eq. 5.19 falls off slowly inside the integral, compared to the other terms inside the integral. Our theory collaborator Dr Vijay Singh performed numerical integration of Eq. 5.19 (Eq. 5.20) which we then interpolated between to perform the fitting of experimental data taken with single-layer (bilayer) systems [53].

5.2.2 Experimental results

With our experimental investigation we wish to benchmark the density-noise readout technique for bilayer systems. To do this we compare it to our standard method of interferometric readout from images of interference fringes taken from the side after longer TOF. We also investigate the density-noise readout technique for a single layer, both since this has not previously been implemented experimentally and since the derivation for density noise readout for bilayers in Sec. 5.2.1 builds on the single-layer readout derivation. Finally we study the readout from the density noise of a system of independent bilayers, where each layer is expected to show the same statistics in their common and relative modes; we probe this by density noise and

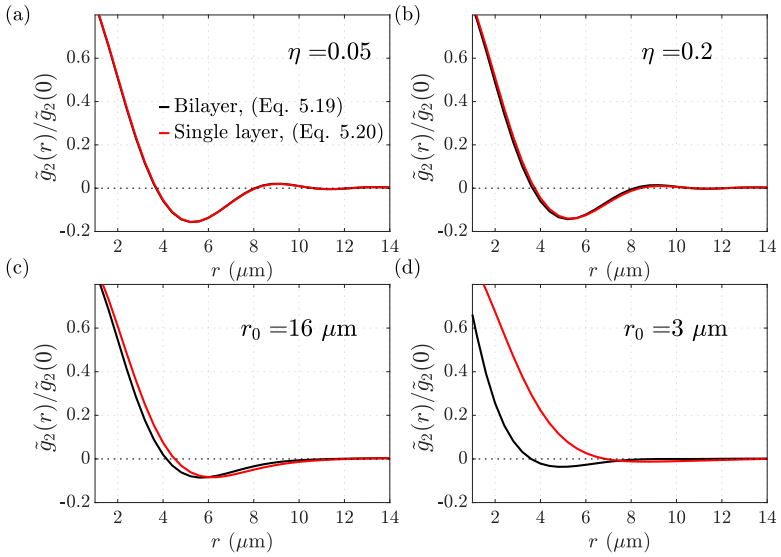


Figure 5.3: Effect of relative mode phase fluctuations on density noise. Theoretical model of bilayer density-noise correlation functions with (red) and without (black) considering the mixing of relative phase effect: (a,b) for the superfluid regime, and (c,d) normal regime. The theoretical curves are obtained by the numerical integration of Eq. 5.19 and Eq. 5.20 as in Ref. [53], where both the common-mode and the relative-mode correlation functions $\mathcal{F}_{\rm com}$ and $\mathcal{F}_{\rm rel}$ are taken to be the first-order correlation function of a single layer system, as applicable for a decoupled bilayer.

matter-wave fringe readout respectively. For a system of two independent bilayers the fluctuations in each layer should match the fluctuations in a single isolated layer, studied by analysing the density noise due to self-interference of a single layer.

In Fig. 5.2c, we show $\tilde{g}_2(\boldsymbol{r}) \equiv g_2(\boldsymbol{r}) - 1$ at $t = 7.8\,$ms, for a single layer, this features a characteristic minimum at distance $r \sim 7\,\mu$m as predicted from the theoretical model [53]. We repeat these measurements for a decoupled bilayer system. Examples of the single-shot density distribution and averaged noise correlation function $\tilde{g}_2(\boldsymbol{r}, t)$, taken with $t = 5.3\,$ms for the systems at $\mathcal{D} = 13.7$ and 6.3, are shown in Fig. 5.2d. The existence of the characteristic minimum of $\tilde{g}_2(\boldsymbol{r})$ at high $\mathcal{D}$ is a feature of the superfluid phase, the minimum and amplitude of oscillations in $\tilde{g}_2(\boldsymbol{r})$ are suppressed in the normal phase at lower $\mathcal{D}$ [53].

To infer the properties of the system we analyse how $g_2(\boldsymbol{r}, t)$ depends on the expansion time and the in-situ phase fluctuations. Analysis of free expansion of a single-layer 2D quasicondensate with phase fluctuations yields $g_2(\boldsymbol{r}, t)$ as a

function of expansion time t [47, 50, 53]

$$g_2(\boldsymbol{r},t) = \frac{1}{(2\pi)^2}\int d^2\boldsymbol{q}\int d^2\boldsymbol{R}\cos(\boldsymbol{q}\cdot\boldsymbol{r})\cos(\boldsymbol{q}\cdot\boldsymbol{R}) \times\frac{\mathcal{F}(\boldsymbol{q}_t)^2\mathcal{F}(\boldsymbol{R})^2}{\mathcal{F}(\boldsymbol{R}-\boldsymbol{q}_t)\mathcal{F}(\boldsymbol{R}+\boldsymbol{q}_t)}, \tag{5.20}$$

where $\boldsymbol{q}_t = \hbar\boldsymbol{q}t/m$ with $\boldsymbol{q}$ being the wave vector and the functions $\mathcal{F}$ are the first-order correlation functions i.e. $\mathcal{F}(\boldsymbol{r}) \sim g_1(\boldsymbol{r})$. This predicts distinctly different behaviour for $g_2(\boldsymbol{r},t)$ for the algebraic and exponential forms of $g_1(\boldsymbol{r})$, which we utilise to probe the BKT transition [47, 53].

In Fig. 5.4a, we show the measurements of $\tilde{g}_2(r,t)$ for a single-layer cloud deep in the superfluid regime, with $\mathcal{D} = 24$, for several expansion times t. We shift the locations of the trapped cloud with a magnetic bias field along z for each t, without changing any system parameters such as trap geometry, temperature and atom number, such that the expanded cloud is at the focus of the imaging apparatus after expansion time t. For the quantitative analysis, we determine the radially averaged $g_2(r,t)$ as a function of the radial coordinate r. Fig. 5.4a shows that the spatial structure associated with the oscillatory behaviour of $g_2(r,t)$ emerges as the clouds expand, and is absent for in-trap measurements. We fit the measurements at finite t with the predictions of Eq. 5.20 for the superfluid phase to determine the superfluid exponent η and the short-range cutoff a. The superfluid model describes our measurements well, with consistent values of $\eta \simeq 0.04$ and $a \simeq 3\,\mu\text{m}$ for all three expansion times as expected for the same in-situ system parameters, see Figs. 5.4b and c. To further corroborate the expansion scaling, we compare the locations r_1 of the first minimum of $\tilde{g}_2(r,t)$ with the mean-field prediction ${r_1}^2 = 3\pi\hbar t/m$ [51–53] and the predictions of the superfluid model, see inset of Fig. 5.4a.

Having verified the expansion scaling behaviour, we perform measurements across the BKT critical point, both with single and uncoupled bilayer 2D clouds. In Fig. 5.5a, we show the measurements of $\tilde{g}_2(r)$ for single-layer clouds at varying $\mathcal{D}$. As $\mathcal{D}$ is lowered, the oscillatory feature of the noise correlations, characteristic of the superfluid phase, vanishes indicating a crossover to the normal phase. To verify this we fit the measurements to Eq. 5.20 calculated for both the superfluid and

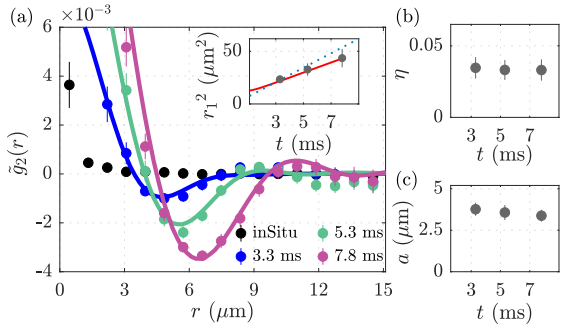


Figure 5.4: Expansion scaling behaviour. (a) Radially averaged correlation function $\tilde{g}_2(r,t)$ is shown for trapped single-layer clouds with no expansion (in-situ) and after $t = 3.3$, 5.3 and 7.8 ms. Error bars are the standard error. Solid lines are the best fits based on Eq. 5.20 for the superfluid phase, from which we determine the superfluid exponent η and the short-range cutoff a needed to regularise the correlation functions [53]. Inset shows the squared locations r_1^2 of the first minimum of the correlation function (dots), together with the mean-field prediction ${r_1}^2 \propto t$ (dashed line). The solid line shows the analytical prediction of the minimum position in the superfluid phase based on Eq. 5.20, including the effect of finite imaging resolution encoded in the short-range cutoff. (b, c) Extracted values of η and a.

normal phases as shown in Figs. 5.5b-c for both large and small $\mathcal{D}$; for $\mathcal{D} = 16.8$ the prediction for the superfluid phase gives a better fit, whereas for $\mathcal{D} = 5.7$ it is the normal phase. Similar to earlier work [6] we determine the BKT crossover point as being the value of $\mathcal{D}$ at which the goodness of the fit of the exponential model overtakes the algebraically decaying model, see inset of Fig. 5.5c. This gives the crossover point at $\mathcal{D}_c = 9.1(9)$, in close agreement with the theoretical prediction $\mathcal{D}_{c,th} = 8.6$ [63].

In Fig. 5.5d we show the measurements of our bilayer systems at varying $\mathcal{D}$. Similar to the single-layer case, the noise correlations are oscillatory at large $\mathcal{D}$, however, correlations fall off over short distance in the normal regime at small $\mathcal{D}$. For a decoupled bilayer the noise correlation function is Eq. 5.19. As in the case for the density noise from a single layer we calculate the predictions of Eq. 5.19 for the superfluid and normal regimes and use them to fit our bilayer noise correlations to determine the exponent η and the BKT crossover, see Figs. 5.5d-f. The BKT crossover occurs at $\mathcal{D}_c = 9.0(6)$, in agreement with the results of the single layer behaviour and the theoretical prediction [63]. Combined with the relative-mode

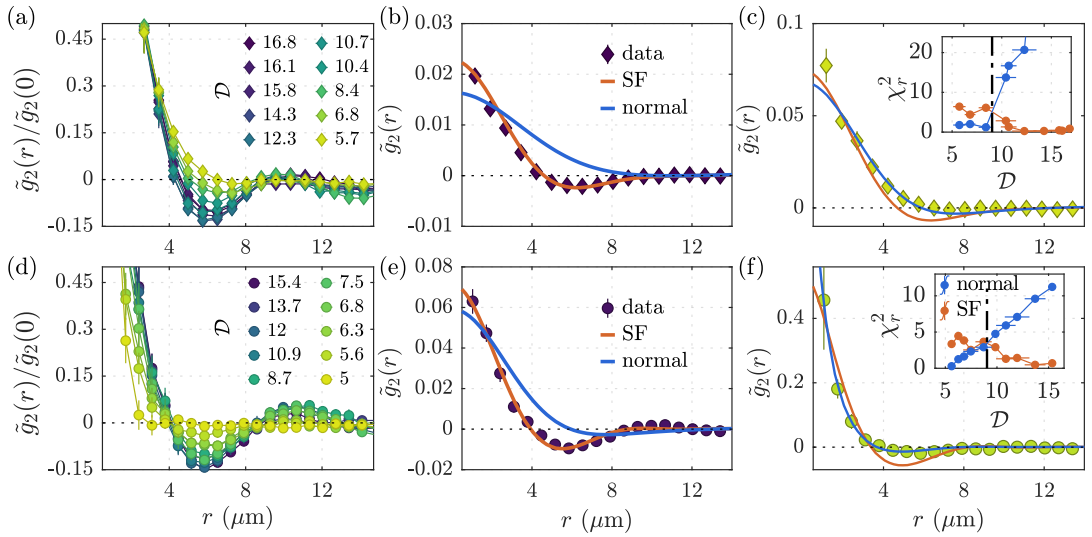


Figure 5.5: Noise correlations of single layer and bilayer 2D Bose gases across the BKT transition. (a) $\tilde{g}_2(r)$, scaled by the value at origin $\tilde{g}_2(0)$, for $t = 5.3$ ms for single-layer clouds having phase-space densities between $\mathcal{D} = 5.7$ and 16.8. Lines are guides to the eye and error bars are the standard error. (b) $\tilde{g}_2(r)$ at $\mathcal{D} = 16.8$, plotted together with best fits of superfluid (SF, orange) and normal phase (blue) based on Eq. 5.20. (c) Measurement at $\mathcal{D} = 5.7$ is well described by the prediction for the normal phase. Inset shows the reduced χ^2 statistics of the superfluid and normal-phase fitting models at varying $\mathcal{D}$ (values for the normal phase at high $\mathcal{D}$ with $\chi_r^2 > 20$ are not shown). The crossover from superfluid to normal phase is identified by the point (vertical dashed line) beyond which $\tilde{g}_2(r)$ is better described by the normal-phase model at small $\mathcal{D}$. This yields the crossover at $\mathcal{D}_c = 9.1(9)$. (d) Measurements after $t = 5.3$ ms for bilayer clouds with phase-space densities between $\mathcal{D} = 5$ and 15.4. (e) $\tilde{g}_2(r)$ and their fitted curves at $\mathcal{D} = 15.4$. (f) The measurement at $\mathcal{D} = 5.6$ is better described by the normal-phase model, similarly to the single-layer case at small $\mathcal{D}$ in panel (c). Inset showing the χ_r^2 errors of the fitting model, whose intersection gives the BKT crossover at $\mathcal{D}_c = 9.0(6)$ (vertical dash-dotted line).

phase correlation measurements using matter-wave homodyning [5, 6], this method gives a complete characterisation of phase fluctuations of bilayer systems.

In Fig. 5.6 we consolidate the results for single and bilayer 2D clouds. The measured value of η scales linearly with the inverse phase-space density $\mathcal{D}^{-1}$ in the superfluid regime, in accordance with the Nelson-Kosterlitz relation $\eta \propto \mathcal{D}^{-1}$ [6, 64]. There is a deviation from this linear behaviour when the system approaches the crossover regime at $\mathcal{D}^{-1} = 0.11(1)$, as predicted [6]: in the normal phase above the broad crossover regime η shows a faster increase within the measurement uncertainty. The determination of η is less accurate in the normal regime since the correlations are short ranged and better described by exponential scaling. We

also show values of η obtained from the relative-phase correlation measurements [6, 47], which agree with the results of the noise measurements.

The location r_1 of the first minimum of the measured noise correlation function $g_2(r,t)$ scales with the expansion time t as $r_1^2 \propto t$. This confirms the expansion scaling and demonstrates that the determined values of the superfluid exponent and the BKT critical point are independent of the expansion time. Furthermore, the noise interferometry of expanded bilayer systems, derived above, is a new readout technique for ultracold gas experiments providing access to the coherence of the common-mode phase correlations, which we benchmarked by exploiting the fact that, in the absence of interlayer coupling, they exhibit the same statistics as the relative-mode correlations.

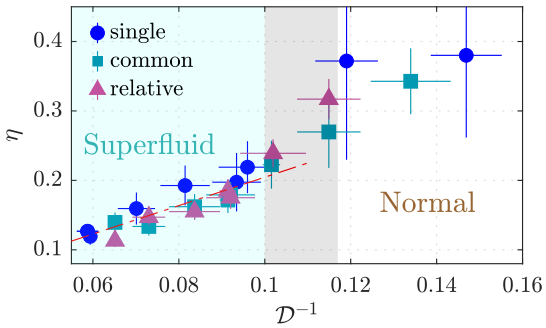


Figure 5.6: The BKT crossover in 2D Bose gases. The algebraic exponent η is plotted as a function of the inverse phase-space density $\mathcal{D}^{-1}$. Results for a single layer (circles) and bilayer (squares) are compared against the measurements (triangles) of the relative-phase correlations [47]. Red dash-dotted line is the Nelson-Kosterlitz relation $\eta \propto \mathcal{D}^{-1}$, expected in the superfluid regime [64]. The crossover region (black shaded area) is at $\mathcal{D}^{-1} = 0.11(1)$, corresponding to a critical algebraic exponent $\eta_c \sim 0.2$ as expected for a finite-sized system [6]. Above the critical point, values of η have increased uncertainty as the in-situ phase correlations become short ranged.

The spatial noise interferometry method presented in this chapter is especially useful in conjunction with the direct matter-wave interferometric probe of the relative phase mode. For instance, superfluid phases arising from coherent coupling of bilayer 2D quantum systems, where the excitations are naturally expressed in terms of relative and common modes where these modes are expected to exhibit qualitatively distinct features, represent a class of novel composite orders, described in Ch. 6.

5.3 Outlook

The readout from density noise patterns after short TOF that we have developed in this work, alongside later independent work on 1D Bose gases [56] can be developed further into improved readout schemes for tunnel-coupled 2D Bose gases. In particular, density noise readout from 2D bilayers provides a way to probe the topological excitations and solitons arising in the sine-Gordon model, these are of great interest since in certain parameter regimes they act as a dissipation channel, as studied numerically by En Chang in his DPhil thesis [48]. To study these features that appear as lines in the images taken of the coupled bilayers would require the 2D readout provided by short-TOF density noise.

5.3.1 Reconstruction using images at different times

Considering that a single image of the 2D density distribution, provides a single real-valued 2D field it does not contain enough information to uniquely infer two real 2D fields of the same size corresponding to the phase and density of the condensate wavefunction, for arbitrary phase and density. This follows from the pigeon-hole principle, if certain combinations of the in-situ density and phase fields map to the same configuration of the single 2D density field after free propagation. Work has been successful in 1D on reconstructing the 1D phase field from the density noise by assuming weak in-situ density fluctuations and imposing physical constraints including a lack of vorticity [56]. However in 2D the physics of the BKT transition relies on vorticity and the vortices are clearly visible in the density patterns after a short TOF as shown in earlier work by the group [65]; so based on the limited information in the image we naively expect the technique used for 1D would struggle with single-shot reconstruction in 2D near the BKT transition.

However, a different approach might work, namely obtaining two separate snapshots of the 2D density field after free expansion, with a known evolution between them, provides information about two real-valued 2D fields and thus giving us a chance of reconstructing the in-situ density and phase fields, which are also two 2D fields.

The free evolution of the macroscopic wavefunction is precisely the same as that for light in classical optics, a fact that has been used in other work on defocused readout from cold atom experiments [55]. As such the problem of reconstructing the in-situ density and phase fields from observations at different times maps to reconstructing the amplitude and phase from the intensity of a defocused image from two images with different known distances from the focus [66]. For this problem it has been shown that, under general conditions, such a reconstruction is unique up to a global phase [67]. This means that it should, in theory, be possible to achieve single-shot reconstruction of the in-situ density and phase fields of the 2D macroscopic wavefunction provided two images of the density noise taken after different lengths of time-of-flight.

The practicalities of our imaging system present a concern regarding how this might be achieved as the cloud only falls through the focal plane once. However, since the MRF states get projected into the different M_F states at the start of the TOF evolution, the high- and low-field seeking states and the $M_F = 0$ state pass through the focal plane at different times. Thus, it should be possible to reconstruct the 2D phase and density field from images of the clouds of atoms in different Zeeman states, with corrections to account for their differing expansion in the evolution when the magnetic field is still applied. The evolution of the different M_F states during TOF, taking into account the RF and DC magnetic field turn-off sequence, was studied numerically by Abel Beregi, as reported in an appendix of his DPhil thesis [18]. Such a sophisticated readout technique would allow extraction of higher moments of the phase and density distribution and studying higher-order correlators in a single layer. Additionally a readout scheme utilising the information from different M_F states to solve a phase-retrieval problem would result in significantly more local information per experimental run, as currently we only read out a 1D slice of the 2D relative phase field.

6

Coupled Two-Dimensional Bilayers

This chapter is adapted from work which has since been published [34].

Coherent Josephson tunnelling between macroscopic quantum systems is an important paradigm that is the foundation for various quantum technologies [68, 69]. The interplay between coupling-induced coherence and the intrinsic fluctuations of low-dimensional constituent systems gives rise to a rich variety of quantum many-body phenomena [70, 71]. In bilayer two-dimensional (2D) systems, this coupling can induce a transition to an interlayer superfluid state. This transition modifies the superfluid-normal transition observed in uncoupled systems, which is governed by the unbinding of vortex-antivortex pairs, known as the Berezinskii-Kosterlitz-Thouless (BKT) transition [72, 73] as described in Ch. 4. Such a bilayer system serves as a model with potential significance for understanding high-temperature superconductivity [9, 74, 75], including optically pumped superconductivity [10, 11], twisted bilayer graphene [76, 77], and dipolar particles with competing repulsive intra-plane and attractive inter-plane interactions [78, 79]. Furthermore, novel phases are expected to emerge from the ordering of relative or common degrees of freedom, and there is strong interest in both the static and dynamic properties

of these phases [58, 80–87]. Several studies predicted the existence of a coupling-induced superfluid phase [58, 88] as well as a paired BKT superfluid phase [87, 89, 90], though these predictions were largely unexplored experimentally prior to the work reported in this chapter.

Ultracold atom systems offer an exemplary platform for studying coupled many-body systems, thanks to their exquisite control over coherent quantum tunnelling combined with the ability to directly probe many-body states. A key technique in cold-atom systems is matter-wave interferometry since it provides a direct probe of relative phase fluctuations [5, 6]. In addition, the development of noise interferometry [47, 53], as described in Ch. 5, enables measurements determining common-mode correlation properties from the density-noise patterns appearing in expanded bilayer 2D systems. Although trapping of 1D and 3D quantum gases in controllable double-well potentials has been used to investigate coupled systems [91, 92], the work covered in this chapter represents the first experimental realisation of a tunable double-layer continuous 2D system using cold atoms [34].

This chapter covers the creation of a highly controllable bilayer of 2D Bose gases coupled via Josephson tunnelling and detailed measurements of its correlation properties using matter-wave and noise interferometry, to probe both relative and common degrees of freedom. We fit the correlation function with algebraic and exponential models to identify the superfluid-normal transition, which manifests as a coupling-dependent crossover. This allows us to detect the emergence of a double-layer superfluid (DLSF) phase and trace the corresponding phase diagram, which agrees with renormalisation-group (RG) analysis of the bilayer XY model [58, 81] and Monte Carlo simulations. The microscopic origin of this emergent phase is the suppression of vortex unbinding, which is confirmed through direct measurements of free vortices in the relative-phase mode.

6.1 Theoretical Background

In a bilayer system the possibility that a particle might tunnel from one layer to another can be incorporated into the Hamiltonian with a hopping term

$$H_{1,2} = -J \int d\boldsymbol{r}^d (\Psi_1^\dagger(\boldsymbol{r})\Psi_2(\boldsymbol{r}) - \Psi_2^\dagger(\boldsymbol{r})\Psi_1(\boldsymbol{r})) \tag{6.1}$$

written using the creation and annihilation operators for layer $1, 2$ respectively. Replacing the operators with classical fields and using the density-phase representation one obtains

$$\begin{aligned} H_{1,2} &= -J \int d\boldsymbol{r}^d \sqrt{n_1}(\boldsymbol{r})\sqrt{n_2}(\boldsymbol{r}) e^{i(\theta_2(r)-\theta_1(r))} - \sqrt{n_1}(\boldsymbol{r})\sqrt{n_2}(\boldsymbol{r}) e^{(\theta_1(r)-\theta_2(r))} \\ &= -J \int d\boldsymbol{r}^d \sqrt{n_1}(\boldsymbol{r})\sqrt{n_2}(\boldsymbol{r}) 2\cos\left(\theta_1(\boldsymbol{r}) - \theta_2(\boldsymbol{r})\right). \end{aligned} \tag{6.2}$$

The term which arises featuring the cosine of the relative phase between the layers matches the form of the in-plane Hamiltonian in the XY model, as expected from the isotropy of space. The complete Hamiltonian for the coupled bilayer system is thus

$$H = \int dr^2 \left[\sum_{j=1}^{2} \left(\frac{\hbar^2}{2m} (\nabla\psi^*(\boldsymbol{r})_j)(\nabla\psi(\boldsymbol{r})_j) + \frac{g}{2}\psi^*(\boldsymbol{r})_j\psi^*(\boldsymbol{r})_j\psi(\boldsymbol{r})_j\psi(\boldsymbol{r})_j \right) \right] + H_{1,2} \tag{6.3}$$

When parametrised in terms of the relative and common phase $\theta_{s/a}(\boldsymbol{r}) = \theta_1(\boldsymbol{r}) \pm \theta_2(\boldsymbol{r})$ and considering small density perturbations in these modes $\delta n_{s/a}(\boldsymbol{r}) = \delta n_1(\boldsymbol{r}) \pm \delta n_2(\boldsymbol{r}))$ the combined Hamiltonian can be written as:

$$\begin{aligned} H = &\int dr^2 \left[\sum_{j=a,s} \left(\frac{n\hbar^2}{4m} (\nabla\theta_j(\boldsymbol{r}))^2 + \frac{\hbar^2}{4m} n (\nabla\delta n_j(\boldsymbol{r}))^2 + g n^2 (\delta n_j(\boldsymbol{r}))^2 \right) \right] \\ &- J \int d\boldsymbol{r}^d n \sqrt{1 + 2\delta n_s(\boldsymbol{r}) + \delta n_s(\boldsymbol{r})^2 + \delta n_a(\boldsymbol{r})^2} 2\cos\left(\theta_a(\boldsymbol{r})\right) \end{aligned} \tag{6.4}$$

In the limit of negligible density fluctuations, it is clear that the common and relative modes provide a natural basis for the excitations. Written in terms of relative and common phase fluctuations the Hamiltonian factors cleanly into two uncoupled Hamiltonians for the relative and common phase fields [35]

$$\begin{aligned} H &= \int dr^2 \frac{n\hbar^2}{4m} (\nabla\theta_s(\boldsymbol{r}))^2 + \int dr^2 \frac{n\hbar^2}{4m} (\nabla\theta_a(\boldsymbol{r}))^2 - 2J \int d\boldsymbol{r}^d n \cos\left(\theta_a(\boldsymbol{r})\right) \\ &= H_s + H_a \end{aligned} \tag{6.5}$$

Where we note that tunnel-coupling breaks the $U(1)$ symmetry in the relative phase, while the Hamiltonian for the common phase fluctuations has the same form as for a single isolated layer but rescaled by a factor of $1/2$. We also note that in the limit of the inter-layer coupling J going to infinity, the cosine term in the

Hamiltonian for the relative excitations will lock the relative phase to 0 everywhere. We therefore expect the layers to be phase-locked in the strong coupling limit. This has the effect of the common phase behaving like a single layer with double the density, as any fluctuations have to drag around both layers. So in the infinite coupling limit the BKT transition in the common mode should occur at half the PSD at which it occurs in the uncoupled case.

Between these two trivial limits there is a complicated interplay between the relative and common modes and the inter-layer coupling term giving rise to a non-trivial phase diagram. As J increases the system undergoes a crossover to a double-layer superfluid phase, where the broken U(1) symmetry and increased energy cost of fluctuations due to the tunnel-coupling shifts the transition temperature to higher temperatures and suppresses the formation of vortices, especially in the relative phase field.

6.1.1 Renormalisation-group analysis

The analytical prediction for the phase diagram in Fig. 6.2b and Fig. 6.5 is based on the renormalisation-group equations for coupled 2D superfluids derived in Refs. [58, 81]. As introduced in Ch. 2 such RG equations relate the effective system parameters at varying length scales l, and in this case provide a universal description of the DLSF phase and its transitions. The behaviour depends on the following quantities: the temperature energy scale T', the interlayer coupling $J_\perp$, the stiffness of symmetric and antisymmetric phase fluctuations, $J_{s/a} = J \pm J_{int}$, the single vortex fugacity $A_1 \sim Je^{-J}$, and corresponding fugacities for symmetric and antisymmetric

vortex pairs A_s and A_a [58]

$$\begin{aligned}
\frac{dJ_\perp}{dl} &= \left(2 - \frac{T'}{2\pi J_a}\right) J_\perp, \\
\frac{dA_s}{dl} &= \left(2 - 2\pi\frac{J_s}{T'}\right) A_s + \alpha_3 \frac{A_1^2(J_a - J_s)}{2T'^2}, \\
\frac{dA_a}{dl} &= \left(2 - 2\pi\frac{J_a}{T'}\right) A_a + \alpha_3 \frac{A_1^2(J_s - J_a)}{2T'^2}, \\
\frac{dA_1}{dl} &= \left(2 - \frac{\pi(J_s + J_a)}{2T'} + \alpha_3 \frac{A_s J_s + A_a J_a}{T'^2}\right) A_1, \\
\frac{dJ_a}{dl} &= \alpha_2 \left(\frac{J_\perp^2}{4\pi^4 J_a} - 4\frac{A_a^2}{T'^4} J_a^3 - \frac{A_1^2}{2T'^4}(J_s + J_a) J_a^2\right), \\
\frac{dJ_s}{dl} &= -\alpha_2 \left(2\frac{A_s^2}{T'^4} J_s^2 + \frac{A_1^2}{4T'^4}(J_s + J_a) J_s\right) 2J_s,
\end{aligned} \tag{6.6}$$

where α_2 and α_3 are dimensionless non-universal constants. We identify the crossover for common and relative modes shown in Fig. 6.5, from the behaviour of J_s and J_a respectively, after integrating Eqs. 6.6 for Δl, as we vary the $\mathcal{D}$: the transition is labelled at the $\mathcal{D}$ where the dimensionless stiffnesses $\tilde{J}_{s/a} = J_{s/a}\pi/T'$ suddenly drop below a certain value; we chose $\tilde{J}_{s/a} = 10^{-1}$ for this work, the precise value chosen does not affect the phase diagram significantly as the stiffnesses jump by orders of magnitude at the transition under RG flow (Fig. 6.1). We used Bayesian optimisation to identify the non-universal RG parameter values for our system, reported in Fig. 6.1 caption, where the cost function is defined as the χ^2 distance between the RG phase diagram and the Monte Carlo simulation results.

The RG analysis in this work, using the coupled equations Eqs. 6.6 is perturbative in the vortex fugacities and tunnelling energy. The good agreement between the RG predictions and the experiment for relative modes, and the slight deviations between the RG and experiment for the common mode (while exhibiting the same qualitative features) shown in Fig. 6.5 may indicate that potential improvements should be made to the RG equations by incorporating higher-order terms. This may be carried out by collaborators in future theoretical work.

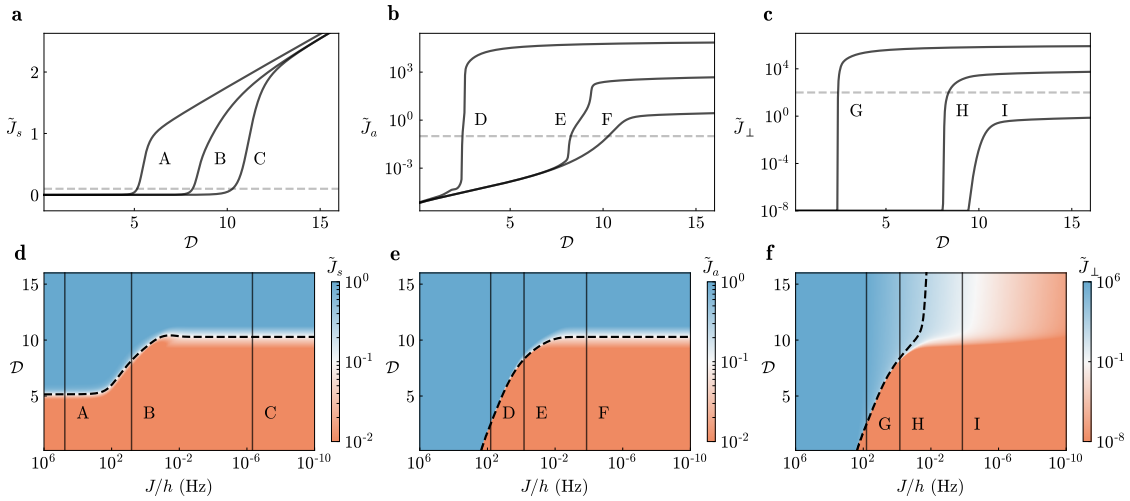


Figure 6.1: Renormalisation-group results for the phase stiffness in bilayers. The Renormalisation-group theory analysis was carried out using the numerical integration of Eqs. 6.6, with $T' = 208$ Hz, $A_{1,0} = 0.345T'/\pi$ and $J_{s,0} = J_{a,0} = \mathcal{D}T'/(5.5\pi)$, $A_{a,0} = A_{s,0} = A_{1,0}$, constants $\alpha_2 = 5.7$, $\alpha_3 = 0.1$ and $\Delta l = 7$. **a,b.** The values of the dimensionless phase stiffnesses $\tilde{J}_{s,a} = \pi J_{a,s}/T'$ at the end of integration at different coupling strengths. Dashed lines denote the 10^{-1} dimensionless cutoff chosen to distinguish between the superfluid and disordered phases. **c.** Value of the dimensionless interlayer coupling strength $\tilde{J}_\perp = \pi J_\perp/T'$, at the end of RG integration, dashed line denotes $\tilde{J}_\perp = 10^2$. **d,e.** The values of $\tilde{J}_s$ and $\tilde{J}_a$ after RG integration. The contour lines (dashed) are where the values of the stiffnesses cross 10^{-1} which we identify as the critical point for a given value of J. **f.** Value of $\tilde{J}_\perp$ at the end of RG integration. In the DLSF and ASF phases $\tilde{J}_\perp \gg 1$ under RG, the dashed contour shows where $\tilde{J}_\perp$ crosses 10^2.

6.2 Experimental Procedure

This investigation utilised the older generation experiment described in Ch. 2. A cloud of ^{87}Rb atoms is confined in a cylindrically-symmetric 2D trap formed by a box-like potential of radius 20 μm in the horizontal plane and a double-well potential in the vertical z direction [60, 93]. Strong vertical confinement in the double-well is created with the multiple-RF (MRF) dressing technique, while the horizontal trapping comes from the dipole force of a strong off-resonant laser beam that is spatially shaped by a digital micromirror device (DMD) into a ring-shaped intensity distribution [47, 94] (Fig. 6.2a).

Atoms are loaded with equal populations in each of the wells at a temperature of $T = 50\,\mathrm{nK}$, set by forced evaporation. In each well the vertical trap frequency is $\omega_z/2\pi = 1.2\,\mathrm{kHz}$ so that the quasi-2D conditions $\hbar\omega_z > k_B T$ and $\hbar\omega_z > \mu$ are

satisfied, where $\hbar$ is the reduced Planck constant, k_B the Boltzmann constant and μ is the chemical potential. The characteristic dimensionless 2D interaction strength is $\tilde{g} = \sqrt{8\pi}a_s/\ell_0 = 0.08$, where a_s is the s-wave scattering length and $\ell_0 = \sqrt{\hbar/(m\omega_z)}$ is the harmonic oscillator length along z for an atom of mass m.

The MRF-dressed double-well potential is created using RF magnetic fields with three frequency components applied to atoms in a static magnetic field gradient as described in Ch. 2. The separation of the two potential minima along the z direction is determined by the frequency difference between the RF components. The high controllability and stability of the RF fields allow precise tuning of the inter-well distance d, thereby creating a bilayer system with tunable coupling strength J (Fig. 6.2a). The interlayer coupling shifts the vortex binding-unbinding critical point, as illustrated in Fig. 6.2b, based on the RG theory presented above and in Refs. [58, 81]. This emergent phenomenon affects both antisymmetric (relative) and symmetric (common) phase modes of the system defined as $\theta = \phi_1 - \phi_2$ and $\varphi = \phi_1 + \phi_2$, respectively, where $\phi_i = \arg(\Psi_i)$ is the argument of the order parameter Ψ_i for layer i (i=1,2). The relative and common modes of the systems are known to provide a natural basis for excitations in two-mode low-dimensional quantum gases [71, 95], including the coupled bilayer systems [58].

The spatial coherence of both phase modes is probed using time-of-flight (TOF) expansion of the two clouds, combined with a spatially selective imaging technique along orthogonal directions, as schematically shown in Figs. 6.2c and d. For the relative mode, the trap is abruptly turned off, releasing the pair of 2D gases for a TOF duration of $t_{\mathrm{TOF}}^{\mathrm{rel}} = 17\,\mathrm{ms}$. Once released, the two clouds expand rapidly along the z direction [96] and overlap, forming an interference pattern along z (Fig. 6.2c), whose phase encodes fluctuations of the relative mode [6, 43]. We then apply a thin sheet of laser light to optically pump atoms from the lower to the upper hyperfine level in a slice of thickness $L_y = 5\,\mu\mathrm{m}$ along the y direction (red transparent sheet in Fig. 6.2c) and image the atoms in the $F = 2$ hyperfine level using resonant light [60]. From the interference image we determine the local relative phase $\theta(x)$, and from a set of measurements of $\theta(x)$ we calculate the relative phase correlation function.

To probe the common mode, we use a short TOF of duration $t_{\mathrm{TOF}}^{\mathrm{com}} = 5.3\,\mathrm{ms}$ and record the density-noise patterns after expansion (see Fig. 6.2d), as introduced in Ch. 5. In this method, self-interference within and between the clouds transforms initial phase fluctuations into density modulations [50, 51, 53, 97, 98]. This short-TOF technique has been applied to measure phase coherence in low-dimensional gases in several experiments [47, 49, 99], and for our density-balanced bilayer, it measures the fluctuations of the common mode, as demonstrated in [47] and Ch. 5. We perform selective repumping of the atoms using a horizontal sheet of thickness $L_z = 5\,\mu\mathrm{m}$, and image the resulting density distribution $n(x, y)$ with a high-resolution imaging system with optical axis along the z direction (Fig. 6.2d). The selective imaging is necessary because the extent of the cloud after TOF expansion exceeds the depth of focus of the imaging system [47, 61].

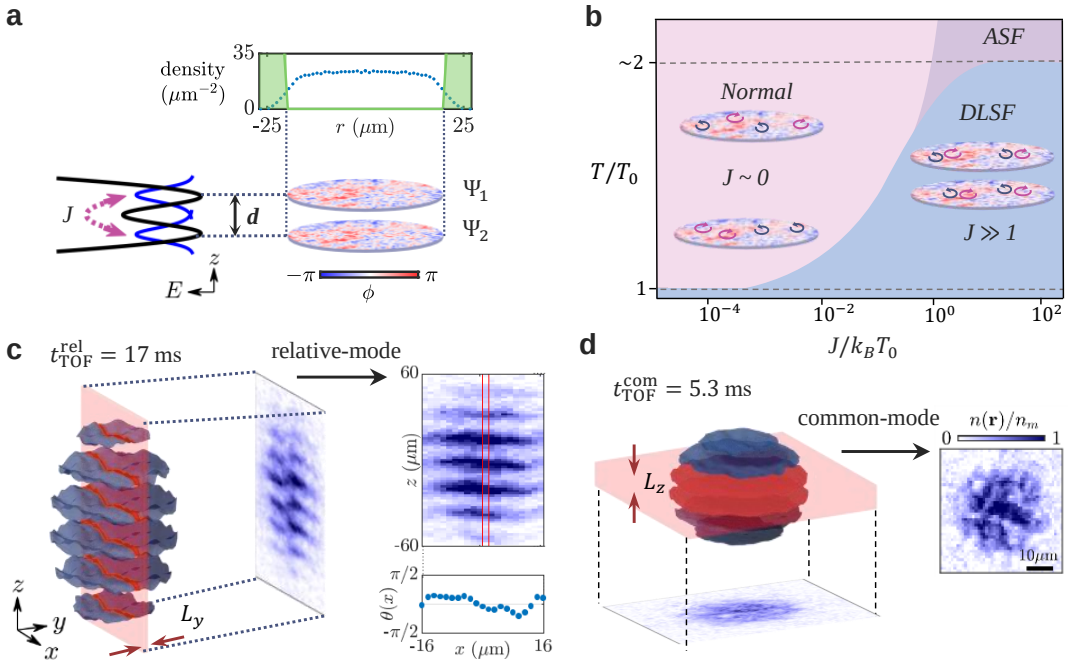


Figure 6.2: Formation of a bilayer quasi-2D Bose gas and its characterisation by matter-wave interferometry. a. Two near-homogeneous clouds of ^{87}Rb atoms (represented by wave functions Ψ_1 and Ψ_2, with complex phases ϕ) are trapped in a double-well potential, where the inter-well distance d is controlled using a multiple-RF dressing technique; see text. This results in a bilayer system with a tunable interlayer coupling J. The top panel shows the radially averaged density profile, obtained from a single in-situ image taken along the z direction. The green-shaded region indicates the box potential shape, which is created by a ring-shaped, blue-detuned laser beam. **b.** The phase diagram of our coupled bilayer system based on theoretical work: RG analysis and Monte Carlo simulation. Increasing the interlayer coupling J increases the transition temperature T, towards $T/T_0 \sim 2$ [58, 87], where T_0 denotes the transition temperature for $J = 0$. Illustrations show unbound vortex pairs in the normal phase and bound vortex pairs in the double-layer superfluid (DLSF) phase. In the anti-symmetric superfluid (ASF) phase vortices are bound in the relative-mode but unbound in the common-mode [58]. **c.** Clouds released from the trap undergo a time-of-flight (TOF) expansion for a duration of $t_{\mathrm{TOF}}^{\mathrm{rel}} = 17$ ms, so that they overlap producing interference fringes (blue wavy planes) encoding the local relative phase fluctuations. The interference pattern is recorded by selectively imaging atoms within a thin slice of thickness $L_y = 5\,\mu$m (shown as a red sheet; see text). The column interference profiles at different x allow us to extract the local relative phase $\theta(x)$. **d.** After a short TOF of $t_{\mathrm{TOF}}^{\mathrm{com}} = 5.3$ ms, the in-plane density distribution, $n(\boldsymbol{r})$, is imaged from below using a selective imaging technique (thin repumping sheet with thickness $L_z = 5\,\mu$m). Image on the right displays $n(\boldsymbol{r})/n_m$, where n_m is the maximum density.

6.3 Results

We explore a range of interlayer coupling strengths, from J/h below 10^{-3} to 10 Hz, by varying the inter-well distance d from 1.7 to 5.9 µm. By adjusting the total atom number N from 2×10^4 to 9×10^4 we cover a wide range of phase-space density (PSD), $\mathcal{D} = n\lambda_{\mathrm{th}}^2$, where n is the 2D atom density in each cloud, and $\lambda_{\mathrm{th}} = h/\sqrt{2\pi m k_B T}$ is the thermal de Broglie wavelength. For each combination of d and N, the experiment is repeated to collect an ensemble of images using both relative and common detection techniques. From these measurements of $\theta(x)$ and $n(x, y)$ the correlation functions are computed as described below. We average over up to 60 experimental repetitions for each set of d and $\mathcal{D}$.

The real part of the two-point relative-phase correlation function is defined as $C(x, x') = \mathrm{Re}[\langle e^{i[\theta(x)-\theta(x')]}\rangle]$, where $\theta(x)$ is the phase of the relative mode. Throughout this chapter, $\langle..\rangle$ denotes the statistical average over experimental repetitions. A value of $C(x, x') = 1$ indicates perfect coherence, while $C(x, x') = 0$ implies no coherence. In Fig. 6.3a, we plot $C(x, x')$ for an inter-well distance of $d = 1.7$ µm at two different phase-space densities $\mathcal{D} = 6.5$ and 3.4. For small $\mathcal{D}$, phase coherence decays rapidly over large distances. To quantify this, we calculate the correlation function $C(\overline{x}) = \mathrm{Re}[\langle e^{i[\theta(x)-\theta(x-\overline{x})]}\rangle_x]$ as a function of separation $\overline{x} = x - x'$, where $\langle..\rangle_x$ denotes both the statistical average and an average over the coordinate x. This analysis is performed using $\theta(x)$ obtained as illustrated in Fig. 6.2c restricted to the central region of the cloud. Fig. 6.3b, shows that $C(\overline{x})$ decays more rapidly with distance as $\mathcal{D}$ decreases, indicating a transition from quasi-long-range order to short-range phase coherence. To identify the critical point, we fit the data with both algebraic and exponential decay models (solid and dashed lines). The reduced chi-squared value, χ_r^2, of the exponential fit increases significantly beyond a certain point, crossing the χ_r^2 statistic for the algebraic fit. We identify this crossing as the critical value $\mathcal{D}_c$ (inset of Fig. 6.3b). For $d = 1.7$ µm, corresponding to the coupling strength $J/h \simeq 30$ Hz, we determine $\mathcal{D}_c = 4.8(6)$ from the relative phase. This is lower than the critical value $\mathcal{D}_c(0) = 10(1)$ observed in the uncoupled system at $J/h \ll 1$ Hz.

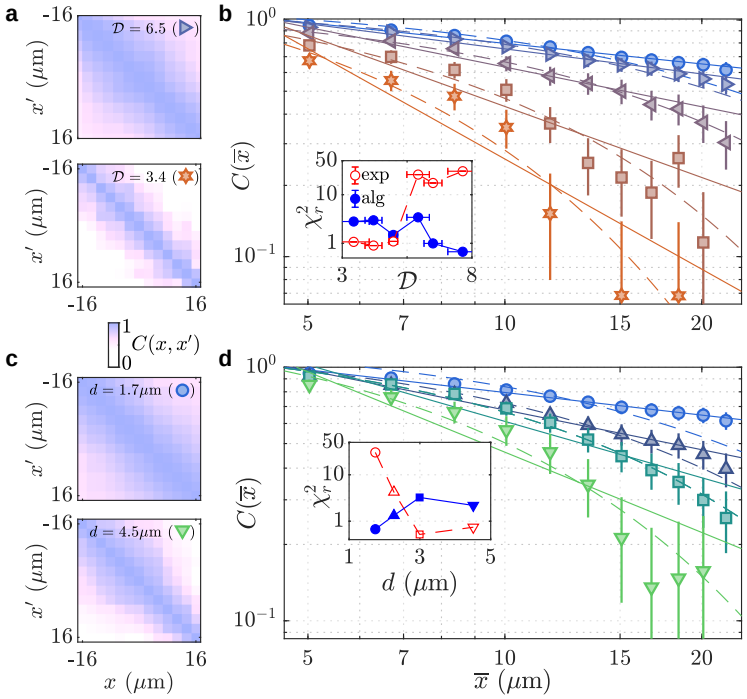


Figure 6.3: Phase coherence of the relative mode in the coupled bilayer. a. Two-point relative-phase correlation function $C(x, x')$ is shown for phase-space densities $\mathcal{D} = 6.5$ and 3.4, with an inter-well distance of $d = 1.7\,\mu$m. **b.** Correlation function $C(\bar{x})$ plotted as a function of the distance $\bar{x} = x - x'$, measured at $d = 1.7\,\mu$m for five different values of $\mathcal{D} = 7.6, 5.9, 5.0, 4.2$ and 3.4 (from top to bottom). **c.** $C(x, x')$ is shown for $\mathcal{D} = 7.5$, with inter-well distances of $d = 1.7\,\mu$m and $4.5\,\mu$m. **d.** $C(\bar{x})$ is measured at $\mathcal{D} = 7.5$ for four inter-well distances $d = 1.7,\ 2.3,\ 3.0$ and $4.5\,\mu$m (from top to bottom). In **b** and **d**, solid lines represent fits using an algebraic model, while dashed lines represent exponential model fits. Insets show χ_r^2 values for the algebraic (filled symbols) and exponential (open symbols) fit models.

To assess the effect of coupling on the phase coherence, we also perform measurements for varying d at fixed $\mathcal{D}$. In Fig. 6.3c, the measurements of $C(x, x')$ at two different values of d clearly indicate a fast-decaying correlation at large distance $\bar{x}$ when d is increased. In Fig. 6.3d, the correlation functions for four distinct d values show a coupling-induced crossover from algebraic to exponential phase-coherence decay. This is confirmed by fits to the two models (inset). The transition occurs around $d \simeq 2.5\,\mu$m, or equivalently $J/h \simeq 10\,$Hz for our system, with $\mathcal{D} \simeq 7.5$. For comparison, the effective in-plane coupling strength is $\sim 100\,$Hz, based on the energy scale set by the transition temperature using Eq. 4.8 and Eq. 4.14. Despite $\mathcal{D}$ being below $\mathcal{D}_c(0)$, stronger coupling suppresses

phase fluctuations, enforcing algebraic order.

Let us now consider the information that can be deduced from the noise-correlation function after free expansion $g_2(\boldsymbol{r}) = \langle \tilde{n}(\boldsymbol{r})\tilde{n}(\boldsymbol{r}-\boldsymbol{r}_0)\rangle_{\boldsymbol{r}_0}$, with $\langle..\rangle_{\boldsymbol{r}_0}$ indicating statistical averaging and spatial averaging over $\boldsymbol{r}_0$ and $\tilde{n}(\boldsymbol{r}) = \delta n(\boldsymbol{r})/\bar{n}(\boldsymbol{r})$ being the normalised in-plane density distribution after a short TOF expansion (see Fig. 6.2d); $\delta n(\boldsymbol{r}) = n(\boldsymbol{r}) - \bar{n}(\boldsymbol{r})$, with $\bar{n}(\boldsymbol{r}) \equiv \langle n(\boldsymbol{r})\rangle$ being the average over many experimental realisations. For bilayer systems, the spatial autocorrelations of the density distribution after TOF encode the spatial coherence of the in-situ common-mode phase [47]. Using this approach, we deduce comprehensive information about correlations of the common-mode phase from the experimental data, including their functional form and values of the parameters.

Figs. 6.4a and b show the measurements of the density correlation function for the bilayer system at two different values of $\mathcal{D}$. At higher $\mathcal{D}$, a negative ring-like structure is visible, but this feature disappears at lower $\mathcal{D}$. This structure arises from the quasi-long-range order of the superfluid phase, which vanishes when the spatial coherence of the phase decays exponentially in the normal phase [47, 53]. We theoretically calculate the noise-correlation function for expanding clouds below and above the BKT transition, which we fit to our measurements to characterise the phase of the system (Fig. 6.4c). At PSDs much lower than the critical value $\mathcal{D} \lesssim 4$, the increase of in-situ density fluctuations affects the measurement as indicated by the gray-shaded region in the inset of Fig. 6.4c. By repeating this analysis for various values of $\mathcal{D}$, we determine the critical value $\mathcal{D}_c$ for our bilayer system at varying coupling strengths. Furthermore, this analysis allows us to extract the algebraic exponent η of the superfluid phase, shown for two different inter-well distances $d = 5.9$ and $3\,\mu\text{m}$ in Figs. 6.4d, e. These results agree well with the measurements of the relative-phase correlations. The superfluid-normal transition occurs at a lower value of $\mathcal{D}$ when d is smaller, with $\mathcal{D}_c = 5.4(6)$ from the common phase for $d = 1.7\,\mu\text{m}$. These observations are further supported by Monte Carlo simulations, showing consistent scaling in the superfluid and crossover regimes.

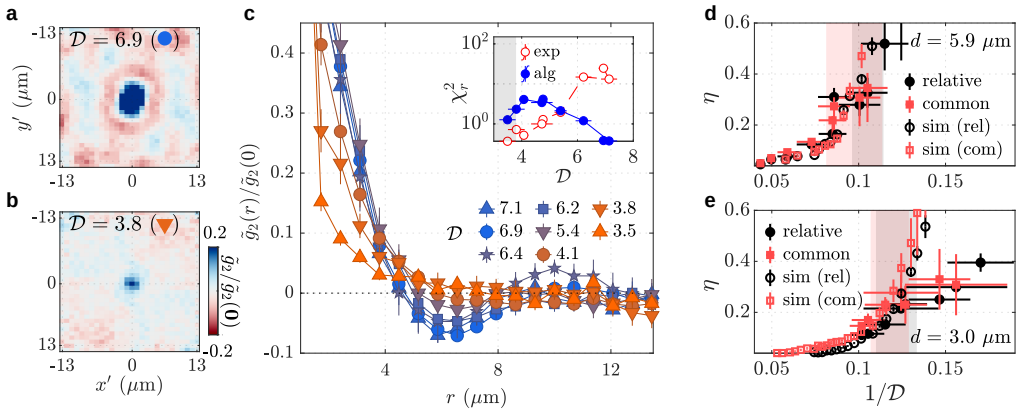


Figure 6.4: Phase coherence of the common mode. a,b. Noise-correlation functions $\tilde{g}_2(r)/\tilde{g}_2(0)$ are shown for $\mathcal{D} = 6.9$ and 3.8, with an inter-well distance $d = 1.7\,\mu$m. **c.** Radially averaged noise-correlation functions $\tilde{g}_2(r)$ are presented for values in the range from $\mathcal{D} = 3.5$ to 7.1, at $d = 1.7\,\mu$m, where the lines connecting the points are a guide to the eye. Inset shows the χ_r^2 values for the two fit models at different $\mathcal{D}$ values (see text). Fitting is performed for $r > 2\,\mu$m to exclude the effect of finite imaging resolution. **d,e.** Measurements of the algebraic exponent η for both the common and relative modes, along with simulation results, are shown for $d = 5.9\,\mu$m and $3\,\mu$m. The black (red) shaded region represents the critical points and their uncertainty in the relative (common) phase, obtained from experimental data, determined by the range over which the χ_r^2 values for the models cross.

6.4 Summary

Fig. 6.5 summarises the measurements of the critical points for the relative and common modes. Within experimental error, the value of $\mathcal{D}_c$ is not strongly affected by small interlayer coupling $J/h \ll 1\,$Hz. However, $\mathcal{D}_c$ decreases monotonically with increasing coupling when $J/h \gtrsim 1\,$Hz, providing evidence for the emergence of a double-layer superfluid (DLSF) phase. These measurements agree well with the predictions of RG theory for layered 2D systems [58]. To further validate the results, Dr Vijay Singh our theory collaborator performed Monte Carlo simulations of the coupled bilayer system using experimental parameters. From the simulations we determine $\mathcal{D}_c(J)$ by direct correlation analysis of the fluctuating classical fields. The simulation results for the antisymmetric mode agree closely with the respective measurements (Fig. 6.5). These simulations reveal that the critical points for the relative and common modes differ significantly for $d \lesssim 2\,\mu$m, indicating a strong phase-locking effect that results in an ordered relative phase while the common

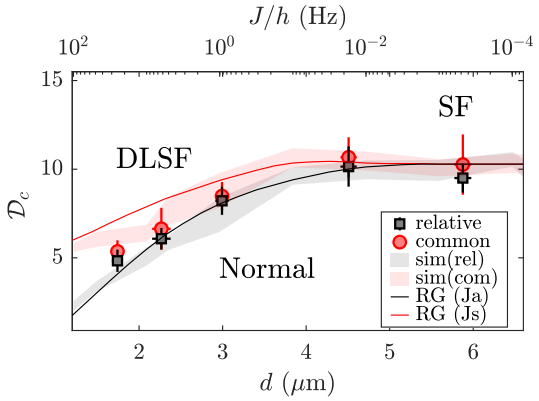


Figure 6.5: Phase diagram of the coupled bilayer 2D Bose gas. Measurements of the critical phase-space density D_c for both the relative (circles) and common (squares) modes are compared with the results from Monte Carlo simulations (filled curves). The solid lines are the predictions from the RG theory for two coupled 2D Bose gases. The coupling strength J (horizontal axis at the top) varies exponentially with the interlayer separation d shown on the bottom axis.

phase remains disordered, characteristic of a predicted anti-symmetric superfluid (ASF) phase [58]. In the range of coupling strengths that we have investigated experimentally, we have not observed the separation of the critical points for the relative and common degrees of freedom that is characteristic of a predicted ASF phase. However, in future work, it should be possible to investigate the interesting ASF phase, with stronger interlayer coupling by reducing the barrier height of the double-well potential (which was fixed in this work) while carefully maintaining 2D conditions for the two layers.

To elucidate the microscopic origin of the DLSF phase, we analyse quantised vortex excitations appearing as sudden phase jumps in the relative-phase interference patterns (Fig. 6.6a). These free vortices in the relative-phase mode are only visible when they are located within the narrow region of the imaging slice (Fig. 6.2d), allowing the quantitative analysis of their number density from interference images [6]. In Fig. 6.6b, the measurements of the dimensionless vortex density $n_v\xi^2$, as a function of $\mathcal{D}$, display exponential behaviours for all values of d. The healing length $\xi = 1/\sqrt{\tilde{g}n}$, determined by the 2D density n and interaction $\tilde{g}$, characterises the size of the vortex core. This exponential scaling is a hallmark of the BKT transition, consistent with previous measurements of 2D Bose gases with negligible

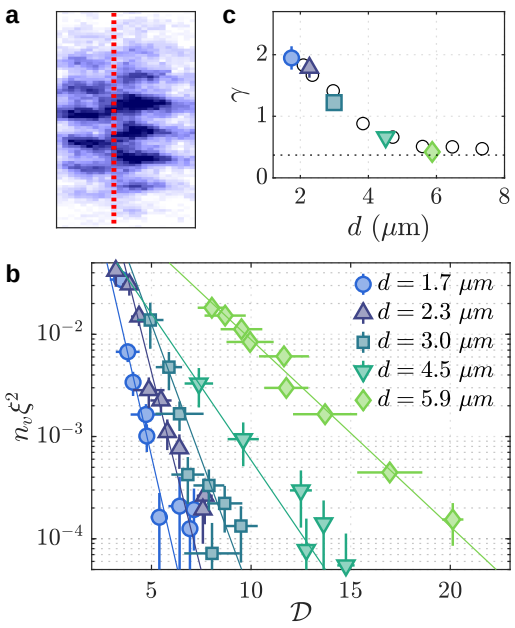


Figure 6.6: Vortex suppression in the relative mode of a bilayer. a. Phase jumps in the fringes, correspond to vortices in the relative phase (as indicated by the red dashed line); these emerge in the interference patterns as the system approaches the transition point. **b.** Dimensionless vortex density $n_v\xi^2$ plotted on a log scale as a function of the phase-space density $\mathcal{D}$ for various values of d. n_v is obtained by averaging over multiple experimental repetitions. The solid lines denote exponential fits to the function $f(\mathcal{D}) = A\exp(-\gamma\mathcal{D})$, where A and γ are fitting parameters. **c.** The best-fit values of the exponent γ are shown, with the horizontal dashed line marking the value for an uncoupled system ($d = 7\,\mu$m), as reported in Ref. [6]. The empty circles are the results obtained from Monte Carlo simulations.

interlayer coupling [6]. In our bilayer system, the interlayer coupling strongly suppresses inter-layer phase jumps, suppressing vortex formation in the relative phase field, although the scaling remains exponential. Notably, the scaling exponent increases as d decreases, indicating that stronger interlayer coupling enhances vortex suppression in the relative mode (Fig. 6.6c).

The realisation of bilayer 2D systems and the interferometric detection scheme demonstrated in this work provides a powerful new approach for exploring novel phases in coupled systems. For instance, this platform can be utilised to study the two-step BKT transition predicted in imbalanced bilayer systems [82, 83, 87]. Moreover, the ability to tune the coupling strength, provided by MRF-potentials, makes it possible to investigate the dynamics of phenomena that were previously inaccessible, such as the Kibble-Zurek mechanism [58, 100, 101], universal scaling

[93, 101, 102] in particular predictions for non-thermal fixed points in the sine-Gordon model [103, 104], parametric enhancement of superfluidity [10, 105], and phase-locking effect of the antisymmetric superfluid phase [58, 106].

Following this work En Chang led an experimental investigation where we used the DLSF phase to perform quenches from a phase with topological defects to one without [48]. This was done by rapidly changing the tunnel-coupling between the layers and was used to study universal dynamical scaling at the transition [35, 48].

6.5 Experimental Details

This section provides additional information on how the results reported in this chapter were obtained experimentally, such as how the experimental data were analysed and compared to numerical simulations.

6.5.1 Experimentally realising ultracold bilayers

To realise the bilayers we form the double-well potential for the dressed atoms using a combination of a static and radiofrequency (RF) magnetic fields as described in Ch. 2. The static field is a quadrupole magnetic field with cylindrical symmetry about a vertical axis, and three RF fields are applied to give a multiple-RF (MRF) double-well trap [14, 107]. Control over the amplitudes and frequencies of RF components allows us to shape the potential from a single well into a double-well potential, as described in Ch. 2 and in Refs. [14, 107–109]. In this work, we used the combinations of RFs in Table 6.1 to control the separation between the layers.

For each set of RF frequencies, we find combinations of RF amplitudes that provide tight confinement in the vertical direction ($\omega_z/2\pi = 1.2$ kHz) for each well and produce a 2D potential, with the double-well barrier height of $E_b/h \sim 4$ kHz. This large barrier height $k_B T, \mu \ll E_b$ ensures that the atoms in each plane are kinematically constrained to their respective 2D planes, with finite

Separation	RF_1	RF_2	RF_3
5.9 µm	7.08 MHz	7.2 MHz	7.32 MHz
4.5 µm	7.11 MHz	7.2 MHz	7.29 MHz
3.0 µm	7.14 MHz	7.2 MHz	7.26 MHz
2.3 µm	7.15 MHz	7.2 MHz	7.25 MHz
1.7 µm	7.155 MHz	7.2 MHz	7.245 MHz

Table 6.1: RF frequencies used to realise the different separations between the wells in the MRF dressed double well potential.

probability of hopping between the layers facilitated by the overlap of ground-state wavepackets along the z direction, analogous to double-well experiments with 1D Bose gases [71, 110, 111].

After loading the atoms into a single-RF dressed potential and performing evaporative cooling, we transfer the atoms into the MRF-dressed potential adiabatically, by slowly increasing the amplitudes of the other two RF signals. This can be performed with negligible heating in the system, and we further ramp up the optical potential over 3 seconds to realise a near-uniform density of atoms in the $x-y$ plane. An optical potential is created by 532 nm laser light, shaped by a spatial light modulator (digital micromirror device, DMD), to realise a box-like trap geometry (see Fig. 6.2a). We ensure the populations in the two wells are equal by maximising the observed matter-wave interference contrast as described in Ref. [60]. After equilibrating the gases further for 500 ms, the MRF-dressed potential and the optical potential are turned off, releasing the cloud into TOF expansion to observe the matter-wave interference pattern as shown in Fig. 6.2 [6].

Finally, to probe the density distribution locally, before absorption imaging we apply a sheet of repumping light that propagates horizontally (in the x direction) with thickness $L_y = 5$ µm and height much larger than the extent of the cloud of atoms [60]. All atoms are initially in a state with $F = 1$, and are then selectively pumped to $F = 2$ by the sheet of repumping light, which we image using a light resonant for the atoms in the $F = 2$ state (Fig. 6.2c,d). We ensure the repumping light passes through the centre of the cloud by moving the pattern along the direction parallel to the propagation of imaging light, to the position

where the total absorption signal is maximum. We repeat the experiments using repumping light sheet with size covering the entire cloud, to extract the total atom number reported in the main text.

6.5.2 Image analysis for relative-phase detection

The analysis of the interference patterns is described in detail in Refs. [6, 18, 93] and proceeds as follows. We first characterise the wavevector of the fringes by fitting the interference pattern with the function also used in Ch. 3

$$\rho_x(z) = \rho_0 \exp\left(-z^2/2\sigma^2\right)\left[1 + c_0 \cos(kz + \theta(x))\right], \tag{6.7}$$

where $\rho_0, \sigma, c_0, k, \theta(x)$ are fit parameters, as shown in Fig. 6.7. We then obtain the relative phase profile $\theta(x)$ by Fourier transforming the images along the z direction at each x and extracting the complex argument of the Fourier coefficient corresponding to the wavevector of the fringes. The extracted phase $\theta(x)$ encodes a specific realisation of the fluctuations of the in-situ local relative phase between the pair of 2D gases. From the ensemble of at least 40 images at each d and N, we calculate the phase correlation function $C(\overline{x}) = \mathrm{Re}[\langle e^{i[\theta(x)-\theta(x-\overline{x})]}\rangle_x]$ where the averaging is performed over the set of images and different positions in the cloud x for which x and $x - \overline{x}$ are within the central 30 µm of the density distribution of the cloud. As described and confirmed experimentally in Ref. [6], the long-range behaviour of this function changes from algebraic scaling $\sim r^{-\eta}$ in the superfluid phase, to exponential scaling in the normal phase. We thus fit the obtained $C(\overline{x})$ at long distance $r \gtrsim 5$ µm where the effect of finite imaging resolution is negligible. From the fits with both algebraic and exponential models, we compare the χ_r^2 statistics to identify the critical point $\mathcal{D}_c$ (see Fig. 6.3). The uncertainty of $\mathcal{D}_c$ is determined by the averaged difference of $\mathcal{D}$ to the two nearest data points.

From the interference images, taken along y direction, we detect vortices using the method described in detail in Ref. [6]. We look for sudden jumps of the phases within two pixel distance (3.4 µm), defined by the phase difference of $2\pi/3 < \delta\theta < 4\pi/3$. The vortex density $n_v(x)$ can be obtained by dividing the probability of finding

vortices in each column of the images by the vortex detection area of a single pixel column, $\ell_p L_y = 8.4\,\mu\text{m}^2$ where $\ell_p = 1.67\,\mu\text{m}$ is the image-plane pixel size.

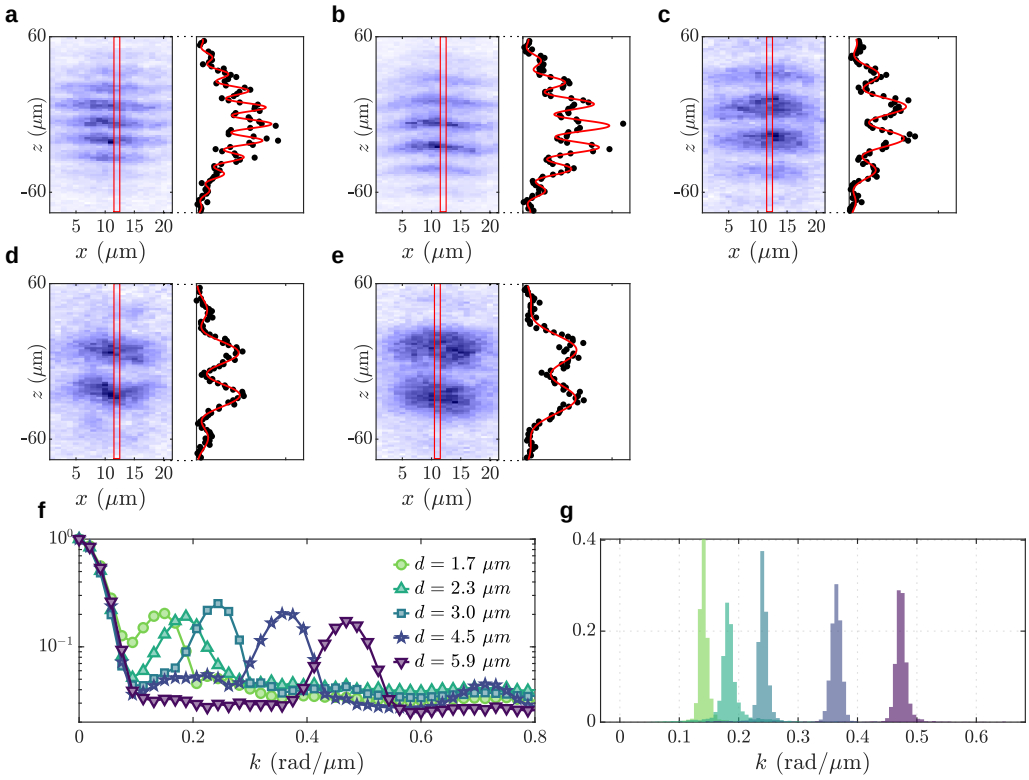


Figure 6.7: Matter-wave interference patterns and their spectra. a-e, Matter-wave interference images at: **a** $d = 5.9\mu m$, **b**, $d = 4.5\mu m$, **c**, $d = 3.0\mu m$, **d**, $d = 2.3\mu m$, **e**, $d = 1.7\mu m$. The panels on the right show the density distribution along the central column, in arbitrary units, together with a fit with model (Eq. 6.7). **f.** Normalised spectra along the z directions, of the experimental images, plotted for different well separations d. The low-momentum peak comes from the envelope of the 2D cloud following the TOF expansion, and their nearly complete overlap demonstrates the same vertical trapping parameter; the expansion along z is that of a Gaussian ground-state wavepacket for quasi-2D regime [112]. **g.** Distributions of fitted values of the interference fringe wavelengths. The peak locations are unchanged from panel **f**, while the peak is narrowed by a non-linear least squares fitting routine.

6.5.3 Image analysis for common-phase detection

As analytically studied and experimentally confirmed for bilayer 2D Bose gases in Ch. 5 (and independently in Ref. [56] for double-well 1D Bose gases), the spatial coherence of the common phase $\varphi = \phi_1 + \phi_2$ predominantly affects the density-noise pattern observed along the double-well direction (Fig. 6.2d). The noise-correlation function in 2D Bose gases, obtained by taking the two-point density-density correlation function after a short TOF, is expressed by the common-mode and relative-mode correlation functions $\mathcal{F}_{\mathrm{com}}(\boldsymbol{r})^2 \simeq \langle \Psi_1^\dagger(\boldsymbol{r})\Psi_2^\dagger(\boldsymbol{r})\Psi_1(\boldsymbol{0})\Psi_2(\boldsymbol{0})\rangle/n^2$ and $\mathcal{F}_{\mathrm{rel}}(\boldsymbol{r})^2 \simeq \langle \Psi_1^\dagger(\boldsymbol{r})\Psi_2(\boldsymbol{r})\Psi_2^\dagger(\boldsymbol{0})\Psi_1(\boldsymbol{0})\rangle/n^2$ via [47]

$$\begin{aligned} g_2(\boldsymbol{r},t) \;&\approx \frac{1}{(2\pi)^2}\int d^2\boldsymbol{q}\int d^2\boldsymbol{R}\cos(\boldsymbol{q}\cdot\boldsymbol{r})\cos(\boldsymbol{q}\cdot\boldsymbol{R}) \\ &\times \frac{\mathcal{F}_{\mathrm{com}}(\boldsymbol{q}_t)^2\mathcal{F}_{\mathrm{com}}(\boldsymbol{R})^2}{\mathcal{F}_{\mathrm{com}}(\boldsymbol{R}-\boldsymbol{q}_t)\mathcal{F}_{\mathrm{com}}(\boldsymbol{R}+\boldsymbol{q}_t)}\mathcal{F}_{\mathrm{rel}}(\boldsymbol{q}_t)^2, \end{aligned} \tag{6.8}$$

where $\boldsymbol{q}_t = \hbar\boldsymbol{q}t/m$ and t is the time-of-flight duration. The common-mode fluctuations are primarily responsible for the spatial structure of the self-interference patterns and thus the oscillatory behaviour of g_2, while relative-mode correlations are only relevant in the normal phase, where g_2 displays short-ranged exponential decay (Fig. 6.4c).

The analysis of the density-noise patterns, as shown in Fig. 6.4, proceeds as follows, as described in Ch. 5. From at least 20 experimental images taken from below as in Fig. 6.2d for each experimental parameter value, we first normalise the images by the average density distribution for each dataset. We then obtain autocorrelations from the density patterns in the images within a region of interest (ROI) capturing the central part of the cloud. This results in a collection of correlation functions on a 2D grid, scaled by the squared mean density $n_0^2 = \langle\hat{n}(\boldsymbol{r},t)\rangle^2 = \langle\hat{\Psi}(\boldsymbol{r},t)^\dagger\hat{\Psi}(\boldsymbol{r},t)\rangle^2$, where $\hat{\Psi}(\boldsymbol{r},t)$ is the bosonic field operator after the expansion corresponding to [53]

$$\frac{\langle\hat{n}(\boldsymbol{r},t)\hat{n}(\boldsymbol{0},t)\rangle}{n_0^2} = g_2(\boldsymbol{r},t) + \frac{\delta(\boldsymbol{r})}{n_0}, \tag{6.9}$$

where the second term is the shot-noise term with zero mean, such that

$$g_2(\boldsymbol{r},t) = \frac{\langle\hat{\Psi}^\dagger(\boldsymbol{r},t)\hat{\Psi}(\boldsymbol{r},t)\hat{\Psi}^\dagger(\boldsymbol{0},t)\hat{\Psi}(\boldsymbol{0},t)\rangle}{\langle\hat{n}(\boldsymbol{r},t)\rangle\langle\hat{n}(\boldsymbol{0},t)\rangle}, \tag{6.10}$$

is identified by averaging over experimental repetitions. Some of the extracted g_2, such as Fig. 6.4a, exhibit anisotropy of the ring structure which arises because of finite sampling used in our measurements but this does not affect the radially averaged g_2 functions used for the quantitative analysis such as the fitting procedure described in this section. We have confirmed this by taking a larger dataset for a few chosen parameters and then randomly selecting a subset, some of which contain anisotropic rings, and finding that this resampling analysis yields the same radially averaged g_2 functions.

The quantitative analysis of the measured g_2 follows the procedure that I developed, outlined in Ch. 5 and Ref. [47]; we fit the experimental data with a model based on Eq. (6.8), where the model is constructed from the theoretical forms that describe both $\mathcal{F}_{\rm com}$ and $\mathcal{F}_{\rm rel}$, namely, the algebraic falloff in the superfluid regime and the exponential decay in the normal regime, for both common and relative phase modes [53, 58]. More concretely, Dr Vijay Singh a theory collaborator at TII Abu Dhabi, programmed a numerical routine to compute Eq. (6.8) and performed curve fitting via nonlinear least squares; fit results of a few representative datasets are shown in Fig. 6.8.

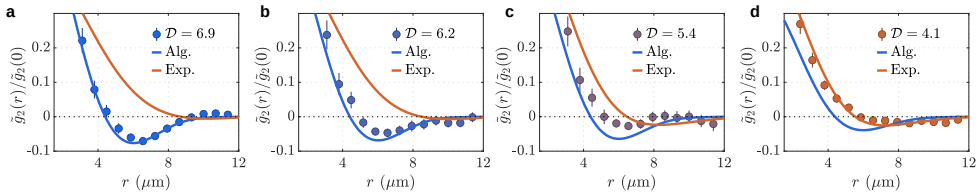


Figure 6.8: Density noise-correlation functions across the critical point. Radially averaged noise-correlation functions $\tilde{g}_2(r)$ for the $d = 1.7\,\mu$m dataset also shown in Fig. 6.4c. The best fits from Eq. 6.8, corresponding to algebraically (exponentially) decaying form of the common phase correlations are shown in blue (orange), where the shapes depend on the value of the algebraic (exponential) decay parameters. Data shown for phase-space densities are **a**, $\mathcal{D} = 6.9$, **b**, $\mathcal{D} = 6.2$, **c**, $\mathcal{D} = 5.4$, **d**, and $\mathcal{D} = 4.1$.

6.5.4 Estimation of Josephson coupling J

We estimate the interlayer coupling strength J by numerically solving for the ground and first excited states in our trap using the imaginary time evolution of 3D Gross-Pitaevskii equation [113]. This allows us to numerically compute the position representation of the lowest eigenstates of the 2D Bose gas in the MRF potentials we realise in the experiment. We deduce the Josephson plasma energy in the two-mode model following the method of the improved two-mode model in Ref. [114]. The improved two-mode model provides a way to numerically compute the strength of the Josephson tunnelling J from the spatial overlap and energies of the lowest energy eigenstates. For our system the relation between well separation and Josephson coupling energy follows

$$J/h = F_0 e^{(-b\cdot d)}, \tag{6.11}$$

where $F_0 = 2437$ Hz, $b = 2.63 \times 10^6\,\mathrm{m}^{-1}$ and d is the well separation. The well separation is calculated from the fringe spacing in the interference patterns as seen in Fig. 6.7.

6.5.5 Monte Carlo simulation of tunnel-coupled bilayers

For 2D bilayers our theory collaborator Dr Vijay Singh used classical Monte Carlo simulations, as introduced in Sec. 4.2.1 to study the many-body thermal state of our interacting system at nonzero temperature. To perform these simulations we discretise real space on a 2D square lattice and represent the continuous Hamiltonian using the discrete Bose-Hubbard Hamiltonian. The system of two 2D layers (labelled $a = 1, 2$) coupled by a tunable Josephson tunnelling J is described by the Hamiltonian

$$H = H_1 + H_2 + H_{12}, \tag{6.12}$$

with, for each layer,

$$\begin{aligned} H_a = &-J_h \sum_{\langle ij \rangle} \left(\psi^*_{a,i}\psi_{a,j} + \psi^*_{a,j}\psi_{a,i} \right) + \frac{U}{2} \sum_i n^2_{a,i} \\ &+ \sum_i (V_i - \mu) n_{a,i} \end{aligned} \tag{6.13}$$

and the interlayer coupling described by

$$H_{12} = -J \sum_i \left(\psi_{1,i}^* \psi_{2,i} + \psi_{2,i}^* \psi_{1,i} \right). \tag{6.14}$$

Here, $\langle ij \rangle$ denotes nearest neighbours, $\psi_{a,i}$ and $n_{a,i} = |\psi_{a,i}|^2$ are the complex-valued field and the density at site i, respectively. V_i corresponds to the trapping potential at site i, J_h is the hopping energy, and U is the onsite repulsive interaction energy. We choose the simulation parameters according to the experiments. The total atom number N, which varies between 20 000 and 90 000, is adjusted by the chemical potential μ in the simulations. We consider a lattice system with sites $N_x \times N_y = 100 \times 100$ and use a discretisation length of $l = 0.5\,\mu\text{m}$. For the continuum limit, l is chosen to be smaller than or comparable to the healing length and the de Broglie wavelength [115]. The value of U is determined by $U/J_h = \sqrt{32\pi} a_s / l_0 = 0.16$, based on the experimental scattering length a_s and the harmonic oscillator length $l_0 = \sqrt{\hbar/(m\omega_z)}$ of the confining potential $m\omega_z^2 z^2/2$ in the transverse direction, where m is the atomic mass. J_h is given by $J_h = \hbar^2/(2ml^2)$, yielding $J_h/k_\text{B} = 11.16\,\text{nK}$ for ^{87}Rb atoms and $l = 0.5\,\mu\text{m}$. V_i is chosen such that the simulated cloud produces a homogeneous density profile with a radius of 20 µm.

In the classical-field approximation, one replaces the operators $\hat{\psi}$ by complex numbers ψ as in Eq. 6.12. The initial states are generated using a grand-canonical ensemble of temperature T and chemical potential μ, via a classical Metropolis algorithm [116, 117]. We set $T/J_h = 4.5$ and vary μ to achieve the desired N for various values of J within the range between $10^{-4}\,\text{Hz}$ and $100\,\text{Hz}$. The simulation procedure involves randomly selecting lattice sites and performing single-site updates by modifying the real and imaginary parts of the complex field, drawn from a normal distribution. The width of the distribution is adjusted such that the acceptance rate is around one half for each step. About 10^5 steps are performed to thermalise the system. After thermalisation, more than 2000 updates per site are executed to ensure that the generated states are uncorrelated. For each sample, we calculate the phases $\theta_1(x, y)$ and $\theta_2(x, y)$ of the two clouds, and use them to compute the correlation functions (Fig. 6.9). We average the two-point correlation

function over the initial ensemble and determine the superfluid-normal transition point for various values of J.

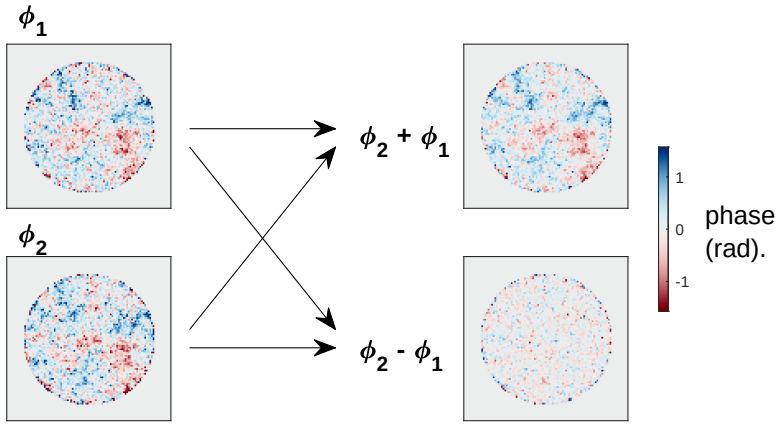


Figure 6.9: Analysis of numerical simulation. From the simulated phase fields ϕ_1 and ϕ_2, we obtain the symmetric and antisymmetric modes from which the phase correlation functions are computed.

7

Implementing a Speckle Disorder Potential

This chapter covers experimental work undertaken to add the ability to apply a disordered potential to the 2D Bose gas samples in the previous generation experiment. The implementation of a disordered optical potential to the experimental apparatus opens up new avenues of research, starting with experimentally mapping out a phase diagram of how disorder and temperature affect 2D Bose gases, reported in Ch. 8. Such a phase diagram provides a foundation for further investigations into how disorder affects the system, for example investigating the dynamical scaling when a disorder-driven BKT transition is crossed. This chapter describes the experimental implementation and characterisation of the disordered potential added to the experiment.

7.1 Implementing a Repeatable Speckle Potential

We wished to investigate the effect of a speckle potential, a type of disordered potential which has previously been studied both theoretically and experimentally in the context of disordered 2D Bose gases [118–122]. In this work we consider a speckle with a Gaussian-distributed autocorrelation,

$$\langle V_d(\boldsymbol{r}) V_d(\boldsymbol{r'}) \rangle = V_d^2 e^{-\frac{|\boldsymbol{r}-\boldsymbol{r'}|^2}{2\ell_d^2}} \tag{7.1}$$

where ℓ_d is the correlation length of the speckle potential. We generate speckle patterns by passing a blue detuned (repulsive) laser beam with a Gaussian profile through a diffusive plate [123]. Diffusive plates are optical elements which randomly perturb the phase of the incoming light at different positions which gives rise to an optical speckle pattern in the far field. The use of a disordered potential with distinct but repeatable disorder realisations, implemented using a rotating diffusive plate, is a key feature of this work compared to previous works studying the effect of disordered potentials on 2D Bose gases [118]. Distinct but repeatable disordered potentials drawn from a statistical ensemble are needed in our case since the typical size of our BEC $\sim$20 μm is not several orders of magnitude greater than the $\sim$2 μm correlation length of the disorder. Because of this the Bose gas in our experiment is not in the so-called self-averaging regime [124], where the statistics of the disorder at different spatial locations in the system match the statistics of different disorder realisations. However we can circumvent this by using different realisations of the disorder so the system experiences an ensemble of disorder realisations with the correct statistics. Whereas in a system large enough so that it is in the self-averaging regime, a single realisation of the disorder would be sufficient to capture the statistical variations of the disordered potential.

7.1.1 Speckle patterns

Speckle patterns, as described in the book by J W Goodman [125], can be generated by applying random perturbations to the phasors of the Fourier amplitudes of a light-field. Considering a field with N discrete Fourier components, this gives Fourier amplitudes

$$\boldsymbol{A} = \frac{1}{\sqrt{N}} \sum_{n=1}^{N} a_n e^{i\varphi_n} \tag{7.2}$$

where the statistics of φ_n and a_n determine the properties of the speckle pattern. We consider φ_n being uniformly distributed on the interval $(-\pi, \pi)$, which is motivated by symmetry. Considering the real and imaginary parts of $\boldsymbol{A}$ one can see that they have zero mean, with second moments given by

$$\sigma^2 = \frac{1}{N}\sum_{n=1}^{N} E[a_n^2]E[\cos(\varphi_n)^2] = \frac{1}{N}\sum_{n=1}^{N} E[a_n^2]E[\sin(\varphi_n)^2] = \frac{1}{N}\sum_{n=1}^{N}\frac{E[a_n^2]}{2} \tag{7.3}$$

where the total variance follows from the real and imaginary parts being independent and Gaussian distributed from the central limit theorem. We get that the magnitude of the phasors are Rayleigh distributed

$$p(|A|) = \frac{|A|}{\sigma^2} e^{-\frac{|A|^2}{2\sigma^2}}. \tag{7.4}$$

It thus follows that the mean and variance are

$$\begin{aligned} \mu_A &\approx 1.25\sigma \\ \sigma_A^2 &\approx 0.43\sigma^2. \end{aligned} \tag{7.5}$$

Let us now consider the probability distribution of the intensity, since this is both the relevant quantity we can measure with a CMOS camera and what the atoms experience of the light field. Considering $I = |A|^2$ we see that

$$P(I) = P_A(A)\left|\frac{dA}{dI}\right| = \frac{1}{|A|}P_A(A) = \frac{1}{2\sigma^2}e^{-\frac{I}{2\sigma^2}} = \frac{1}{\mu_I}e^{-\frac{I}{\mu_I}}. \tag{7.6}$$

Thus we expect the probability distribution for the intensity in a speckle pattern to decay exponentially. We must then incorporate the initial Fourier amplitudes to obtain a correct speckle pattern. Considering a Gaussian beam in terms of wave vectors

$$E_0(k_x, k_y) = e^{-\frac{k_x^2+k_y^2}{2k_T^2}} \tag{7.7}$$

where $k_T^2 = k_0/z_R$, z_R is the Rayleigh range, and $k_0 = 2\pi/\lambda$. Using $z_R = \pi w_0^2/\lambda$, where w_0 is the beam waist. Considering the focus of the beam after the 37.6 mm objective lens and the beam having an initial waist diameter of 2.7 mm, measured using a CMOS camera, we get a diffraction limited spot size of

$$w_f = \frac{\lambda f}{\pi w_o} = 4.36\,\mu\text{m}. \tag{7.8}$$

7.1.2 Stick-slip servo

To hold the holographic diffuser in a controllable and repeatable orientation, so an off-axis beam illuminates a repeatable location, we use a stick-slip rotation mount (*Thorlabs, ELL14*). Stick-slip servos utilise a piezo and a rod-like piece whose end traces out an ellipse when it is driven at resonance by the piezo. By tracing out an ellipse the rod can drag an object along (by sticking to it and then slipping) in very fine increments. This rotation mount features orientation with 1.75 mrad accuracy and has a digital magnetic encoder with a resolution of 143, 360 distinct values over 360 degrees, giving an angular resolution of 43 μrad. This rotation mount is shown in Fig. 7.1. To control this rotation mount I wrote a Python package to provide a high-level programming interface and functions for serial communication with the device. The functionality of this Python package was then exposed with an RPC server written using Sipyco and integrated with the Artiq control system [18]. This way distinct and repeatable disorder realisations could be specified. This allows us to sample different disordered potentials with the same statistics so that any findings are not tied to a specific realisation of the disorder we project upon the atoms, as any single realisation might not be representative of the ensemble. The

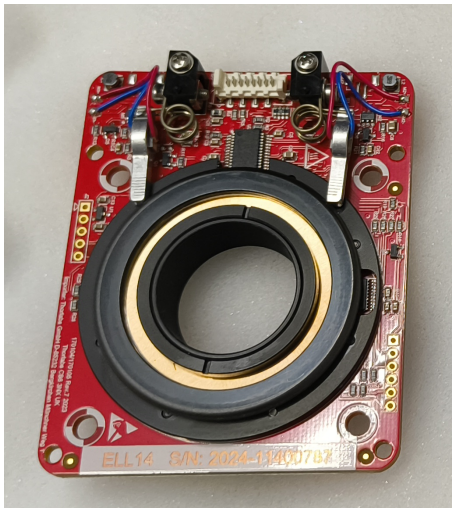


Figure 7.1: The rotation mount used to allow for distinct and repeatable disorder realisations when a Gaussian beam is propagated, displaced from the central axis, through a holographic diffuser mounted in the pictured mount. The angular resolution of the stick-slip mechanism in conjunction with the magnetic encoder is discussed in the text.

in-situ density distribution for distinct disorder realisations at high power (2 times the highest shown in the calibration, 1.0 linearised amplitude, 2W), to accentuate the effect of the speckle potential in-situ. Examples of in-situ density distributions when the speckle potential is applied are shown in Fig. 7.2. We note that the different disorder instances were queued in random order, so the different repeats of the same instance of the disorder pattern in Fig. 7.2 were in general not captured in succession. The addition of the stick-slip rotation mount for repeatable and distinct

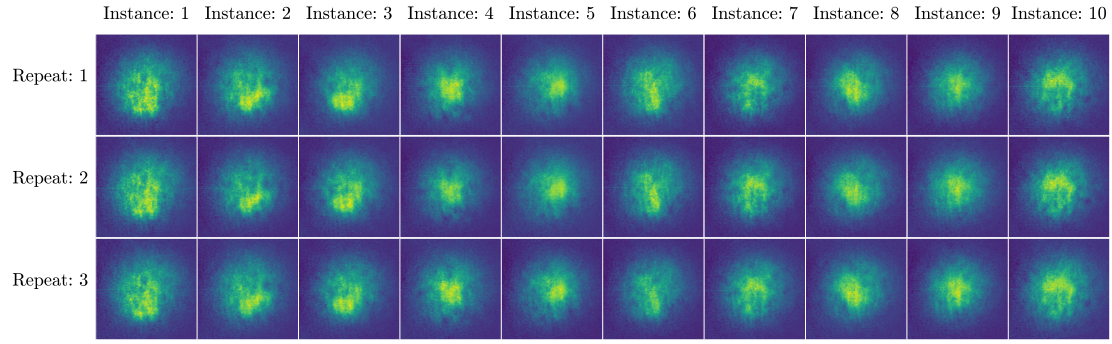


Figure 7.2: In-situ density distribution with 10 different instances of the speckle pattern disorder applied by using different rotation angles on the stick-slip mount. Each pattern was applied 3 non-successive times, as ordered vertically. The box potential was not applied when these images were taken

disorder realisation was a significant upgrade of the capabilities of our experiment, and opens the way for further investigations of disorder in condensed matter systems. The ability to see the effect of different well-characterised disorder realisations is something which cold atoms based experiments enable, but which is generally not feasible in solid-state condensed matter systems with random impurities. This therefore opens the possibility of studying how specific properties of a disordered potential, such as the spatial correlations or fractal dimension of the disorder, affect a system's properties. Repeatable disorder realisations will also allow us to study how collective properties and microscopic details, such as vortex pinning, depend on the specifics of a spatially disordered potential.

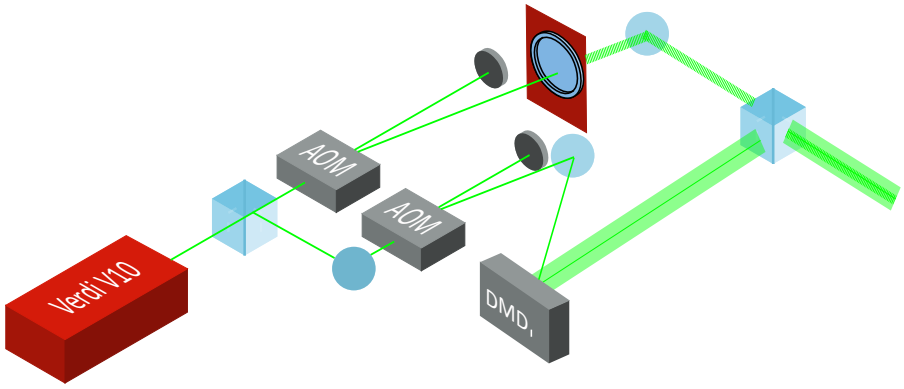


Figure 7.3: Schematic showing how AOMs are used to modulate the intensity of the light used to create the hard wall from the DMD and the light which passes through the diffusive plate to create the speckle potential.

7.1.3 Optical setup for green light

The blue detuned 532 nm beam used to illuminate the atoms with the speckle pattern was initially aligned on the atoms without the diffusive plate in the beam path. The beam was aligned by ensuring it was co-propagating with the imaging beam used for vertical imaging which was known to be well aligned on the atoms, and then comparing with the light from the DMD used for repulsive walls which was also aligned on the atoms. As the condensed cloud is $\sim$50 μm wide and the experiment has a cycle time over a minute blindly walking the beam would not be fruitful and aligning the disorder beam based on known references was necessary. When the disorder beam was aligned to be co-propagating with the previously aligned beams the disorder beam punched a hole through the cloud which was clearly visible when imaging the in-situ density. When the diffusive plate was inserted only minor adjustments to the alignment were needed and these could be accomplished by looking at the effect of the disorder on the atoms.

7.1.4 Characterising the optical speckle potential

To characterise the properties of the disorder potential produced by the 0.5 degree holographic diffuser *(Edmund Optics SN: 47-988)* we illuminated it with green light from a diode-pumped solid state (DPSS) laser *(Coherent: Verdi V10)* and placed a CMOS camera in the path of the beam to image the resulting pattern. We

analysed the intensity distribution generated by the holographic diffuser to verify its statistical properties and found the exponentially decaying intensity distribution shown in Fig. 7.4. We studied the spatial correlations within the speckle patterns to

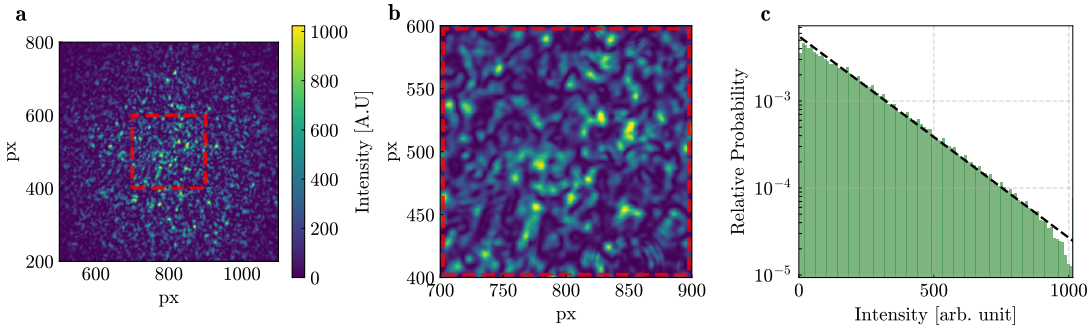


Figure 7.4: **a.** Image of speckle pattern generated with diffusive plate, red dashed line indicates region in which the intensity distribution was analysed. **b.** Central region analysed to obtain a histogram of the intensities, **c.** Histogram of intensities in the central region, the black dashed line corresponds to exponential decay and is included as a guide and is proportional to e^{-I}.

verify that they were Gaussian as expected. To do this we utilised an objective with the same specifications as the one used to illuminate the atoms in the experiment, this is since the correlation length of the speckle pattern depends on the diffraction limited spot size of the disorder beam. We measure a correlation length consistent with the diffraction limited spot size calculated earlier. The wide approximately Gaussian envelope which appears in the cross-correlation matrix in Fig. 7.5 is due to the Gaussian beam which illuminates the holographic diffuser. Furthermore,

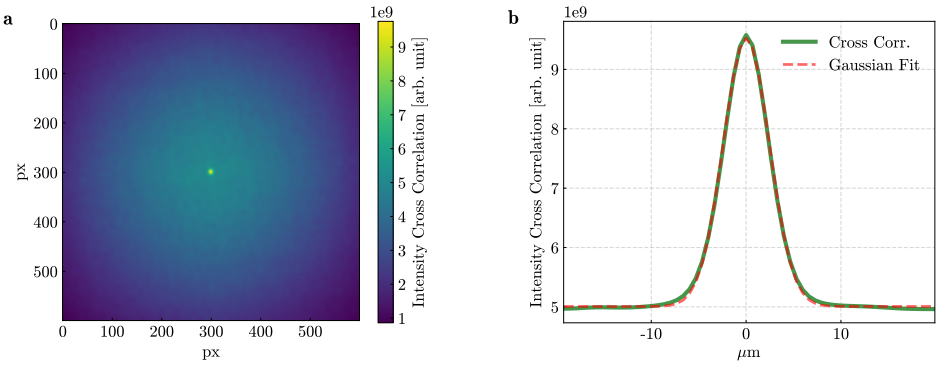


Figure 7.5: **a.** Two-dimensional cross-correlation matrix computed from the speckle pattern shown in Fig. 7.4a. **b.** The central 60 pixels fitted with a Gaussian distribution matching Eq. 7.1, the fitted Gaussian has $\ell_d = 2.44\,\mu$m.

we confirmed that different disorder realisations, obtained by rotating the stick-slip mount holding the waveplate in 8 different orientations separated by 40°, showed similar statistics as shown in Fig. 7.6 obtained by inspecting the speckle pattern with a CMOS camera.

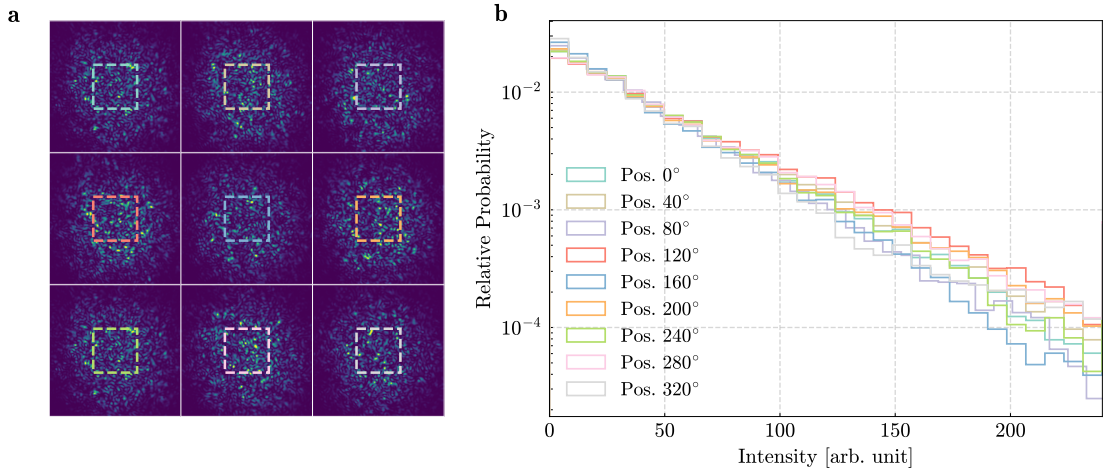


Figure 7.6: **a.** The regions of the 9 distinct speckle realisations analysed are outlined with dashed lines. **b.** Histogram of intensities in the central regions of the different speckle realisations.

7.1.5 Characterising the disorder strength

As seen in Fig. 7.3, we modulate the intensity of the disordered speckle potential by varying the amount of power in the first diffraction order of the AOM. To convert between the power in the first diffraction order into the strength of the potential felt by the atoms, quantified by V_d in Eq. 7.1, we need to establish the relation between the amplitude of the RF signal driving the AOM and the power in the first diffraction order. These measurements are shown in Fig. 7.7, with a piecewise linear interpolation between the measured points.

In what follows we work in terms of the linearised disorder amplitude, which is proportional to the intensity of the light sent through the diffusive plate, and therefore the parametrisation of the power in the disorder beam, which is the relevant quantity for the strength of the potential experienced by the trapped gas. To calculate the strength of the disorder potential we follow a procedure inspired by

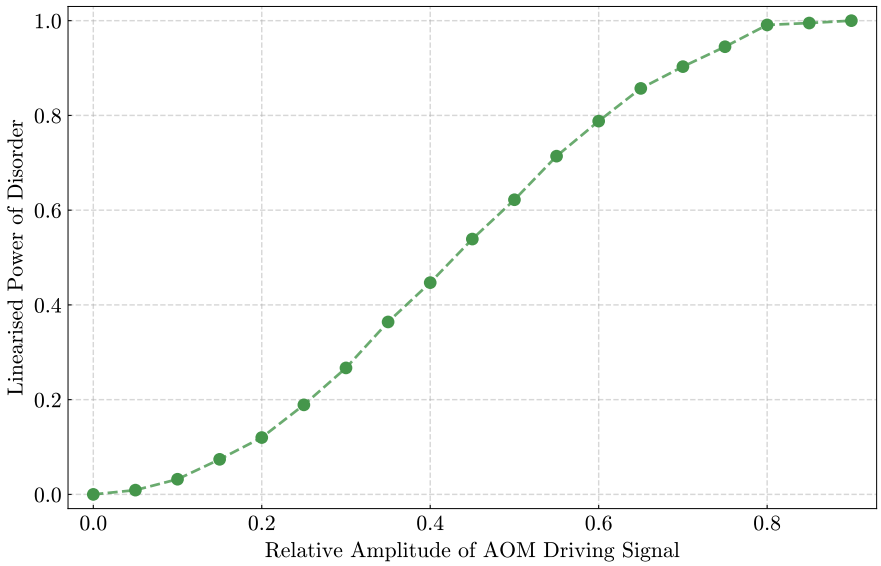


Figure 7.7: Relation between the amplitude of the AOM driving frequency and the power in the beam going to the diffusive plate to generate the disorder potential. Where both have been normalised to the $0-1$ range. The measured points are shown as dots and the piecewise linear interpolation is shown as a dashed line.

the one used by Beeler et al. [126], where a thermal cloud is released and after 0.5 ms the disorder potential is turned on for a short period (1 ms). By this procedure the gradients of the speckle potential impart momentum onto the atoms, this increase in momentum can be detected after TOF expansion. To establish the relation between disorder power and increased momentum (which we extract by fitting the width of the cloud after TOF in the same way as the temperature) we utilise a classical simulation code for a thermal Bose gas. With this code we simulate a large number of classical particles at thermal equilibrium which are perturbed by the addition of a speckle disorder potential for 1 ms. The speckle potentials are generated using the characterisation above to match the statistics of those generated by the diffusive plate where the phase is randomly perturbed. For this we use a method from earlier theoretical work [127] using the formula

$$V_{speckle}(\boldsymbol{r}_{i,j}) = A\left|\mathrm{DFT}_{2D}(e^{-i\varphi_{k_i,k_j}}e^{|\boldsymbol{k}_{i,j}|^2/\sigma^2})\right|^2 \tag{7.9}$$

where the prefactor A sets the amplitude, and $\varphi_{i,j}$ is uniformly randomly distributed. The width of the Gaussian inside the discrete Fourier transform (DFT) was chosen

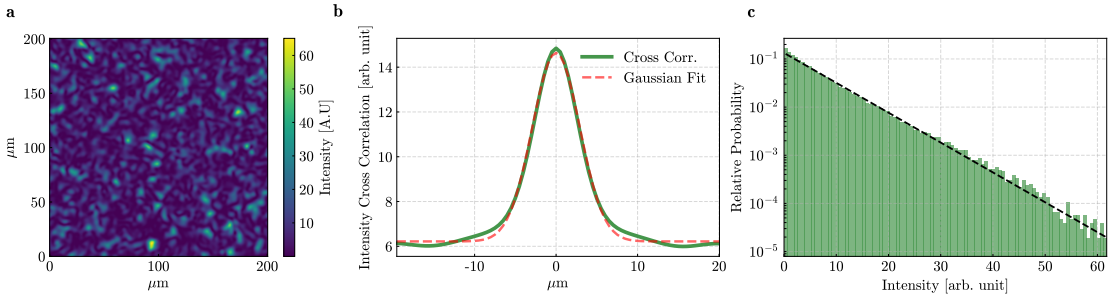


Figure 7.8: **a.** Example of speckle pattern generated using Eq. 7.9. **b.** Cross-correlation matrix computed from the simulated speckle pattern shown in panel a, fitted with a Gaussian distribution matching Eq. 7.1 the fitted Gaussian has $\ell_d = 2.5\,\mu$m. **c.** Histogram of intensities in the simulated speckle pattern the black dashed line corresponds to exponential decay and is included as a guide to the eye.

to match the expected diffraction limited spot size and also reproduces a speckle pattern with a correlation length in agreement with experimentally realised potential shown in Fig. 7.5. The simulated speckle pattern and the autocorrelation is shown in Fig. 7.8.

The classical particles in the simulation are confined in a harmonic potential matching the experiment and the initial positions and velocities of the particles are generated using Monte Carlo sampling to also match the temperature in the experiment. The atoms in the simulation are released from the trap and allowed to expand freely for 1 ms after which the potential is modified by the addition of the speckle pattern for 1 ms which is then turned off again and the atoms evolve freely again for another 8 ms. After this time evolution the estimated temperature was extracted from the mean kinetic energy of the atoms. The difference between the initial kinetic energy and the kinetic energy after the speckle pattern has been turned on was then expressed as a temperature and the effect of the strength of the speckle pattern on this quantity was inferred. For each strength of the speckle pattern 50 different speckle realisations were simulated and averaged over. The result of the disorder strength simulation shown in Fig. 7.9 corresponds to an initial temperature of the thermal cloud of 220 nK. To establish the effect of the initial temperature on our disorder strength calibration we performed the previous analysis for a range of initial temperatures and the results are shown in Fig. 7.10 below.

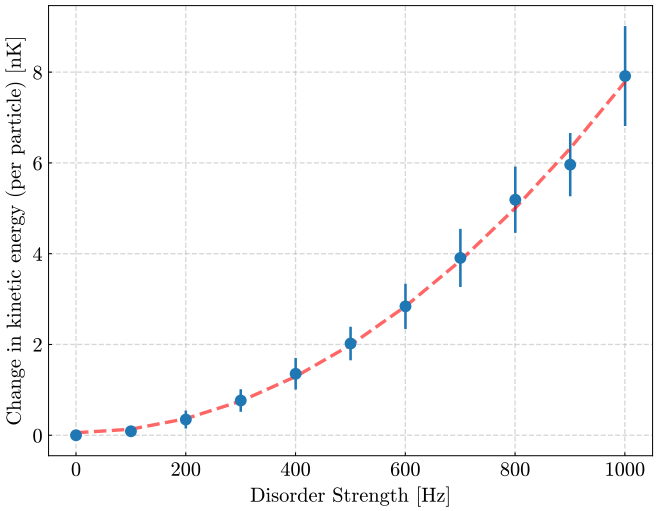


Figure 7.9: Simulation results for the change in kinetic energy imparted when pulsing a speckle potential on as described in the text, for various strengths of the speckle potential. The fitted line is of the form $y = bx^2 + c$, where the fitted line shown corresponds to $b = 7.8 \times 10^{-6}\,\mathrm{nK/Hz^2}$

.

When the same procedure of pulsing the disorder onto a thermal cloud and then imaging the cloud after TOF was implemented in the experiment the results were as shown in Fig. 7.11. For the experimental data the disorder strength is expressed in terms of the linearised disorder strength. This leads to a relation where a value of 1 (maximum optical power in the first order of the AOM) corresponds to a disordered potential strength of 935 Hz. For the disorder strength calibration shown in Fig. 7.11 5 different realisations of the disorder were used for each intensity, and an average of 87 experimental images were taken for each disorder strength.

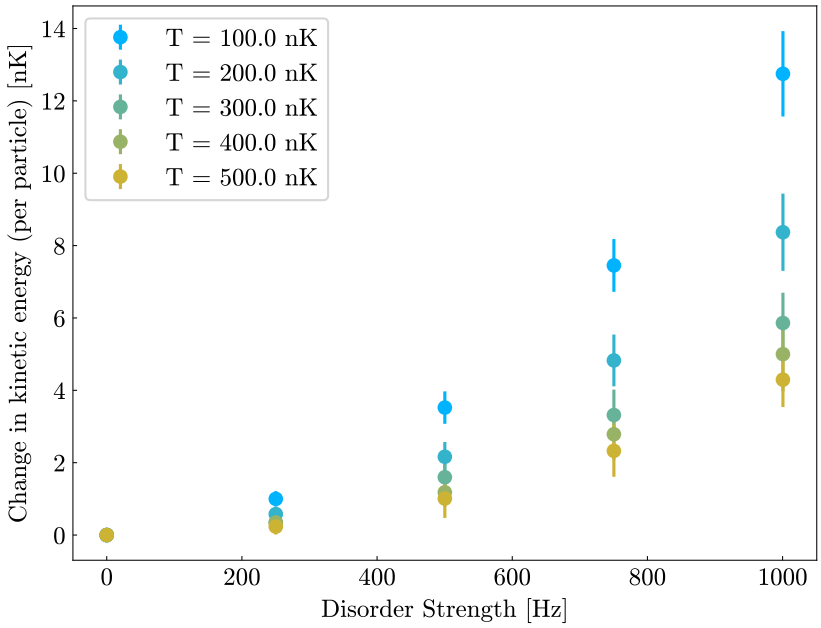


Figure 7.10: Simulation results for the change in kinetic energy imparted when pulsing a speckle potential on as described in the text, for various strengths of the speckle potential, and various initial temperatures.

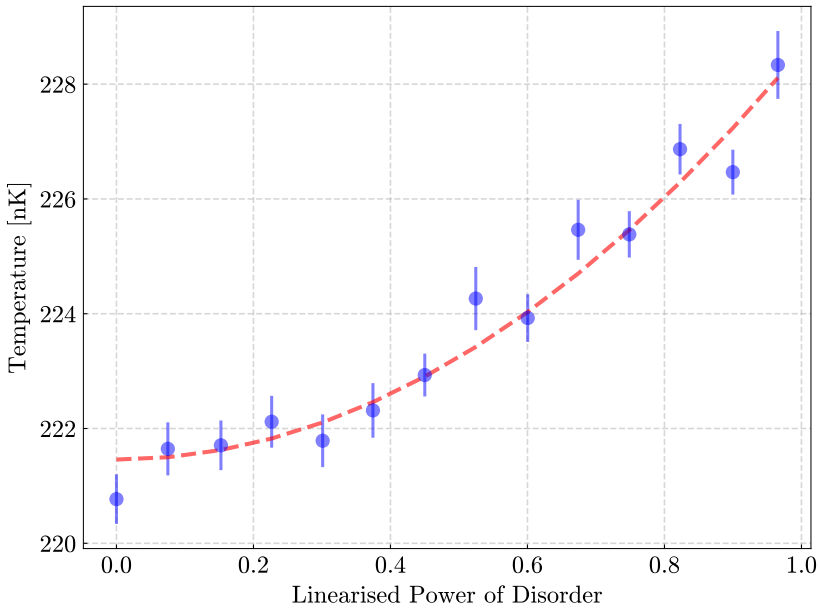


Figure 7.11: Experimental results for the change in temperature when pulsing a speckle potential, for various strengths of the speckle potential. The strength of the speckle potential is expressed in terms of the linearised power of disorder (LPD) shown in Fig. 7.7. The fitted line is of the form $y = b_2x^2 + c_2$, where the fitted line shown corresponds to b_2 =7.1 nK/LPD^2, c_2 = 221.5 nK gives the unperturbed temperature.

8 Disordered Bose Gases

A static spatially disordered potential can localise waves and therefore single particles in a quantum mechanical treatment. For classical waves this is due to scattering of the obstacles imparting random phases which causes destructive interference and an exponential decay of the amplitude at large distances. Philip W Anderson studied the case of a single quantum mechanical particle in a disordered potential and found an absence of diffusion given sufficiently short-range interactions with the disorder, this phenomenon is called 'Anderson localisation' [128]. More generally, random disorder such as random spatially varying potentials tend to act to localise particles, modifying the emergent behaviour in many-body quantum systems.

8.1 Theory of Disordered Bose Gases

How the presence of a disordered potential modifies the superfluid transition in interacting bosonic systems is called the 'dirty boson problem' [129]. This problem is of interest as it combines disorder and particle-particle interaction effects in a simple Hamiltonian, whose solution is nevertheless non-trivial. The theoretical treatment of the problem of bosons in a disordered potential is complicated by the fact that there does not exist a well-defined non-interacting limit around which it is possible to study interaction effects perturbatively. Expanding around the

non-interacting limit is complicated because the lowest lying state in the disordered system is localised and can accommodate an infinite number of bosons. Thus the introduction of even the smallest repulsion between the particles dramatically changes their collective behaviour in the thermodynamic limit.

In two dimensions, varying the strength of a disordered potential can induce a phase transition between a superfluid and a non-superfluid state, which for finite-temperatures is expected to be of the BKT type [12, 130]. A phase transition persists even when the disorder strength is varied at $T = 0$ where the system transitions into a Bose glass (BG) phase for strong disorder. The Bose glass is a disorder-localised gapless insulating phase. Since interacting bosons in a disordered potential undergo a phase transition at zero temperature the phase transition cannot be driven by thermal fluctuations, instead it is driven by quantum fluctuations and such transitions are called quantum phase transitions (QPT). The 2D bosonic superfluid to insulator transition in the presence of quenched random disorder is a prototypical QPT. While QPTs only occur at zero-temperature they nonetheless affect the phase diagram even at finite temperatures. To see why disorder might cause a quantum phase transition we remind ourselves that a particle that is spatially confined has a discrete (gapped) energy spectrum, while a free particle has a quasi-continuum of energy levels which becomes a continuous (gapless) spectrum as the system size tends to infinity [131].

Consider the spectrum of an ensemble of non-interacting identical particles in an environment with low and intermediate disorder where their collective wavefunction is not localised they have a gapless spectrum in an infinite system. However, once the disorder is strong enough to localise the wavefunction the energy spectrum suddenly changes to be the gapped spectrum of a confined particle. This non-analyticity in the energy spectrum of the system's Hamiltonian gives rise to the quantum phase transition as the disorder strength is varied. This is illustrated in Fig. 8.1. However the presence of interactions modifies the picture and the particles will occupy states which are localised in different regions of the system, where the gap between

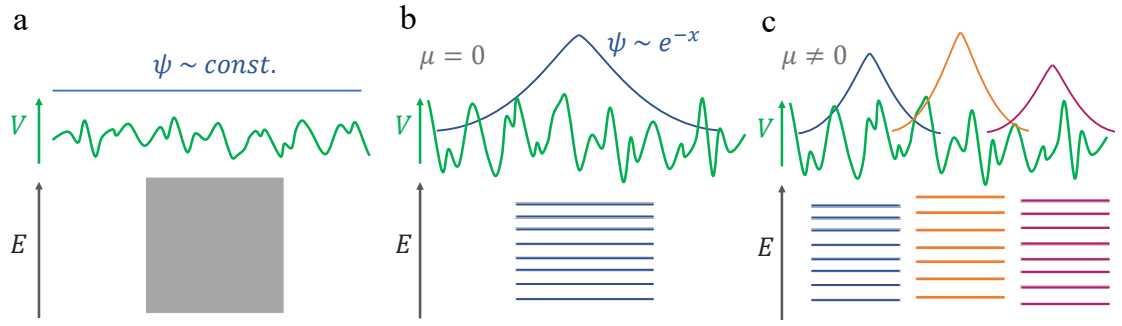


Figure 8.1: Illustration of the effect of disorder on bosons and their eigenenergy spectra. **a.** The case where the magnitude of the disorder is low, and the wavefunction is not localised so the energy eigenstates form a continuum. **b.** The case when the disorder is strong enough to localise a single particle, or all particles if $\mu = 0$, so the wavefunction is bounded and the energy eigenstates form a discrete spectrum. **c.** The different localised eigenstates of interacting bosons in strong disorder, where there might be an infinitesimal energy difference in the eigenenergies of spatially separated eigenstates leading to the Bose glass phase.

the discrete spectra associated with states localised in any two regions might be infinitesimal for a system with infinite spatial extent, as shown in panel c of Fig. 8.1.

The zero-temperature phase diagram for the disordered Bose Hubbard model for bosons on a lattice with kinetic (hopping) energy, contact interactions, and a spatially disordered potential has been mapped out theoretically [130, 132, 133]. Such studies frequently employ quantum Monte Carlo techniques. For finite temperature the case of bosons confined within a quasi-crystal, meaning the disorder is distributed as $V_j = V/2 \cos(2\pi r j + \phi_j)$ where j is the lattice site index, r is an incommensurate ratio, and ϕ_j is a random variable uniformly distributed over $\pm\pi$ [134], has been studied experimentally [135] and theoretically [136].

The phase diagrams of finite temperature bosonic systems with speckle disorder with different correlation lengths in two dimensions have been studied theoretically using a variety of techniques, we outline some of the results below. One work uses the local density approximation (LDA), a semi-classical approach incorporating the disorder as a spatially varying chemical potential [137]. This treatment finds that the presence of weak disorder slightly increases the critical temperature for the BKT transition as it compresses the gas while stronger disorder decreases the critical temperature up to a critical disorder strength where the critical temperature reaches

zero and the system is never superfluid. To study the influence of quantum effects not included in the semi-classical LDA treatment, quantum Monte Carlo studies have been conducted for 2D Bose gases in the presence of speckle disorder with a correlation length 2.24 times the healing length, similar to the situation studied experimentally in this chapter [127]. The aforementioned quantum Monte Carlo study found that the disorder monotonically decreased the critical temperature and that the reduction in critical temperature with increased disorder strength was significantly stronger compared to the predictions from the LDA analysis. The quantum Monte Carlo study in Ref. [127] found that the strength of disorder above which the system is not superfluid at any temperature was approximately halved compared to the prediction from LDA. Since the disorder results in a QPT at $T = 0$ it is expected that LDA will not capture the phase diagram accurately in this low-temperature limit. The interpolation between the QPT at $T = 0$ and the higher temperatures which should be accurately described by classical field theories is not conclusively determined.

Separate theoretical work also studied the dynamics of disordered 2D Bose gases following a quench, consisting of suddenly applying a spatially uncorrelated disorder potential (corresponding to a speckle potential with an infinitesimal length-scale). This work on the post-quench dynamics utilises a semi-classical treatment using the Gross-Pitaevskii equation to time evolve the system into an equilibrium state after the quench and found that the disorder monotonically decreased the critical temperature [120]. The work identified the phases from the functional form of the phase correlation function, $g_1(r)$, on either side of the BKT transition, this led to a crossover region in the phase diagram between the superfluid and normal phases where it could not be distinguished whether the decay of the correlations was exponential or algebraic.

Other work studying Gaussian correlated disorder with a finite correlation length found a phase diagram where increased disorder strength monotonically reduced the transition temperature, while also proposing that for strong disorder the system would enter a many-body localised (MBL) phase where it does not thermalise [12].

That work also found a SF-MBL-normal tri-critical point as a function of the disorder strength for $T = 0$. Experimental investigations using superconducting qubit arrays have also studied the phase diagram for small 2D bosonic systems on a lattice with disorder [138], proposing a quite different phase diagram compared to the works listed above, which like Ref. [12] features a SF-BG-MBL transition at $T = 0$ and a finite temperature MBL phase.

8.2 Experimental Results

To experimentally investigate the phase diagram of 2D Bose gases with different strengths of disorder we vary the temperature of our gases of ^{87}Rb atoms. This is done by varying the final frequency applied during the evaporative cooling, as shown in Fig. 2.1, this way the number of atoms and therefore the phase-space density is varied. The disordered speckle potential is ramped up slowly over 4.9 s during the TAAP phase before the clouds have condensed, this way the condensation occurs in the disordered potential and also reduces excitations from ramping up the disorder. The single RF potential, generated with an RF tone at 7.1 MHz, is then slowly split into two by forming an MRF potential by introducing two additional frequency components at 75 kHz above and below the central frequency, leading to decoupled 2D gases. The splitting takes place over 450 ms as in the earlier experimental investigations studying equilibrium properties reported in Ch. 5 and Ch. 6. After splitting the condensates are held in the MRF potential for 300 ms before they are released and imaged.

In Fig. 8.2 we show that the total atom number stays constant within measurement error while the temperature decreases monotonically with the experimental control parameter, 'Final Freq.' which defines the lowest frequency reached by the RF field which ejects energetic atoms during evaporative cooling. To obtain the temperature and atom number data shown in Fig. 8.2 we repump and image the whole cloud as in Ch. 3; the fitting analysis used to determine temperature and the number of atoms used $\sim$ 25 experimental images which were programmed

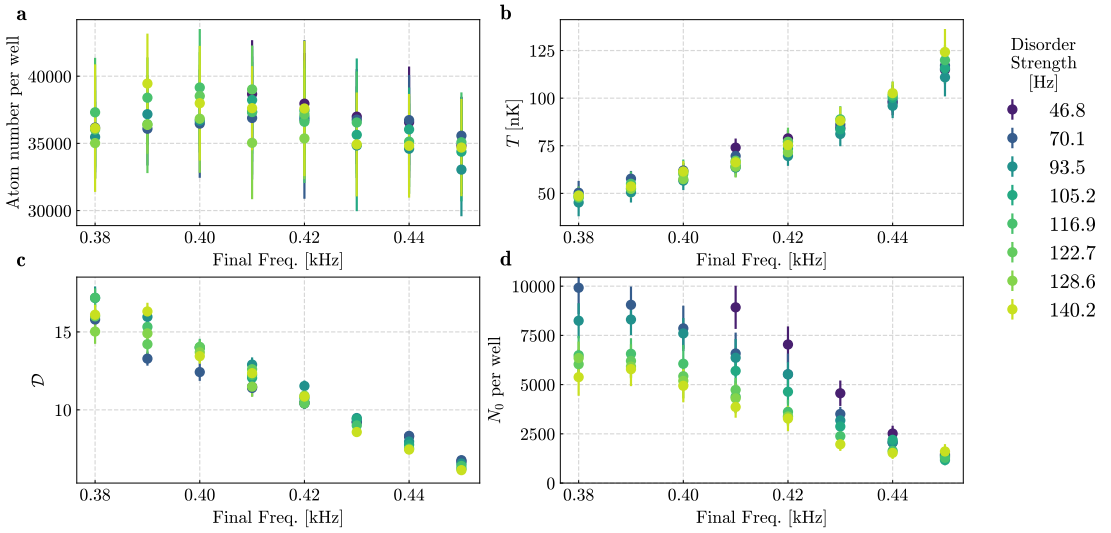


Figure 8.2: Thermodynamic properties of gas when varying the disorder strength and temperature. **a.** The total number of atoms in each well. **b.** The temperature of the gas. **c.** The phase-space density, calculated using the total number of atoms in each well and the extracted temperature. **d.** The number of atoms in the quasi-condensate, per well. The number of atoms in the quasi-condensate per well is proportional to the chemical potential μ and its effect on the region of the phase diagram probed is shown in Fig. 8.3.

to be taken interspersed with the images used for fringe analysis in order to be sensitive to experimental drifts.

In terms of the thermodynamic variables we therefore probe a region of the phase diagram as shown in Fig. 8.3, where we also express the disorder in terms of the chemical potential computed using $\mu = gn_0$, where g is the interaction parameter and n_0 is the mean 2D density of atoms in the quasi-condensate computed for a disc with radius 22.5 μm. The different combinations of thermodynamic quantities and disorder strength shown on the axes in Fig. 8.3 are to aid the comparison of our results and theoretical works on the 2D dirty Bose problem [12, 119, 120, 127, 137].

The 2D phase correlation functions, obtained using FFT analysis of the images as described for the case of coupled bilayers in Ch. 6, are shown in a grid in Fig. 8.4. This analysis is comparable to the numerical and theoretical work on 2D Bose gases in disordered potentials by Scoquart et al. [120, 139] where they inspect the correlation functions to identify the phases in equilibrium and map out a phase diagram.

We note from Fig. 8.4 that either increasing temperature (shown as decreasing PSD) or increasing disorder strength both cause $g_1(r)$ to decay more rapidly with

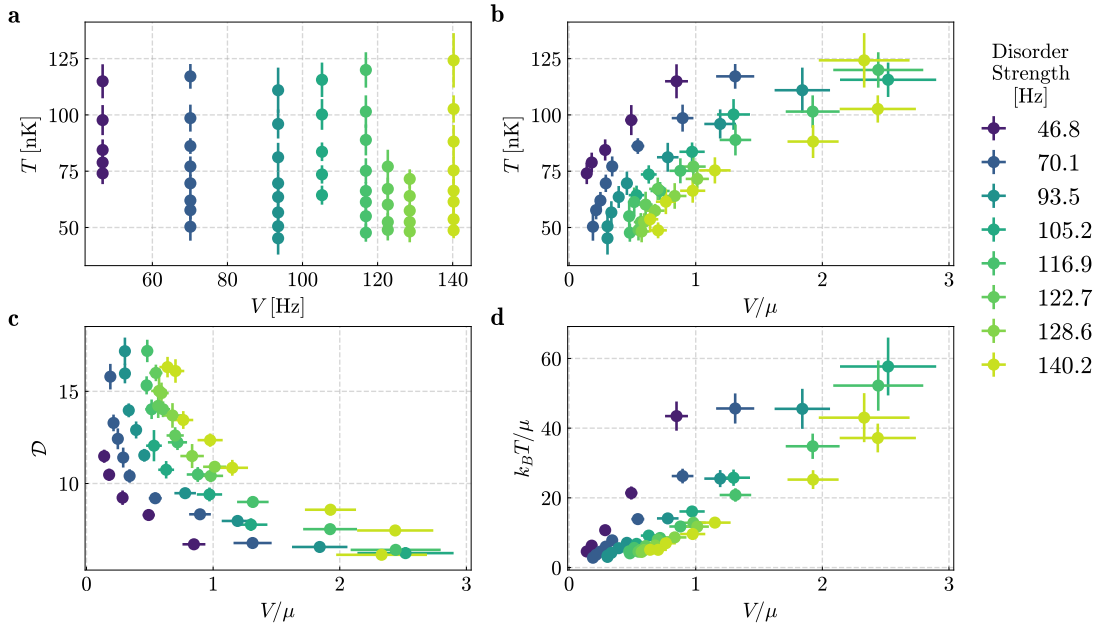


Figure 8.3: Region of temperature and disorder phase diagram probed. **a.** The sampled points in terms of the disorder strength obtained using the calibration described in the previous section and the temperature. **b.** The sampled points in terms of the temperature and the disorder strength expressed as a dimensionless ratio with respect to the chemical potential. **c.** The sampled points shown in terms of the phase-space density D and the disorder potential strength divided by the chemical potential. **d.** The sampled points shown in terms of the dimensionless ratios k_BT/μ and the disorder potential strength divided by the chemical potential.

distance. We observe a similar crossover regime featuring rapid but algebraic decay of $g_1(r)$ as in Ref. [120]. This regime might be due to the fact that while the disorder isolates different parts of the condensate and thus reduces the phase coherence the non-uniform density might impair vortex unbinding away from the low density regions where they are expected to arise due to the comparatively lower energy cost. This could lead to the algebraic decay of g_1 arising from thermally populated phononic fluctuations without the exponential decay arising from vortex excitations.

We studied the algebraic decay exponent η of the experimentally obtained $g_1(r)$ functions shown in Fig. 8.4 when fitted with an analytical model for algebraic decay, as expected in the superfluid phase. We also computed the correlation length when fitted with a model of exponential decay expected in the normal phase, reported as a fraction of the Thomas-Fermi radius. These quantities are shown in Fig. 8.5.

We wish to identify the superfluid and normal phases to construct a phase

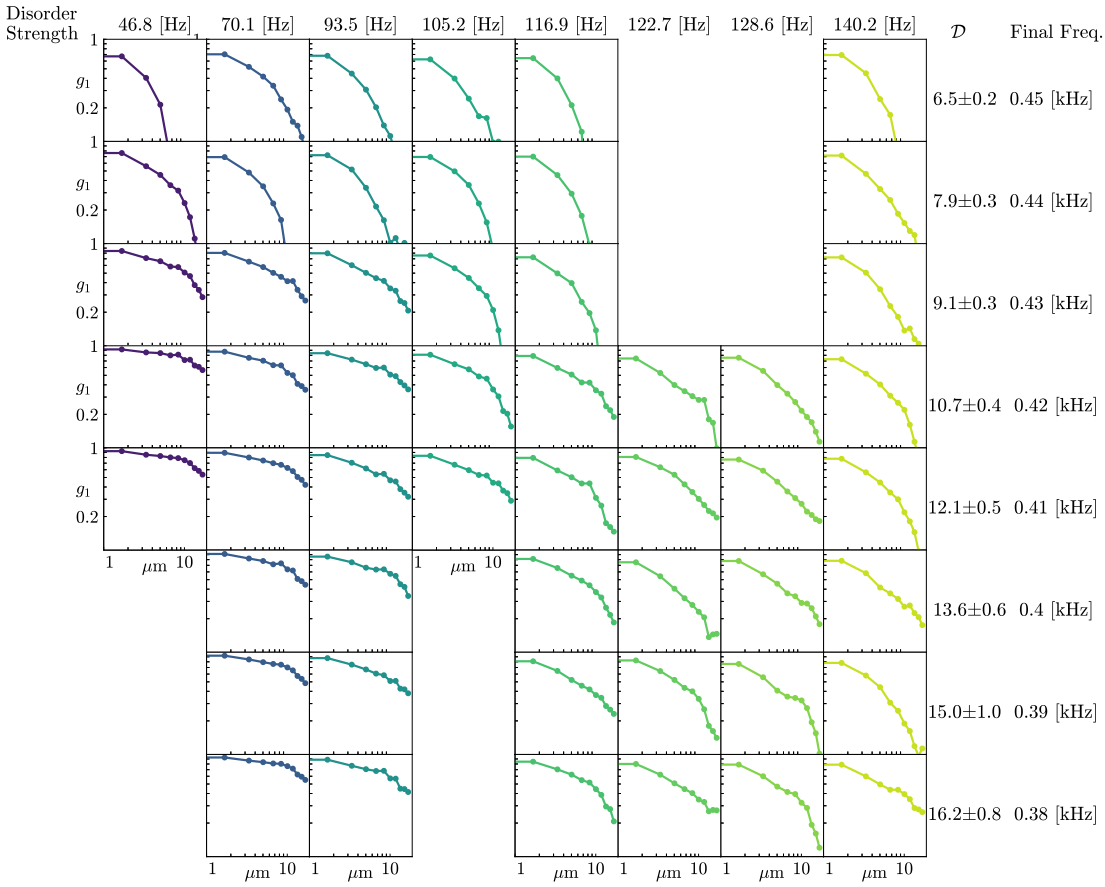


Figure 8.4: Phase correlation functions, g_1, when varying temperature and disorder strength. The experimental points sampled are shown in a grid where a plot's vertical position corresponds to the value of the Final Freq. experimental parameter which determines the temperature and PSD as in Fig. 8.2. The horizontal position of the plots correspond to the strength of the disordered potential applied also shown in Fig. 8.3. For each combination of Final Freq. and disorder strength the g_1 function was computed using ~ 60 experimental images.

diagram. The phases are identified using the different signatures of the superfluid and normal phases in a clean system, these are: (1) in the superfluid phase we expect the correlations to decay algebraically while they decay exponentially in the normal phase, we therefore investigate the ratio of the χ_r values of the two models, (2) in the superfluid phase we expect quasi-long-range order quantified by $r_{corr}/r_{TF} \geq 0.9$, and (3) in a clean system we expect the decay exponent of the superfluid to be $\eta \leq 0.2$, as seen in Fig. 5.6. When all of these signals, shown separately in Fig. 8.6, are consistent with either the superfluid or normal phase we have coloured the corresponding region of the phase diagram blue, or red respectively; while the cases

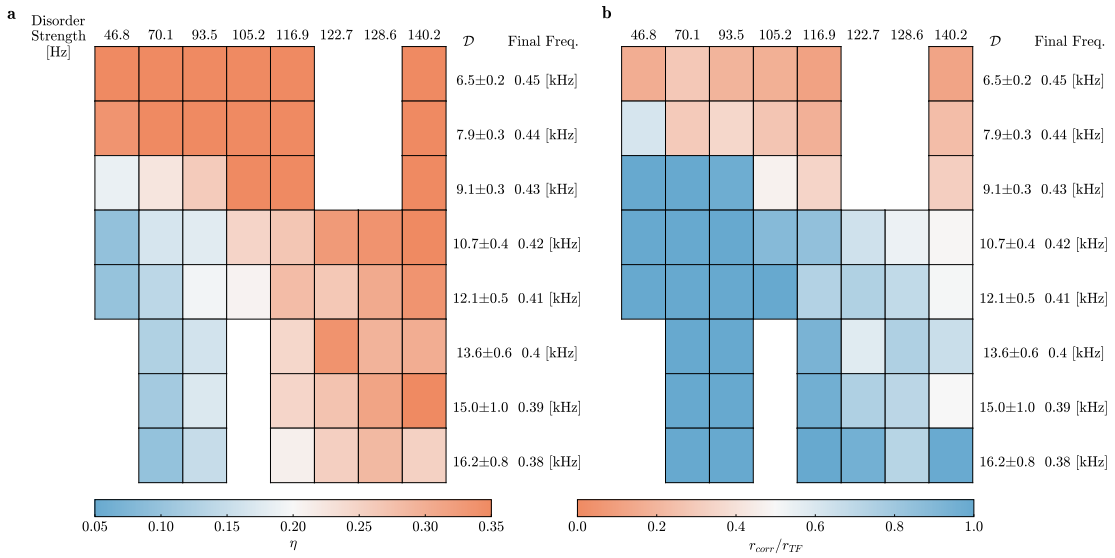


Figure 8.5: Algebraic and exponential decay rates of g_1 functions. The vertical and horizontal ordering of the data is consistent with Fig. 8.4. **a.** The algebraic decay rate η obtained from fitting the g_1 functions with a model of algebraic decay. **b.** The exponential decay rate, called the correlation length r_{corr} expressed as a fraction of the Thomas-Fermi radius obtained from fitting the g_1 functions with a model of exponential decay.

where there is an inconsistency between the different signals are a salmon colour. In Fig. 8.7 we show the classifications of the different data points in terms of the thermodynamic variables shown in Fig. 8.3.

We also study the number of vortices present in the relative phase-mode of the gases. This is carried out analogously to the coupled-bilayer case in Ch. 6, where we look for phase jumps in the interference patterns. Fig. 8.8 shows the number of vortices as a function of phase-space density for the different disorder strengths probed. The data are fitted with an exponential decay model $N_v \propto e^{-\gamma D}$ motivated by earlier work, where in a clean system we found $\gamma = 0.56(5)$ [6, 34, 65]. The fitting function is motivated by Ref. [140] where the decay exponent γ relating the vortex density to the PSD depends on the vortex core energy. The varying rate of exponential decay is shown in Fig. 8.9.

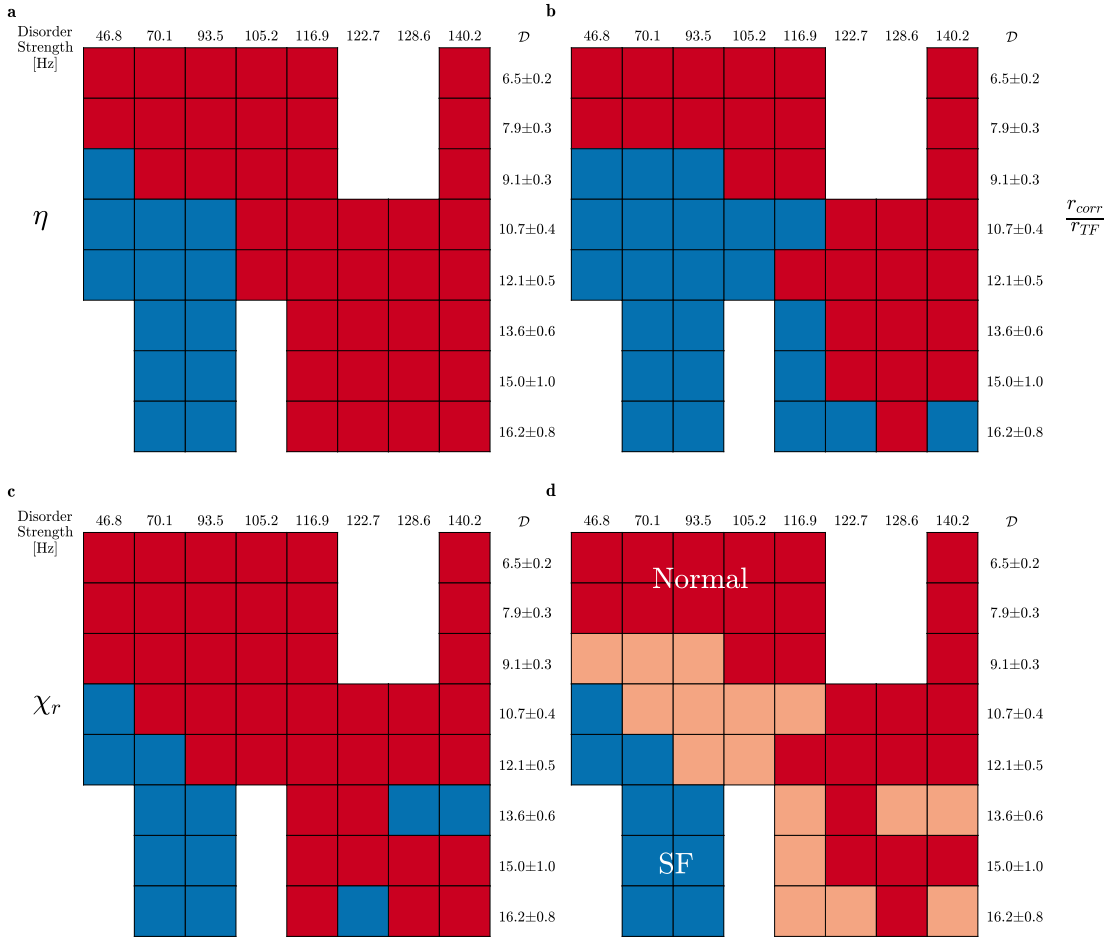


Figure 8.6: Compilation of the different signals indicating superfluid or normal regime. The vertical and horizontal ordering of the data is consistent with Fig. 8.4. **a.** Squares are coloured blue if the value of η is consistent with superfluid, otherwise red. **b.** Squares are coloured blue if the value of r_{corr}/r_{TF} is consistent with superfluid, otherwise red. **c.** Squares are coloured blue if the value of χ_r is consistent with superfluid, otherwise red. **d.** The squares are coloured blue if all the properties shown in panels **a**, **b**, **c** are consistent with superfluid, and red if none of them are; if some are consistent with superfluid the square is shown as salmon.

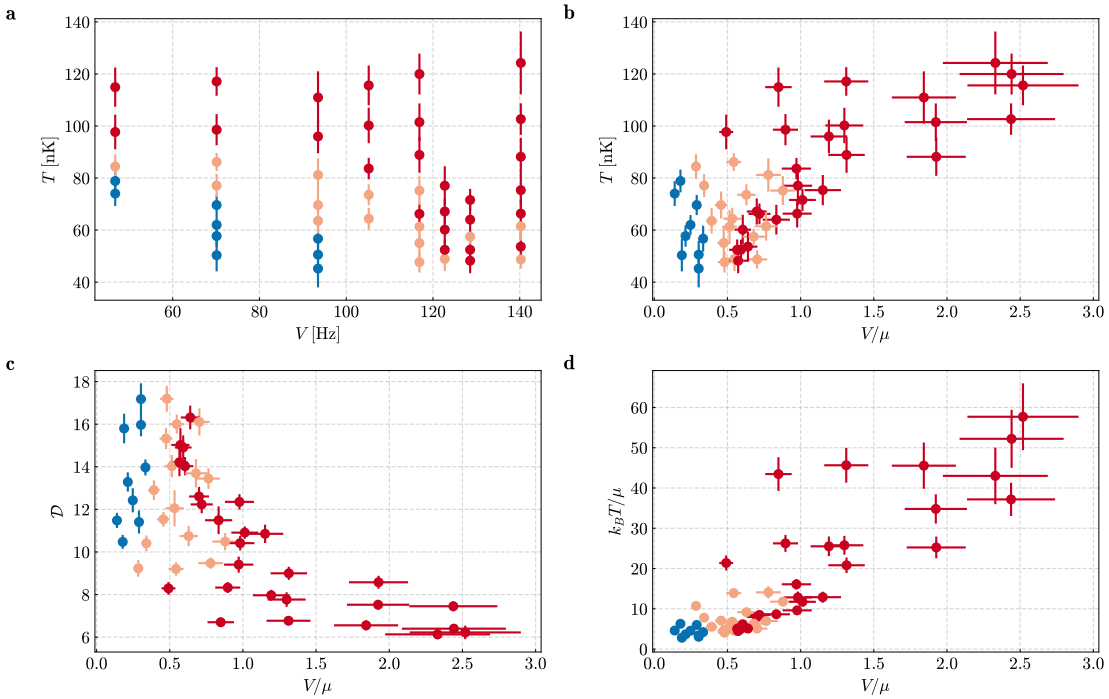


Figure 8.7: Phase identification shown in terms of thermodynamic variables shown in Fig. 8.3. The points are coloured blue if all the properties shown in panels **a**, **b** and **c** of Fig. 8.6 are consistent with superfluid, and red if none of them are, those where only some criteria are consistent with superfluid are shown as salmon. These colours are consistent with Fig. 8.6 **d**.

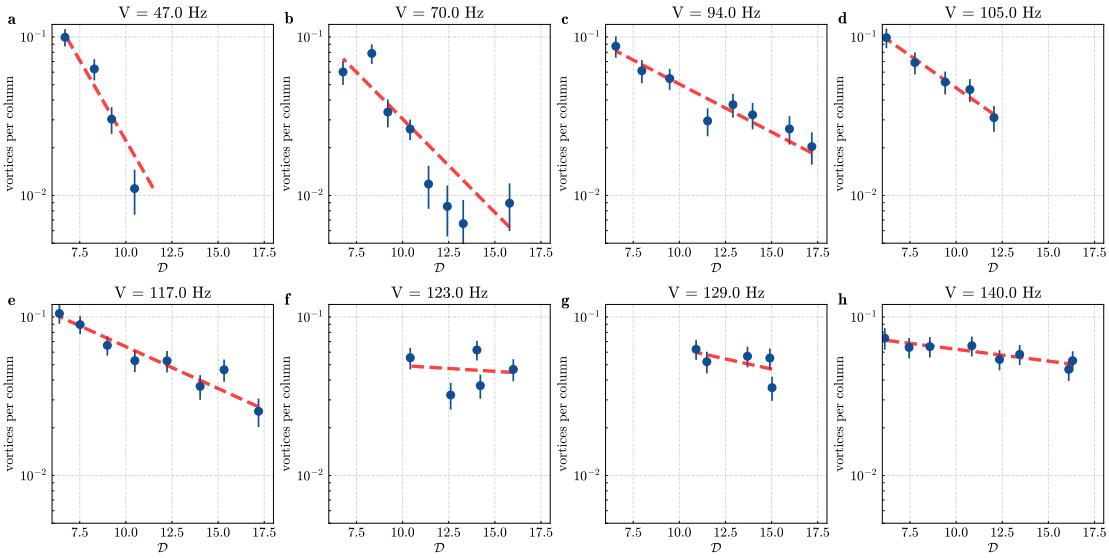


Figure 8.8: Effect of disorder strength on vortex density. The number of vortices per image column are shown as blue dots and the best fits for the exponential decay model are shown as a red dashed line for all the disorder strengths probed.

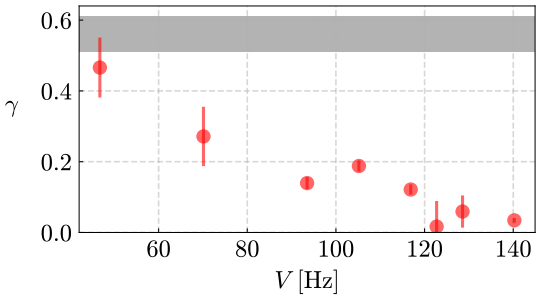


Figure 8.9: Vortex proliferation rate as a function of disorder strength. Here we show the value of γ from the $N_v \propto e^{-\gamma D}$ fits shown in Fig. 8.8. The grey shaded region shows the interval for a clean system found in earlier experimental work and MC simulations of clean systems [6, 34, 65].

8.3 Numerical Simulations

To numerically investigate the phase-diagram of 2D Bose gases subject to the disordered potential realised in the experiment we performed Monte Carlo simulations, utilising the Metropolis-Hastings algorithm described in Ch. 2. The Hamiltonian is constructed using disorder numerically generated by the same method as in Eq. 7.9 with magnitude V, and also a boundary enclosing a circle with radius r_0 =22.5 μm, using a smooth boundary $V_{boundary}(x,y) = \tanh\left(\frac{\sqrt{x^2+y^2}-r_0}{\Delta r}+1\right)$, where $V_0 = 1\,\mathrm{kHz}$ and $\Delta r = 2.5\,\mu\mathrm{m}$. The functional form for the intensity of the light making the boundary is motivated by earlier work [13]. The simulation is performed on a 128×128 lattice with a lattice spacing chosen to be smaller than the healing length, $\xi = 1\,\mu$m, which is the characteristic smallest length scale for the fluctuations. Giving a discretised Hamiltonian on a lattice with the appearance of a Bose-Hubbard model [48],

$$H = -J_h \sum_{\langle i,j \rangle} (\psi_i^* \psi_j + \psi_j^* \psi_i) + \frac{U}{2} \sum_i n_i^2 + \sum_i (V_i - \mu) n_i \tag{8.1}$$

where $J_h = \hbar^2/2ml^2$, with l denoting the simulation grid spacing (set to l = 0.5μm for the simulations in this chapter), $V_i = V_{boundary,i} + V_{speckle,i}$ as in Eq. 7.9 and $U = g/l^2$. The chemical potential was used as a free parameter to match the number of atoms in the Monte Carlo results with the values measured experimentally in Fig. 8.2. The chemical potential was varied to minimise the difference between the experimentally detected atom number and the atom number in the simulation using a Nelder-Mead minimisation routine [141]. Treating the chemical potential as a free parameter in this way matches what was done in the Monte Carlo simulations of the tunnel-coupled bilayers in Ch. 6. The temperatures in the simulations were varied over a range to match the experimental data. For each combination of disorder strength and temperature 1000 fields were generated using Monte Carlo sampling, corresponding to 100 fields for 10 different realisations of the speckle disorder. The temperatures, phase space densities and atom numbers in the Monte Carlo simulations are shown in Fig. 8.10; the temperatures were selected so that the phase

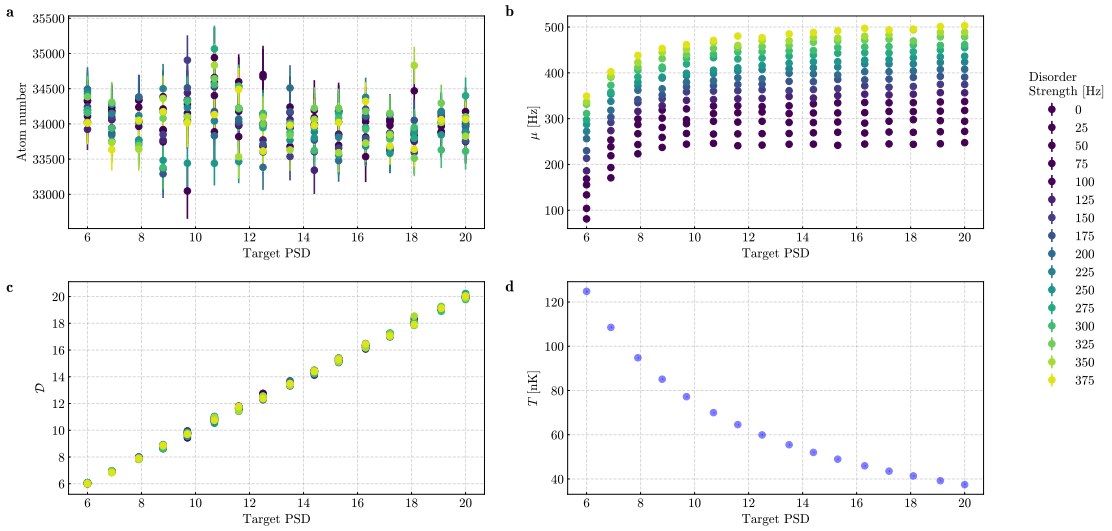


Figure 8.10: Thermodynamic properties of the Monte Carlo simulated fields. **a.** The total number of atoms in the simulated field, error bars correspond to the standard deviation of the atom number in the 1000 simulated fields. **b.** The values of the μ parameter in the Monte Carlo simulation to match the number of atoms in the experimental data for a range of temperatures and disorder strengths. **c.** The phase-space density, calculated from the total number of atoms in the fields and the specified temperature compared to the target phase space densities. **d.** The temperature in the Monte Carlo simulations as a function of target phase space densities.

space densities overlap the region probed in the experiment. The different chemical potentials in the simulation were chosen to achieve the range of target phase space densities. The radially averaged phase correlation functions g_1 from the numerical simulations are shown in Fig. 8.11. We show the algebraic and exponential decay coefficients computed from the correlation functions obtained from the simulations shown in Fig. 8.11 (in analogy with Fig. 8.5) these are shown in Fig. 8.12. This leads to the different signals indicating whether the system is in the superfluid or normal state shown in Fig. 8.13. Finally we also see vortex suppression in our Monte Carlo simulations, as shown in Fig. 8.14 and Fig. 8.15. The varying rate of exponential decay of the number of vortices with PSD is shown in Fig. 8.15. We note that we see the same qualitative behaviour in the simulation and the experimental data, namely that: the critical temperature shifts downwards with increased disorder and there is a reduced dependence of number of vortices on temperature as disorder increases.

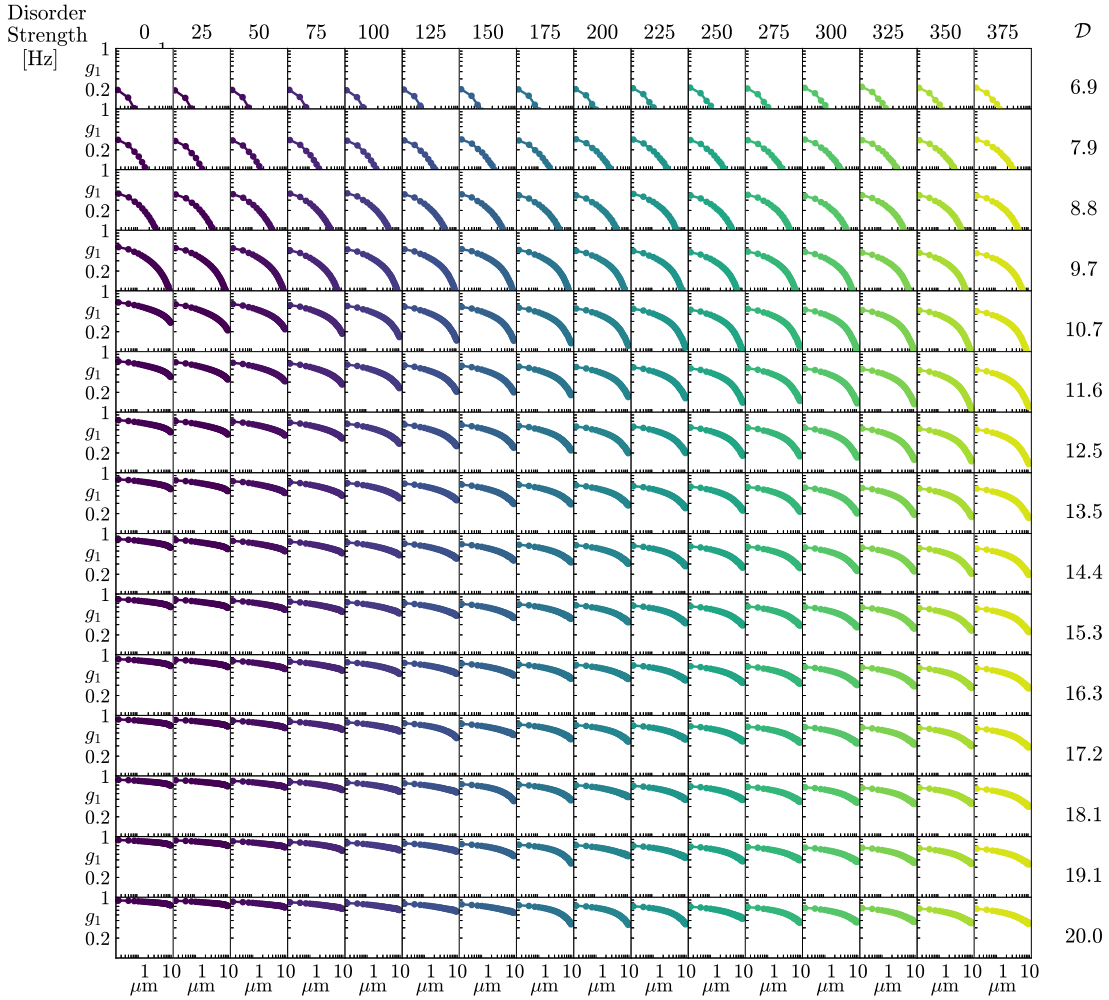


Figure 8.11: Phase correlation functions from simulations, g_1, when varying temperature and disorder strength. The experimental points sampled are shown in a grid where a plot's vertical position corresponds to temperature and PSD as in Fig. 8.2. The horizontal position of the plots corresponds to the strength of the disordered potential.

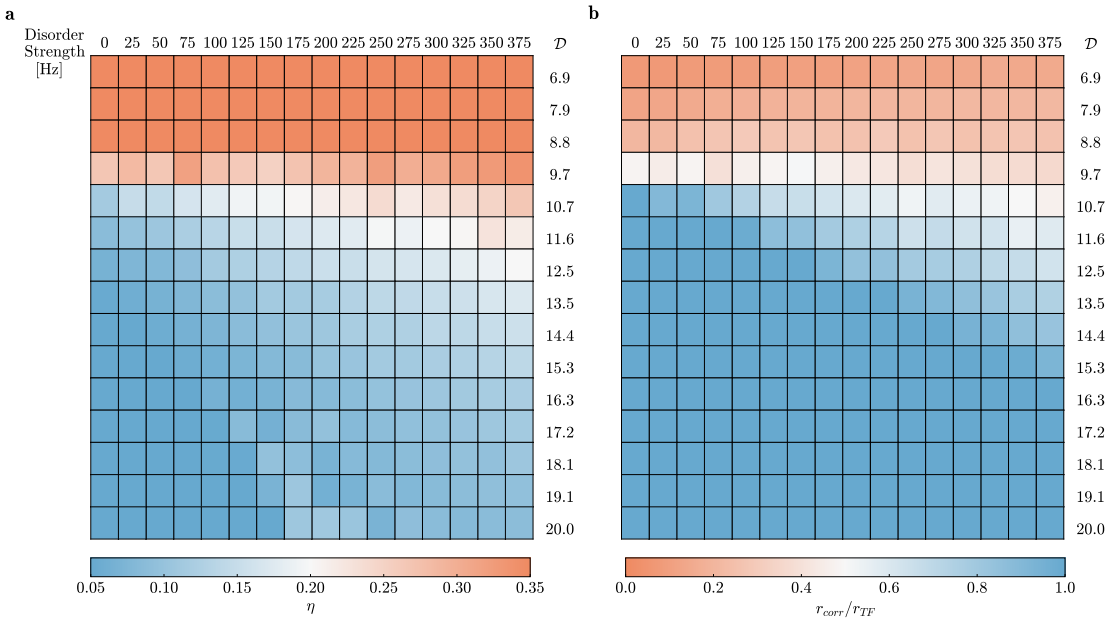


Figure 8.12: Algebraic and exponential decay rates of g_1 functions. The vertical and horizontal ordering of the data is consistent with Fig. 8.4. **a.** The algebraic decay rate η obtained from fitting the g_1 functions with a model of algebraic decay. **b.** The exponential decay rate, called the correlation length r_{corr} expressed as a fraction of the Thomas-Fermi radius obtained from fitting the g_1 functions with a model of exponential decay.

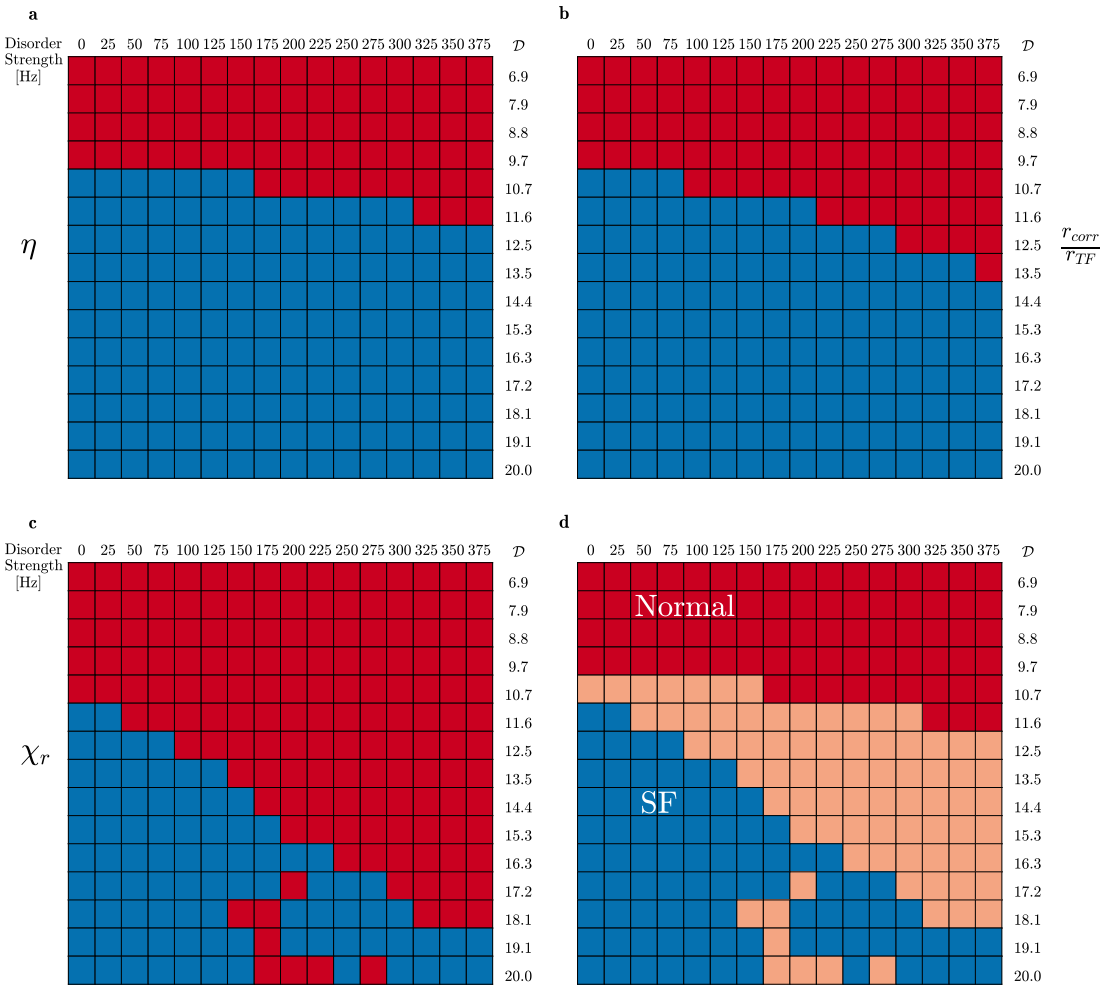


Figure 8.13: Different signals indicating superfluid or normal regime from simulation. The vertical and horizontal ordering of the data is consistent with Fig. 8.11. **a.** Squares are coloured blue if the value of η is consistent with superfluid, otherwise red. **b.** Squares are coloured blue if the value of r_{corr}/r_{TF} is consistent with superfluid, otherwise red. **c.** Squares are coloured blue if the value of χ_r is consistent with superfluid, otherwise red. **d.** The squares are coloured blue if all the properties shown in panels **a**, **b**, **c** are consistent with superfluid, and red if none of them are, if some are consistent with superfluid the square is shown as salmon.

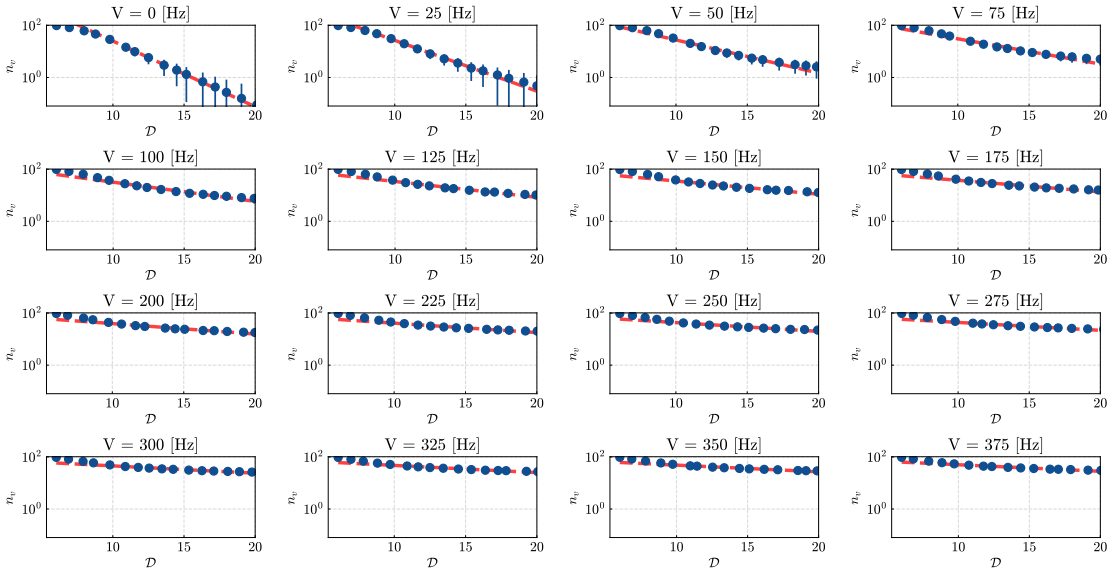


Figure 8.14: Effect of disorder strength on vortex number from simulation. The average number of vortices per simulation field are shown as blue dots and the best fits for the exponential decay model are shown as a red dashed line for all the disorder strengths simulated.

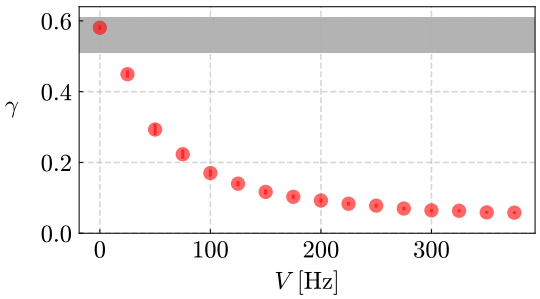


Figure 8.15: Vortex decay exponent with increasing PSD as a function of disorder strength from simulation. Here we show the value of γ from the $N_v \propto e^{-\gamma D}$ fits shown in Fig. 8.14. The grey shaded region shows the interval for a clean system found in earlier work [6, 34, 65].

8.4 Summary and Outlook

We observe the same qualitative shift of critical point in the experimental data and the Monte Carlo simulations with classical fields, including rough quantitative agreement. The observed change in vortex number with disorder is also consistent between the experimental results and numerical simulation. The effect of disorder on the vortex number likely stems from the reduced energy cost of creating vortices in the lower density regions created by disorder, leading to increased vortex nucleation. A reduced energy cost associated with a vortex would manifest as a reduced Boltzmann weight for phase and density field configurations with a vortex and thus a reduced dependence of the vortex number on temperature, as seen in Fig. 8.9 and Fig. 8.15. Ref. [140] presents a theoretical model relating the dependence of vortex number on PSD, captured by γ in our analysis, to the vortex core energy in clean systems. To investigate the possible role of the disorder in nucleating and pinning vortices, spatial correlations between the intensity of the disordered potential at different points and the vortex locations will be studied in future work.

The theoretical interpretation of the results presented in this chapter is ongoing work benefitting from collaboration with theorists. The continued investigation as to how to interpret our results will also benefit from significantly increased computational resources to study the effect of quantum fluctuations on the phase diagram. At present we cannot determine to what extent the observed behaviour is due to classical effects of disorder such as those captured by LDA and percolation or determine if any of the observed effects might be due to quantum effects such as localisation, or tunnelling between regions classically separated by percolation.

Precisely determining the phase diagram for our finite-sized system experimentally is complicated by the observed algebraic falloff at rates greater than those occurring in a clean system. Thus, to better understand the phase diagram we intend to perform additional experimental investigations to analyse the statistics of the interference contrast, as well as studying the Binder cumulant calculated using the statistics of the contrast of the interference patterns as introduced in our recent work [142]. Distributions of the interference contrast have been proposed to both

reveal signatures of a glassy phase [143] and provide an additional signal of when the transition is crossed. A signal from the contrast statistics would be independent of the form of the correlation function and the number of vortices, and therefore be helpful in precisely determining the transition point within the identified crossover regime. In addition to studying the order parameter distributions using contrast statistics, a natural extension to this work is to study the dynamical behaviour as the disorder-induced phase transition is crossed rapidly, both to study predictions of universal scaling exponents in disordered Bose systems [144, 145] using the methodology of our recent work on quenches in coupled bilayers [35] and since the relaxation timescales are expected to be significantly slower than for a clean system if the system is in a disorder-induced glassy phase. Quench experiments could therefore reveal possible glassy dynamics induced by the disorder.

Another study of interest will be to study the spatial distributions of the locations of the vortices as the disorder strength is varied. This would utilise vertical imaging and the vortex detection technique using a convolutional neural network developed by our research group during the undergraduate project of Magnus Sesodia, supervised by Abel Beregi [65]. Comparing the locations of the vortices with the spatial structure of the disorder potential, obtained from in-situ images, will allow us to investigate vortex pinning. Furthermore, the statistical distribution of the locations of vortices at different times after a quench would provide an additional viewpoint for observing possible disorder-induced glassy dynamics.

9 Conclusion and Outlook

This work presents a number of technical and scientific advancements for engineering and probing novel phases of matter and emergent phenomena using two-dimensional ultracold gas experiments.

This includes, to our knowledge, the first experimental example of evaporative cooling to quantum degeneracy carried out entirely in a linearly polarised RF-dressed potential. This has applications for creating ultracold quantum gases with significantly reduced random excitations in tuneable RF-dressed potentials. Gases created using this technique are useful for reaching the lower temperature where quantum fluctuations and entanglement are expected to shape the emergent behaviour of our ultracold gases [146]. Furthermore, such ultracold quantum gases with reduced random excitations are likely to be suitable for sensing schemes utilising deliberately generated phononic excitations in ultracold gases [38, 147].

We also introduce a novel density-noise readout technique to obtain information about the symmetric excitations in bilayer systems. We benchmark this scheme experimentally and find agreement between, analysis of matter-wave interference fringes, single layer density noise measurements, and double layer density noise measurements. Capturing and analysing short time-of-flight interference images taken from above opens up the development of improved reconstruction techniques both similar to the ones used for one-dimensional Bose gases [56] and analogous to

the phase retrieval problem for classical optics [67]. The goal would be single-shot reconstruction of the phase and density fields in each experimental run, this information would allow calculating higher-order statistics, as in our work analysing the statistics of interference contrast [142], as well as studying entanglement [148]. The improved imaging system due to be installed on the new generation apparatus will enable further work on interferometric readout from our ultracold gas experiments.

Using the new density noise readout scheme we study experimentally how quantum tunnelling between two-dimensional bilayers affects the phase diagram, identifying the theoretically predicted double-layer superfluid phase. This is a phase where tunnel-coupling allows the system to be superfluid at higher temperatures than otherwise and where topological defects in the relative phase-field of the order parameter are suppressed. For future work the controlled tunnelling between the layers can be periodically modulated to realise Hamiltonians which are periodic in time. Using Floquet engineering to create effective Hamiltonians [149] could allow changing the sign of the tunnelling term between the bilayers in an effective Hamiltonian to realise a BKT-paired phase [87, 90].

Additionally, we performed an experimental upgrade to be able to project a set of repeatable and distinct speckle patterns onto our gases to realise disordered potentials. This allows us to study the effect of multiple disordered potentials drawn from a single ensemble. We are able to drive the system across a Berezinskii-Kosterlitz-Thouless transition by increasing the strength of the disordered potential. For the temperatures studied we observe a phase diagram which is qualitatively consistent with numerical mean-field simulations. In the experiment we observe that the disorder affects how the number of topological defects changes with the phase-space density of the gas, a behaviour which also is seen in the numerical simulations. This indicates that the vortex-core energy in the system changes significantly as the disorder strength is increased. Having experimentally established the equilibrium phase diagram in our parameter regime a natural next step is to study the dynamics as the phase transition is crossed, similarly to our work on out-of-equilibrium Bose gases [35, 93]. The disordered potential added to the experiment opens the door

for a large number of experimental investigations, including studying quenches and dynamics in disordered two-dimensional bosonic systems. A next step would be to realise programmable disordered potentials using a digital micromirror device. While this requires changes to our optical layout and imaging system it would allow for better control over the properties of the disordered potential. This will allow us to, among other things, investigate disorder with different spatial correlations [150] and to study disorder with bimodal intensity distributions [151].

The new evaporative cooling results and novel readout technique in this thesis are two broadly relevant contributions to ultracold gas experiments and their application for quantum simulation, while the experimental results in this thesis advance our understanding of tunnel-coupled two-dimensional bilayer systems and disordered bosonic systems.

Appendices

A

Detailed Bilayer Density Noise Calculation

The density-density correlations of bilayers of ultracold bosons after TOF, differs from the situation studied in earlier works [53, 54] as there it was assumed that the system consisted of a single 2D quasi-condensate with a translationally invariant wavefunction, the work also considered density correlations integrated over the z-direction. This reduces the problem to a 2D problem with translational invariance. Meanwhile in this calculation we are interested in the effect when two 2D quasi-condensates are separated in the z direction. Thus, the interference will not only stem from a single quasicondensate at different points interfering, but also the different quasicondensates interfering. Many of the arguments and steps from the calculation for a single 2D layer carry over with a key difference that while we assume that the wavefunction is still translationally invariant in the xy-plane this is not true in the z direction. Just as in the case of a single layer the time evolution of the bosonic field operator is given by

$$\hat{\mathbf{\Psi}}(\boldsymbol{r},t) = \int d^3\boldsymbol{r}' G_3(\boldsymbol{r}-\boldsymbol{r}',t)\hat{\mathbf{\Psi}}(\boldsymbol{r}',0) \tag{A.1}$$

Where the Green's function when evolving without an external potential is

$$G_3(\boldsymbol{r}-\boldsymbol{r}',t) = G_1(x-x',t)G_1(y-y',t)G_1(z-z',t), \tag{A.2}$$

where

$$G_1(r,t) = \sqrt{\frac{m}{2\pi i\hbar t}} e^{\frac{im}{2\hbar t}r^2}. \tag{A.3}$$

Thus the density at a point is given by

$$\begin{aligned}\hat{n}(\boldsymbol{r},t) &= \hat{\boldsymbol{\Psi}}^\dagger(\boldsymbol{r},t)\hat{\boldsymbol{\Psi}}(\boldsymbol{r},t)\\ &= \int d^3\boldsymbol{v}\int d^3\boldsymbol{w} G_3^*(\boldsymbol{r}-\boldsymbol{v},t)\hat{\boldsymbol{\Psi}}^\dagger(\boldsymbol{v},0)G_3(\boldsymbol{r}-\boldsymbol{w},t)\hat{\boldsymbol{\Psi}}(\boldsymbol{w},0)\\ &= A^3\int d^3\boldsymbol{v}\int d^3\boldsymbol{w} e^{\frac{-im}{2\hbar t}(\boldsymbol{r}-\boldsymbol{v})^2}\hat{\boldsymbol{\Psi}}^\dagger(\boldsymbol{v},0)e^{\frac{im}{2\hbar t}(\boldsymbol{r}-\boldsymbol{w})^2}\hat{\boldsymbol{\Psi}}(\boldsymbol{w},0)\end{aligned} \tag{A.4}$$

introducing $A = \frac{m}{2\pi\hbar t}$ (the imaginary part vanishes since the Green's functions are complex conjugated) as in Seigl's thesis [54] (although he seems to arrive at a different power in the prefactor) to simplify the notation. Switching to centre-of-mass coordinates, $\boldsymbol{s} = \boldsymbol{v} - \boldsymbol{w}$, $\boldsymbol{S} = 1/2(\boldsymbol{v}+\boldsymbol{w})$ the exponentials can be combined as

$$\begin{aligned}\hat{n}(\boldsymbol{r},t) &= A^3\int d^3\boldsymbol{s}\int d^3\boldsymbol{S} e^{\frac{-im}{2\hbar t}(\boldsymbol{r}-\boldsymbol{S}-\frac{\boldsymbol{s}}{2})^2}\hat{\boldsymbol{\Psi}}^\dagger(\boldsymbol{v},0)e^{\frac{im}{2\hbar t}(\boldsymbol{r}-\boldsymbol{S}+\frac{\boldsymbol{s}}{2})^2}\hat{\boldsymbol{\Psi}}(\boldsymbol{w},0)\\ &= A^3\int d^3\boldsymbol{s}\int d^3\boldsymbol{S} e^{\frac{-im}{\hbar t}(\boldsymbol{S}-\boldsymbol{r})\cdot\boldsymbol{s}}\hat{\boldsymbol{\Psi}}^\dagger(\boldsymbol{S}+\frac{\boldsymbol{s}}{2},0)\hat{\boldsymbol{\Psi}}(\boldsymbol{S}-\frac{\boldsymbol{s}}{2},0).\end{aligned} \tag{A.5}$$

Eq. A.5 allows us to write the density-density correlation function as

$$\begin{aligned}\langle\hat{n}(\boldsymbol{r}_1,t)\hat{n}(\boldsymbol{r}_2,t)\rangle =& A^6\int d^3\boldsymbol{s}\int d^3\boldsymbol{S}\int d^3\boldsymbol{u}\int d^3\boldsymbol{U} e^{\frac{-im}{\hbar t}(\boldsymbol{S}-\boldsymbol{r}_1)\cdot\boldsymbol{s}}e^{\frac{-im}{\hbar t}(\boldsymbol{U}-\boldsymbol{r}_2)\cdot\boldsymbol{u}}\\ &\times\left\langle\hat{\boldsymbol{\Psi}}^\dagger(\boldsymbol{S}+\frac{\boldsymbol{s}}{2},0)\hat{\boldsymbol{\Psi}}(\boldsymbol{S}-\frac{\boldsymbol{s}}{2},0)\hat{\boldsymbol{\Psi}}^\dagger(\boldsymbol{U}+\frac{\boldsymbol{u}}{2},0)\hat{\boldsymbol{\Psi}}(\boldsymbol{U}-\frac{\boldsymbol{u}}{2},0)\right\rangle.\end{aligned} \tag{A.6}$$

Normal ordering the operators, as in the single-layer derivation, we can identify the density-density correlation function as [54]

$$\begin{aligned}g_2^{3\mathrm{D}}(\boldsymbol{r}_1,\boldsymbol{r}_2,t) =& \frac{A^6}{n_0^2}\int d^3\boldsymbol{s}\int d^3\boldsymbol{S}\int d^3\boldsymbol{u}\int d^3\boldsymbol{U} e^{\frac{-im}{\hbar t}(\boldsymbol{S}-\boldsymbol{r_1})\cdot\boldsymbol{s}}e^{\frac{-im}{\hbar t}(\boldsymbol{U}-\boldsymbol{r_2})\cdot\boldsymbol{u}}\\ &\times\left\langle\hat{\boldsymbol{\Psi}}^\dagger(\boldsymbol{S}+\frac{\boldsymbol{s}}{2},0)\hat{\boldsymbol{\Psi}}^\dagger(\boldsymbol{U}+\frac{\boldsymbol{u}}{2},0)\hat{\boldsymbol{\Psi}}(\boldsymbol{S}-\frac{\boldsymbol{s}}{2},0)\hat{\boldsymbol{\Psi}}(\boldsymbol{U}-\frac{\boldsymbol{u}}{2},0)\right\rangle,\end{aligned} \tag{A.7}$$

where the superscript 3D, is to indicate that $g_2^{3\mathrm{D}}$ is a function of 3D spatial coordinates, as opposed to the $g_2(\boldsymbol{r})$ (introduced in Eq. A.15) extracted experimentally from the images of short TOF density noise which is a function of 2D spatial coordinates. Doing another centre-of-mass transform, introducing relative distance $\boldsymbol{r}_{12} = \boldsymbol{r}_1 - \boldsymbol{r}_2$ and the centre-of-mass coordinate $\boldsymbol{R}_{12} = 1/2(\boldsymbol{r}_1+\boldsymbol{r}_2)$

$$\begin{aligned}g_2^{3\mathrm{D}}(\boldsymbol{r}_1,\boldsymbol{r}_2,t) =& \frac{A^6}{n_0^2}\int d^3\boldsymbol{s}\int d^3\boldsymbol{S}\int d^3\boldsymbol{u}\int d^3\boldsymbol{U} e^{\frac{-im}{\hbar t}\left[(\boldsymbol{S}-\frac{\boldsymbol{r}_{12}}{2})\cdot\boldsymbol{s}+(\boldsymbol{U}+\frac{\boldsymbol{r}_{12}}{2})\cdot\boldsymbol{u}-\boldsymbol{R}_{12}\cdot(\boldsymbol{s}+\boldsymbol{u})\right]}\\ &\times\left\langle\hat{\boldsymbol{\Psi}}^\dagger(\boldsymbol{S}+\frac{\boldsymbol{s}}{2},0)\hat{\boldsymbol{\Psi}}^\dagger(\boldsymbol{U}+\frac{\boldsymbol{u}}{2},0)\hat{\boldsymbol{\Psi}}(\boldsymbol{S}-\frac{\boldsymbol{s}}{2},0)\hat{\boldsymbol{\Psi}}(\boldsymbol{U}-\frac{\boldsymbol{u}}{2},0)\right\rangle.\end{aligned} \tag{A.8}$$

We separate the spatial coordinates into the components parallel to the xy-plane $\boldsymbol{R}_\parallel$ and perpendicular to it $R_\perp$ (i.e. in the z direction). Explicitly writing the in-plane and out-of-plane dependence of the initial position representation of the Bose operators as $\hat{\boldsymbol{\Psi}}_0(\boldsymbol{r}_\parallel, r_\perp)$, Eq. A.8 can be rewritten as

$$\begin{aligned} g_2^{\mathrm{3D}}(\boldsymbol{r}_1,\boldsymbol{r}_2,t) =& \frac{A^6}{n_0^2}\int d^2\boldsymbol{s}_\parallel \int ds_\perp \int d^2\boldsymbol{S}_\parallel \int dS_\perp \int d^2\boldsymbol{u}_\parallel \int du_\perp \int d^2\boldsymbol{U}_\parallel \int dU_\perp \\ &\times e^{\frac{-im}{\hbar t}\left[(\boldsymbol{S}_\parallel - \frac{\boldsymbol{r}_{\parallel 12}}{2})\cdot\boldsymbol{s}_\parallel + (\boldsymbol{U}_\parallel + \frac{\boldsymbol{r}_{\parallel 12}}{2})\cdot\boldsymbol{u}_\parallel - \boldsymbol{R}_{\parallel 12}\cdot(\boldsymbol{s}_\parallel+\boldsymbol{u}_\parallel)\right]} \\ &\times e^{\frac{-im}{\hbar t}\left[(S_\perp - \frac{r_{\perp 12}}{2})s_\perp + (U_\perp + \frac{r_{\perp 12}}{2})u_\perp - R_{\perp 12}(s_\perp+u_\perp)\right]} \\ &\times \Big\langle \hat{\boldsymbol{\Psi}}_0^\dagger(\boldsymbol{S}_\parallel + \frac{\boldsymbol{s}_\parallel}{2}, S_\perp + \frac{s_\perp}{2})\hat{\boldsymbol{\Psi}}_0^\dagger(\boldsymbol{U}_\parallel + \frac{\boldsymbol{u}_\parallel}{2}, U_\perp + \frac{u_\perp}{2}) \\ &\hat{\boldsymbol{\Psi}}_0(\boldsymbol{S}_\parallel - \frac{\boldsymbol{s}_\parallel}{2}, S_\perp - \frac{s_\perp}{2})\hat{\boldsymbol{\Psi}}_0(\boldsymbol{U}_\parallel - \frac{\boldsymbol{u}_\parallel}{2}, U_\perp - \frac{u_\perp}{2})\Big\rangle. \end{aligned} \tag{A.9}$$

Where $\boldsymbol{r}_{\parallel 12}$ is the separation between $\boldsymbol{r}_1, \boldsymbol{r}_2$ in the xy-plane, and $r_{\perp 12}$ the separation in the z-direction. We can then follow the procedure in earlier work to simplify the in-plane component, namely noting that by integrating over $\boldsymbol{R}_{\parallel 12}$ we obtain a delta function on the RHS, and we denote the integral formally by $\int d^2\boldsymbol{R}_{\parallel 12} = B$ on the LHS. Using

$$\int d^2\boldsymbol{R}_{\parallel 12} e^{\frac{im}{\hbar t}\left[\boldsymbol{R}_{\parallel 12}\cdot(\boldsymbol{s}_\parallel+\boldsymbol{u}_\parallel)\right]} = \left(\frac{2\pi\hbar t}{m}\right)^2 \delta^2(\boldsymbol{s}_\parallel + \boldsymbol{u}_\parallel) = A^{-2}\delta^2(\boldsymbol{s}_\parallel + \boldsymbol{u}_\parallel). \tag{A.10}$$

Using this and integrating over $\boldsymbol{u}_\parallel$ sets $\boldsymbol{u}_\parallel = -\boldsymbol{s}_\parallel$, yielding

$$\begin{aligned} g_2^{\mathrm{3D}}(\boldsymbol{r}_1,\boldsymbol{r}_2,t)B =& \frac{A^4}{n_0^2}\int d^2\boldsymbol{s}_\parallel \int ds_\perp \int d^2\boldsymbol{S}_\parallel \int dS_\perp \int du_\perp \int d^2\boldsymbol{U}_\parallel \int dU_\perp \\ &\times e^{\frac{-im}{\hbar t}\left[(\boldsymbol{S}_\parallel - \boldsymbol{U}_\parallel - \boldsymbol{r}_{\parallel 12})\cdot\boldsymbol{s}_\parallel\right]} \\ &\times e^{\frac{-im}{\hbar t}\left[(S_\perp - \frac{r_{\perp 12}}{2})s_\perp + (U_\perp + \frac{r_{\perp 12}}{2})u_\perp - R_{\perp 12}(s_\perp+u_\perp)\right]} \\ &\times \Big\langle \hat{\boldsymbol{\Psi}}_0^\dagger(\boldsymbol{S}_\parallel + \frac{\boldsymbol{s}_\parallel}{2}, S_\perp + \frac{s_\perp}{2})\hat{\boldsymbol{\Psi}}_0^\dagger(\boldsymbol{U}_\parallel - \frac{\boldsymbol{s}_\parallel}{2}, U_\perp + \frac{u_\perp}{2}) \\ &\hat{\boldsymbol{\Psi}}_0(\boldsymbol{S}_\parallel - \frac{\boldsymbol{s}_\parallel}{2}, S_\perp - \frac{s_\perp}{2})\hat{\boldsymbol{\Psi}}_0(\boldsymbol{U}_\parallel + \frac{\boldsymbol{s}_\parallel}{2}, U_\perp - \frac{u_\perp}{2})\Big\rangle. \end{aligned} \tag{A.11}$$

As in Seigl's thesis we perform a centre-of-mass transformation to exploit the in-plane translational invariance of the wavefunctions [54]. Introducing $\boldsymbol{x} = \boldsymbol{S}_\parallel - \boldsymbol{U}_\parallel$, $\boldsymbol{X} =$

$\boldsymbol{S}_\parallel + \boldsymbol{U}_\parallel$, the Jacobian determinant for this transformation introduces a factor of 1/2.

$$\begin{aligned} g_2^{\mathrm{3D}}(\boldsymbol{r}_1,\boldsymbol{r}_2,t)B =& \frac{A^4}{2n_0^2}\int d^2\boldsymbol{s}_\parallel \int ds_\perp \int d^2\boldsymbol{x} \int dS_\perp \int du_\perp \int d^2\boldsymbol{X} \int dU_\perp \\ & \times e^{\frac{-im}{\hbar t}\left[(\boldsymbol{x}-\boldsymbol{r}_{\parallel 12})\cdot \boldsymbol{s}_\parallel\right]} \\ & \times e^{\frac{-im}{\hbar t}\left[(S_\perp - \frac{r_{\perp 12}}{2})s_\perp + (U_\perp + \frac{r_{\perp 12}}{2})u_\perp - R_{\perp 12}(s_\perp + u_\perp)\right]} \\ & \times \Big\langle \hat{\boldsymbol{\Psi}}_0^\dagger(\boldsymbol{X} + \frac{\boldsymbol{x}+\boldsymbol{s}_\parallel}{2}, S_\perp + \frac{s_\perp}{2})\hat{\boldsymbol{\Psi}}_0^\dagger(\boldsymbol{X} - \frac{\boldsymbol{x}+\boldsymbol{s}_\parallel}{2}, U_\perp + \frac{u_\perp}{2}) \\ & \hat{\boldsymbol{\Psi}}_0(\boldsymbol{X} + \frac{\boldsymbol{x}-\boldsymbol{s}_\parallel}{2}, S_\perp - \frac{s_\perp}{2})\hat{\boldsymbol{\Psi}}_0(\boldsymbol{X} - \frac{\boldsymbol{x}-\boldsymbol{s}_\parallel}{2}, U_\perp - \frac{u_\perp}{2})\Big\rangle. \end{aligned} \tag{A.12}$$

This allows us to exploit the in-plane translational invariance of the wavefunction, i.e that $\hat{\boldsymbol{\Psi}}_0(\boldsymbol{d}+\boldsymbol{r}_\parallel, r_\perp) = \hat{\boldsymbol{\Psi}}_0(\boldsymbol{r}_\parallel, r_\perp)$. This allows us to evaluate the integral over $\boldsymbol{X}$, picking up a factor of B on the RHS. This leaves

$$\begin{aligned} g_2^{\mathrm{3D}}(\boldsymbol{r}_1,\boldsymbol{r}_2,t)B =& \frac{A^4}{2n_0^2}B\int d^2\boldsymbol{s}_\parallel \int ds_\perp \int d^2\boldsymbol{x} \int dS_\perp \int du_\perp \int dU_\perp \\ & \times e^{\frac{-im}{\hbar t}\left[(\boldsymbol{x}-\boldsymbol{r}_{\parallel 12})\cdot \boldsymbol{s}_\parallel\right]} \\ & \times e^{\frac{-im}{\hbar t}\left[(S_\perp - \frac{r_{\perp 12}}{2})s_\perp + (U_\perp + \frac{r_{\perp 12}}{2})u_\perp - R_{\perp 12}(s_\perp + u_\perp)\right]} \\ & \times \Big\langle \hat{\boldsymbol{\Psi}}_0^\dagger(\frac{\boldsymbol{x}+\boldsymbol{s}_\parallel}{2}, S_\perp + \frac{s_\perp}{2})\hat{\boldsymbol{\Psi}}_0^\dagger(-\frac{\boldsymbol{x}+\boldsymbol{s}_\parallel}{2}, U_\perp + \frac{u_\perp}{2}) \\ & \hat{\boldsymbol{\Psi}}_0(\frac{\boldsymbol{x}-\boldsymbol{s}_\parallel}{2}, S_\perp - \frac{s_\perp}{2})\hat{\boldsymbol{\Psi}}_0(-\frac{\boldsymbol{x}-\boldsymbol{s}_\parallel}{2}, U_\perp - \frac{u_\perp}{2})\Big\rangle. \end{aligned} \tag{A.13}$$

The final change of variables, $\boldsymbol{r}' = \boldsymbol{x} - \boldsymbol{s}_\parallel$, $\boldsymbol{r} = \boldsymbol{x} + \boldsymbol{s}_\parallel$ introduces another 1/2 prefactor but simplifies the arguments of the wavefunctions as

$$\begin{aligned} g_2^{\mathrm{3D}}(\boldsymbol{r}_1,\boldsymbol{r}_2,t) =& \frac{A^4}{4n_0^2}\int d^2\boldsymbol{r} \int d^2\boldsymbol{r}' \int ds_\perp \int dS_\perp \int du_\perp \int dU_\perp \\ & \times e^{\frac{-im}{4\hbar t}\left[\boldsymbol{r}^2 - \boldsymbol{r}'^2 - 2\boldsymbol{r}_{\parallel 12}\cdot(\boldsymbol{r}-\boldsymbol{r}')\right]} \\ & \times e^{\frac{-im}{\hbar t}\left[(S_\perp - \frac{r_{\perp 12}}{2})s_\perp + (U_\perp + \frac{r_{\perp 12}}{2})u_\perp - R_{\perp 12}(s_\perp + u_\perp)\right]} \\ & \times \Big\langle \hat{\boldsymbol{\Psi}}_0^\dagger(\frac{\boldsymbol{r}}{2}, S_\perp + \frac{s_\perp}{2})\hat{\boldsymbol{\Psi}}_0^\dagger(-\frac{\boldsymbol{r}}{2}, U_\perp + \frac{u_\perp}{2}) \\ & \hat{\boldsymbol{\Psi}}_0(\frac{\boldsymbol{r}'}{2}, S_\perp - \frac{s_\perp}{2})\hat{\boldsymbol{\Psi}}_0(-\frac{\boldsymbol{r}'}{2}, U_\perp - \frac{u_\perp}{2})\Big\rangle. \end{aligned} \tag{A.14}$$

Now that we have simplified the in-plane components as much as possible we turn our attention to the out of plane components.

A.0.1 Simplifying Out-of-plane Components

With the vertical imaging in our experimental setup we expect to sample g_2 integrated along the z direction (see [47] supplemental material section B.4) we denote this by

$$g_2(\boldsymbol{r}_{1,2D}, \boldsymbol{r}_{2,2D}) = \int dr_{1z} \int dr_{2z} g_2^{3D}(\boldsymbol{r}_{1,3D}, \boldsymbol{r}_{2,3D}). \tag{A.15}$$

This gives

$$\begin{aligned} g_2(\boldsymbol{r}_{1,2D}, \boldsymbol{r}_{2,2D}) =& \frac{A^4}{4n_0^2} \int dr_{\perp 12} \int dR_{\perp 12} \int d^2\boldsymbol{r} \int d^2\boldsymbol{r}' \int ds_\perp \int dS_\perp \int du_\perp \int dU_\perp \\ & \times e^{\frac{-im}{4\hbar t}\left[\boldsymbol{r}^2 - \boldsymbol{r}'^2 - 2\boldsymbol{r}_{\parallel 12}\cdot(\boldsymbol{r}-\boldsymbol{r}')\right]} \\ & \times e^{\frac{-im}{\hbar t}\left[(S_\perp)s_\perp + (U_\perp)u_\perp - \frac{r_{\perp 12}}{2}(s_\perp - u_\perp) - R_{\perp 12}(s_\perp + u_\perp)\right]} \\ & \times \Big\langle \hat{\boldsymbol{\Psi}}_0^\dagger(\frac{\boldsymbol{r}}{2}, S_\perp + \frac{s_\perp}{2}) \hat{\boldsymbol{\Psi}}_0^\dagger(-\frac{\boldsymbol{r}}{2}, U_\perp + \frac{u_\perp}{2}) \\ & \hat{\boldsymbol{\Psi}}_0(\frac{\boldsymbol{r}'}{2}, S_\perp - \frac{s_\perp}{2}) \hat{\boldsymbol{\Psi}}_0(-\frac{\boldsymbol{r}'}{2}, U_\perp - \frac{u_\perp}{2}) \Big\rangle. \end{aligned} \tag{A.16}$$

Where we note that this gives two Dirac delta functions for $s_\perp$ and $u_\perp$, similar to in Eq. A.10 i.e.

$$\int dR_{\perp 12} e^{\frac{im}{\hbar t}[R_{\perp 12}((s_\perp + u_\perp))]} = \left(\frac{2\pi\hbar t}{m}\right)\delta(s_\perp + u_\perp) = A^{-1}\delta(s_\perp + u_\perp), \tag{A.17}$$

and

$$\int dr_{\perp 12} e^{\frac{im}{2\hbar t}[r_{\perp 12}((s_\perp - u_\perp))]} = \left(\frac{4\pi\hbar t}{m}\right)\delta(s_\perp - u_\perp) = 2A^{-1}\delta(s_\perp - u_\perp). \tag{A.18}$$

Substituting this in

$$\begin{aligned} g_2(\boldsymbol{r}_{1,2D}, \boldsymbol{r}_{2,2D}) =& \frac{A^2}{2n_0^2} \int d^2\boldsymbol{r} \int d^2\boldsymbol{r}' \int ds_\perp \int dS_\perp \int du_\perp \int dU_\perp \\ & \times e^{\frac{-im}{4\hbar t}\left[\boldsymbol{r}^2 - \boldsymbol{r}'^2 - 2\boldsymbol{r}_{\parallel 12}\cdot(\boldsymbol{r}-\boldsymbol{r}')\right]} \\ & \times \delta(s_\perp + u_\perp)\delta(s_\perp - u_\perp) e^{\frac{-im}{\hbar t}[(S_\perp)s_\perp + (U_\perp)u_\perp]} \\ & \times \Big\langle \hat{\boldsymbol{\Psi}}_0^\dagger(\frac{\boldsymbol{r}}{2}, S_\perp + \frac{s_\perp}{2}) \hat{\boldsymbol{\Psi}}_0^\dagger(-\frac{\boldsymbol{r}}{2}, U_\perp + \frac{u_\perp}{2}) \\ & \hat{\boldsymbol{\Psi}}_0(\frac{\boldsymbol{r}'}{2}, S_\perp - \frac{s_\perp}{2}) \hat{\boldsymbol{\Psi}}_0(-\frac{\boldsymbol{r}'}{2}, U_\perp - \frac{u_\perp}{2}) \Big\rangle. \end{aligned} \tag{A.19}$$

Where the integrations have the effect of first setting $s_\perp = -u_\perp$ and then using $\delta(ax) = |a|^{-1}\delta(x)$ this has the effect of setting $s_\perp = u_\perp = 0$ and introducing a 1/2 prefactor leaving

$$\begin{aligned} g_2(\boldsymbol{r}, \boldsymbol{r}_{2,2D}) =& \frac{A^2}{4n_0^2} \int d^2\boldsymbol{r} \int d^2\boldsymbol{r}' \int dS_\perp \int dU_\perp \\ & \times e^{\frac{-im}{4\hbar t}\left[\boldsymbol{r}^2 - \boldsymbol{r}'^2 - 2\boldsymbol{r}_{\parallel 12}\cdot(\boldsymbol{r}-\boldsymbol{r}')\right]} \\ & \times \left\langle \hat{\boldsymbol{\Psi}}_0^\dagger(\frac{\boldsymbol{r}}{2}, S_\perp)\hat{\boldsymbol{\Psi}}_0^\dagger(-\frac{\boldsymbol{r}}{2}, U_\perp)\hat{\boldsymbol{\Psi}}_0(\frac{\boldsymbol{r}'}{2}, S_\perp)\hat{\boldsymbol{\Psi}}_0(-\frac{\boldsymbol{r}'}{2}, U_\perp)\right\rangle. \end{aligned} \tag{A.20}$$

We now reintroduce the original z spatial variables as $S_\perp = 1/2(z_1 + z_2)$, $s_\perp = z_1 - z_2$ and $U_\perp = 1/2(z_3 + z_4)$, $u_\perp = z_3 - z_4$. Where from the above delta functions we are left with $S_\perp = z_1$, $U_\perp = z_3$

$$\begin{aligned} g_2(\boldsymbol{r}_{1,2D}, \boldsymbol{r}_{2,2D}) =& \frac{A^2}{4n_0^2} \int d^2\boldsymbol{r} \int d^2\boldsymbol{r}' \int dz_1 \int dz_3 \\ & \times e^{\frac{-im}{4\hbar t}\left[\boldsymbol{r}^2 - \boldsymbol{r}'^2 - 2\boldsymbol{r}_{\parallel 12}\cdot(\boldsymbol{r}-\boldsymbol{r}')\right]} \\ & \times \left\langle \hat{\boldsymbol{\Psi}}_0^\dagger(\frac{\boldsymbol{r}}{2}, z_1)\hat{\boldsymbol{\Psi}}_0^\dagger(-\frac{\boldsymbol{r}}{2}, z_3)\hat{\boldsymbol{\Psi}}_0(\frac{\boldsymbol{r}'}{2}, z_1)\hat{\boldsymbol{\Psi}}_0(-\frac{\boldsymbol{r}'}{2}, z_3)\right\rangle. \end{aligned} \tag{A.21}$$

As the bosons are initially spatially confined in 2 2D condensates, located at $z = \pm d$ we take the initial 3D wavefunction to be of the form

$$\hat{\boldsymbol{\Psi}}_0(\boldsymbol{r}, z) = [\hat{\boldsymbol{\Psi}}_1(\boldsymbol{r})\delta(d - z) + \hat{\boldsymbol{\Psi}}_2(\boldsymbol{r})\delta(-d - z)]/\sqrt{2}, \tag{A.22}$$

where $\hat{\boldsymbol{\Psi}}_{1,2}(\boldsymbol{r})$ are the 2D wavefunctions corresponding to the macroscopic wavefunction in layer 1 or 2 respectively. Note that while the above assumes the particles are in a coherent superposition the outcome of any interference experiment between independent BECs can be modelled as the particles being in a superposition with a random global phase difference between the macroscopic wave functions, the above does therefore not limit the generality of the following calculations. To simplify the notation we introduce

$$\rho_{ijkl}(\boldsymbol{r}, \boldsymbol{r}') = \left\langle \hat{\boldsymbol{\Psi}}_i^\dagger(\frac{\boldsymbol{r}}{2})\hat{\boldsymbol{\Psi}}_j^\dagger(-\frac{\boldsymbol{r}}{2})\hat{\boldsymbol{\Psi}}_k(\frac{\boldsymbol{r}'}{2})\hat{\boldsymbol{\Psi}}_l(-\frac{\boldsymbol{r}'}{2})\right\rangle. \tag{A.23}$$

Substituting Eq. A.22 into Eq. A.21 we see that

$$\begin{aligned} g_2(\boldsymbol{r}_{1,2D},\boldsymbol{r}_{2,2D}) =& \frac{A^2}{4n_0^2}\int d^2\boldsymbol{r}\int d^2\boldsymbol{r}' \\ & \times e^{\frac{-im}{4\hbar t}\left[\boldsymbol{r}^2-\boldsymbol{r}'^2-2\boldsymbol{r}_{\parallel 12}\cdot(\boldsymbol{r}-\boldsymbol{r}')\right]} \\ & \times \frac{1}{4}\Big[\rho_{1111}(\boldsymbol{r},\boldsymbol{r}')+\rho_{2121}(\boldsymbol{r},\boldsymbol{r}')+\rho_{1212}(\boldsymbol{r},\boldsymbol{r}')+\rho_{2222}(\boldsymbol{r},\boldsymbol{r}')\Big]. \end{aligned} \tag{A.24}$$

Now we assume that density fluctuations are negligible and following the derivation for a single layer we make the assumption that [53]

$$\begin{aligned} \rho_{ijkl}(\boldsymbol{r},\boldsymbol{r}') \sim& n_0^2\left\langle e^{i[\theta_i(\boldsymbol{r}/2)+\theta_j(-\boldsymbol{r}/2)-\theta_k(\boldsymbol{r}'/2)-\theta_l(-\boldsymbol{r}'/2)]}\right\rangle \\ =& n_0^2 e^{\frac{1}{2}\left\langle[\theta_i(\boldsymbol{r}/2)+\theta_j(-\boldsymbol{r}/2)-\theta_k(\boldsymbol{r}'/2)-\theta_l(-\boldsymbol{r}'/2)]^2\right\rangle}. \end{aligned} \tag{A.25}$$

Further we introduce the common phase $\varphi(\boldsymbol{r}) = (\theta_1(\boldsymbol{r})+\theta_2(\boldsymbol{r}))/2$ and the relative phase $\theta(\boldsymbol{r}) = (\theta_1(\boldsymbol{r})-\theta_2(\boldsymbol{r}))/2$. Since the clouds are uncoupled they are independent variables, the expectation value can thus be factored into common and relative parts. Expanding the density-density matrices we see that

$$\begin{aligned} \rho_{1111}(\boldsymbol{r},\boldsymbol{r}') =& n_0^2\left\langle e^{i[\varphi(\boldsymbol{r}/2)+\theta(\boldsymbol{r}/2)+\varphi(-\boldsymbol{r}/2)+\theta(-\boldsymbol{r}/2)-\varphi(\boldsymbol{r}'/2)-\theta(\boldsymbol{r}'/2)-\varphi(-\boldsymbol{r}'/2)-\theta(-\boldsymbol{r}'/2)]}\right\rangle \\ =& \rho_\varphi(\boldsymbol{r},\boldsymbol{r}')\left\langle e^{i[\theta(\boldsymbol{r}/2)+\theta(-\boldsymbol{r}/2)-\theta(\boldsymbol{r}'/2)-\theta(-\boldsymbol{r}'/2)]}\right\rangle = \rho_\varphi(\boldsymbol{r},\boldsymbol{r}')\rho_\theta(\boldsymbol{r},\boldsymbol{r}') \end{aligned} \tag{A.26}$$

$$\begin{aligned} \rho_{2121}(\boldsymbol{r},\boldsymbol{r}') =& n_0^2\left\langle e^{i[\varphi(\boldsymbol{r}/2)-\theta(\boldsymbol{r}/2)+\varphi(-\boldsymbol{r}/2)+\theta(-\boldsymbol{r}/2)-\varphi(\boldsymbol{r}'/2)+\theta(\boldsymbol{r}'/2)-\varphi(-\boldsymbol{r}'/2)-\theta(-\boldsymbol{r}'/2)]}\right\rangle \\ =& \rho_\varphi(\boldsymbol{r},\boldsymbol{r}')\left\langle e^{i[-\theta(\boldsymbol{r}/2)+\theta(-\boldsymbol{r}/2)+\theta(\boldsymbol{r}'/2)-\theta(-\boldsymbol{r}'/2)]}\right\rangle \end{aligned} \tag{A.27}$$

$$\begin{aligned} \rho_{1212}(\boldsymbol{r},\boldsymbol{r}') =& n_0^2\left\langle e^{i[\varphi(\boldsymbol{r}/2)+\theta(\boldsymbol{r}/2)+\varphi(-\boldsymbol{r}/2)-\theta(-\boldsymbol{r}/2)-\varphi(\boldsymbol{r}'/2)-\theta(\boldsymbol{r}'/2)-\varphi(-\boldsymbol{r}'/2)+\theta(-\boldsymbol{r}'/2)]}\right\rangle \\ =& \rho_\varphi(\boldsymbol{r},\boldsymbol{r}')\left\langle e^{i[\theta(\boldsymbol{r}/2)-\theta(-\boldsymbol{r}/2)-\theta(\boldsymbol{r}'/2)+\theta(-\boldsymbol{r}'/2)]}\right\rangle \end{aligned} \tag{A.28}$$

$$\begin{aligned} \rho_{2222}(\boldsymbol{r},\boldsymbol{r}') =& n_0^2\left\langle e^{i[\varphi(\boldsymbol{r}/2)-\theta(\boldsymbol{r}/2)+\varphi(-\boldsymbol{r}/2)-\theta(-\boldsymbol{r}/2)-\varphi(\boldsymbol{r}'/2)+\theta(\boldsymbol{r}'/2)-\varphi(-\boldsymbol{r}'/2)+\theta(-\boldsymbol{r}'/2)]}\right\rangle \\ =& \rho_\varphi(\boldsymbol{r},\boldsymbol{r}')\left\langle e^{i[-\theta(\boldsymbol{r}/2)-\theta(-\boldsymbol{r}/2)+\theta(\boldsymbol{r}'/2)+\theta(-\boldsymbol{r}'/2)]}\right\rangle = \rho_\varphi(\boldsymbol{r},\boldsymbol{r}')\rho_\theta(\boldsymbol{r}',\boldsymbol{r}) \end{aligned} \tag{A.29}$$

Where we defined $\rho_\varphi(\boldsymbol{r},\boldsymbol{r}') = n_0^2\left\langle e^{i[\varphi(\boldsymbol{r}/2)+\varphi(-\boldsymbol{r}/2)-\varphi(\boldsymbol{r}'/2)-\varphi(-\boldsymbol{r}'/2)]}\right\rangle$, and $\rho_\theta(\boldsymbol{r},\boldsymbol{r}') = \left\langle e^{i[\theta(\boldsymbol{r}/2)+\theta(-\boldsymbol{r}/2)-\theta(\boldsymbol{r}'/2)-\theta(-\boldsymbol{r}'/2)]}\right\rangle$. Note that the signs of the exponents are opposite for $\rho_{2222}(\boldsymbol{r},\boldsymbol{r}')$ and $\rho_{1111}(\boldsymbol{r},\boldsymbol{r}')$, and also between $\rho_{2121}(\boldsymbol{r},\boldsymbol{r}')$ and $\rho_{1212}(\boldsymbol{r},\boldsymbol{r}')$. We

can therefore express the exponentials as cosines and factor

$$\begin{aligned} g_2(\boldsymbol{r}_{1,2D},\boldsymbol{r}_{2,2D}) =& \frac{A^2}{4n_0^2}\int d^2\boldsymbol{r}\int d^2\boldsymbol{r}' \\ & \times e^{\frac{-im}{4\hbar t}\left[r^2-r'^2-2\boldsymbol{r}_{\parallel 12}\cdot(\boldsymbol{r}-\boldsymbol{r}')\right]} \\ & \times \frac{1}{4}\rho_\varphi(\boldsymbol{r},\boldsymbol{r}')2\Bigg\langle\cos\Big(\theta(\boldsymbol{r}/2)+\theta(-\boldsymbol{r}/2)-\theta(\boldsymbol{r}'/2)-\theta(-\boldsymbol{r}'/2)\Big)+ \\ & \cos\Big(\theta(\boldsymbol{r}/2)-\theta(-\boldsymbol{r}/2)-\theta(\boldsymbol{r}'/2)+\theta(-\boldsymbol{r}'/2)\Big)\Bigg\rangle. \end{aligned} \tag{A.30}$$

Noting that we can apply the cosine angle addition identity

$$\begin{aligned} &\Bigg\langle\cos\Big(\theta(\frac{\boldsymbol{r}}{2})+\theta(-\frac{\boldsymbol{r}}{2})-\theta(\frac{\boldsymbol{r}'}{2})-\theta(-\frac{\boldsymbol{r}'}{2})\Big)+\cos\Big(\theta(\frac{\boldsymbol{r}}{2})-\theta(-\frac{\boldsymbol{r}}{2})-\theta(\frac{\boldsymbol{r}'}{2})+\theta(-\frac{\boldsymbol{r}'}{2})\Big)\Bigg\rangle \\ &=2\Bigg\langle\cos\Big(\theta(\boldsymbol{r}/2)-\theta(\boldsymbol{r}'/2)\Big)\cos\Big(\theta(-\boldsymbol{r}/2)-\theta(-\boldsymbol{r}'/2)\Big)\Bigg\rangle. \end{aligned} \tag{A.31}$$

Which gives

$$\begin{aligned} g_2(\boldsymbol{r}_{1,2D},\boldsymbol{r}_{2,2D}) =& \frac{A^2}{4n_0^2}\int d^2\boldsymbol{r}\int d^2\boldsymbol{r}' \\ & \times e^{\frac{-im}{4\hbar t}\left[r^2-r'^2-2\boldsymbol{r}_{\parallel 12}\cdot(\boldsymbol{r}-\boldsymbol{r}')\right]} \\ & \times \rho_\varphi(\boldsymbol{r},\boldsymbol{r}')\Big\langle\cos(\Delta\theta(\boldsymbol{r},\boldsymbol{r}'))\cos(\Delta\theta(-\boldsymbol{r},-\boldsymbol{r}'))\Big\rangle. \end{aligned} \tag{A.32}$$

where $\Delta\theta(\boldsymbol{r},\boldsymbol{r}')=\theta(\boldsymbol{r}/2)-\theta(\boldsymbol{r}'/2)$, and the average is over a thermal ensemble of phase profiles. Apart from the final term this is analogous to the case of a single layer with the common phase taking the place of the single layer phase.

A.0.2 Effect of Relative Phase

The term

$$\Big\langle\cos(\Delta\theta(\boldsymbol{r},\boldsymbol{r}'))\cos(\Delta\theta(-\boldsymbol{r},-\boldsymbol{r}'))\Big\rangle \tag{A.33}$$

encapsulates the effect of relative phase on $\tilde{g}_2$. Rewriting this using exponentials, introducing the shorthand $\Delta\theta(\pm)=\Delta\theta(\pm\boldsymbol{r},\pm\boldsymbol{r}')$, gives

$$\begin{aligned} &\Big\langle\cos(\Delta\theta(+))\cos(\Delta\theta(-))\Big\rangle = \\ &\frac{1}{4}\Big\langle e^{i[\Delta\theta(+)+\Delta\theta(-)]}+e^{i[\Delta\theta(+)-\Delta\theta(-)]}+e^{i[-\Delta\theta(+)+\Delta\theta(-)]}+e^{i[-\Delta\theta(+)-\Delta\theta(-)]}\Big\rangle \end{aligned} \tag{A.34}$$

Assuming Gaussian phase fluctuations we know that

$$\left\langle e^{i[\theta(r)+\theta(r')]}\right\rangle = e^{-\frac{1}{2}\left\langle[\theta(r)+\theta(r')]^2\right\rangle}. \tag{A.35}$$

We also know that by definition $e^{-\frac{1}{2}\left\langle\Delta\theta(\pm)^2\right\rangle} = g_{1\theta}(|\boldsymbol{r}-\boldsymbol{r}'|/2)$ (the factor 1/2 comes from the definition of $\Delta\theta(\pm)$). Applying Eq. A.35 to each term in Eq. A.34 individually and expanding the exponents we can identify

$$\left\langle e^{i[\Delta\theta(+)\pm\Delta\theta(-)]}\right\rangle = e^{-\frac{1}{2}\left\langle\Delta\theta(+)^2\right\rangle\pm\langle\Delta\theta(-)\Delta\theta(+)\rangle-\frac{1}{2}\left\langle\Delta\theta(-)^2\right\rangle} = g_{1\theta}(|\boldsymbol{r}-\boldsymbol{r}'|/2)^2 e^{\pm\langle\Delta\theta(-)\Delta\theta(+)\rangle} \tag{A.36}$$

Thus Eq. A.34 becomes

$$\left\langle\cos(\Delta\theta(+))\cos(\Delta\theta(-))\right\rangle = g_{1\theta}(|\boldsymbol{r}-\boldsymbol{r}'|/2)^2\cosh(\langle\Delta\theta(-)\Delta\theta(+)\rangle). \tag{A.37}$$

Now for the term $\langle\Delta\theta(-)\Delta\theta(+)\rangle$, we know that when $\boldsymbol{r}=\boldsymbol{r}'$ it is zero, and further at large distances i.e $\boldsymbol{r}\gg\boldsymbol{r}'$ it should also tend to zero due to the lack of true long range order due to the Mermin-Wagner theorem. We thus consider the case when the argument of cosh is small

$$\left\langle\cos(\Delta\theta(+))\cos(\Delta\theta(-))\right\rangle = g_{1\theta}(|\boldsymbol{r}-\boldsymbol{r}'|/2)^2(1+\frac{1}{2}\langle\Delta\theta(-)\Delta\theta(+)\rangle^2+O(\langle\Delta\theta(-)\Delta\theta(+)\rangle^4)) \tag{A.38}$$

so, to linear order in $\langle\Delta\theta(-)\Delta\theta(+)\rangle$, we can approximate

$$\left\langle\cos(\Delta\theta(+))\cos(\Delta\theta(-))\right\rangle \approx g_{1\theta}(|\boldsymbol{r}-\boldsymbol{r}'|/2)^2. \tag{A.39}$$

To validate this assumption we estimated $\left\langle\cos(\Delta\theta(+))\cos(\Delta\theta(-))\right\rangle$ using simulation data. Simulating 7000 relative phase profiles in the quasi-long-range ordered regime using an Ornstein-Uhlenbeck process [48, 51], as well as comparing to 500 relative phase profiles obtained with Monte Carlo, in the superfluid and normal phase. As seen in Fig. A.1 and Fig. A.2 Eq. A.39 appears to be a suitable approximation for the effect of relative phase.

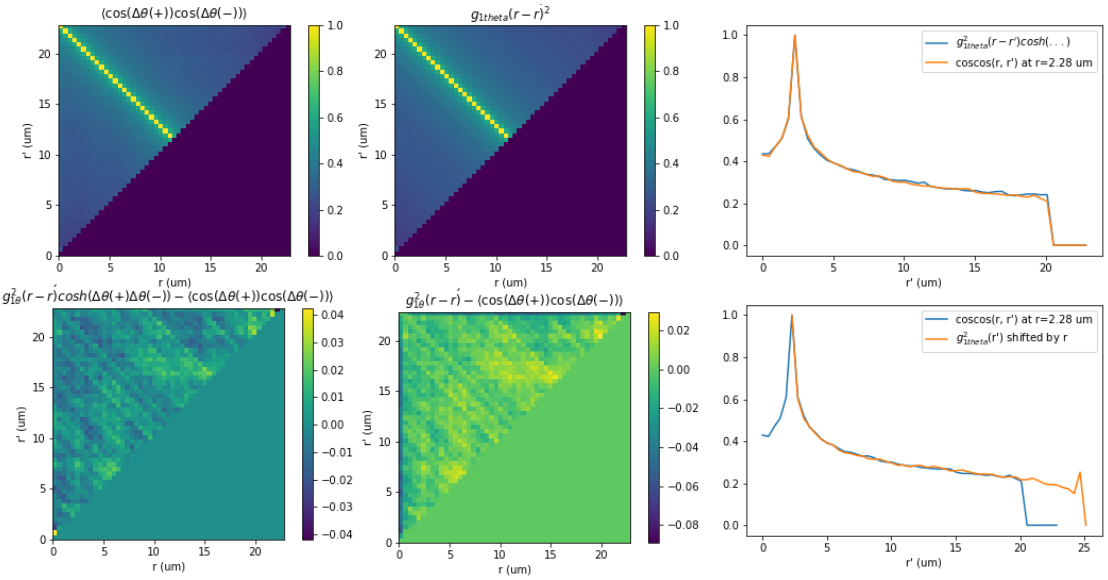


Figure A.1: The term in Eq. A.33, approximations in Eq. A.37 and Eq. A.39 evaluated and compared for 7000 relative phase profiles in the superfluid regime.

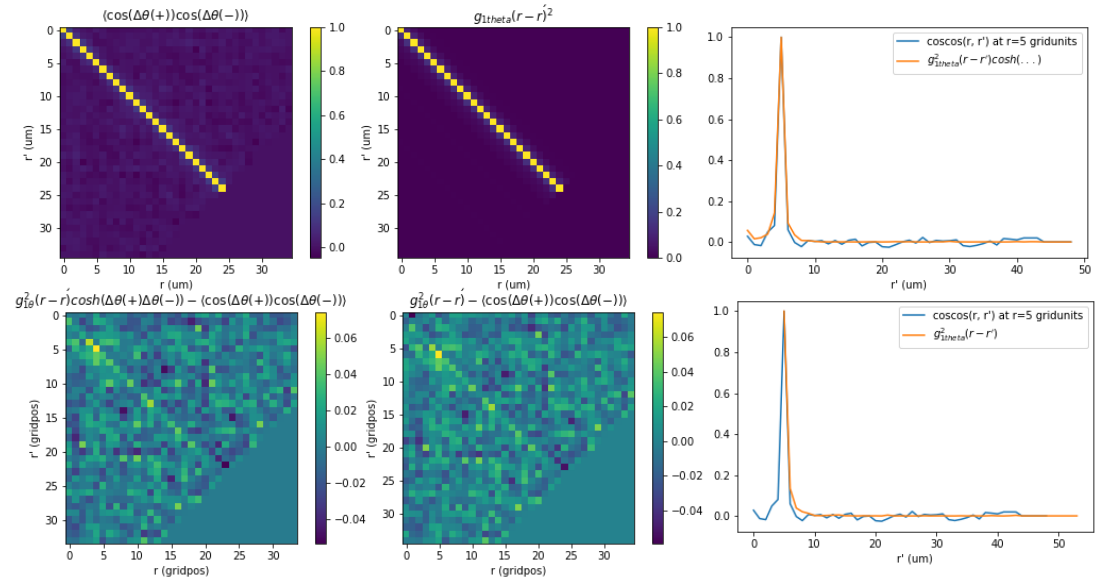


Figure A.2: The term in Eq. A.33, approximations in Eq. A.37 and Eq. A.39 evaluated and compared for 500 relative phase profiles from Monte Carlo simulations in the normal regime.

This leaves the approximate form

$$g_2(\boldsymbol{r}_{1,2D}, \boldsymbol{r}_{2,2D}) \approx \frac{A^2}{4n_0^2} \int d^2\boldsymbol{r} \int d^2\boldsymbol{r}' \times e^{\frac{-im}{4\hbar t}\left[\boldsymbol{r}^2 - \boldsymbol{r}'^2 - 2\boldsymbol{r}_{\parallel 12}\cdot(\boldsymbol{r}-\boldsymbol{r}')\right]} \times \rho_\varphi(\boldsymbol{r}, \boldsymbol{r}') g_{1\theta}(|\boldsymbol{r} - \boldsymbol{r}'|/2)^2. \tag{A.40}$$

A.0.3 Change of Integration Variables

Note that the exponential in Eq. A.40 can be expressed using new variables to more closely match the expression obtained for the single layer density noise patterns

$$\frac{m}{4\hbar t}\left[\boldsymbol{r}^2-\boldsymbol{r}'^2-2\boldsymbol{r}_{\parallel 12}\cdot(\boldsymbol{r}-\boldsymbol{r}')\right]=\frac{m}{2\hbar t}\left[(\boldsymbol{r}-\boldsymbol{r}')\cdot\boldsymbol{r}_{\parallel 12}+(\boldsymbol{r}-\boldsymbol{r}')\cdot(\boldsymbol{r}+\boldsymbol{r}')/2\right]=\boldsymbol{q}\cdot\boldsymbol{r}_{\parallel 12}+\boldsymbol{q}\cdot\boldsymbol{R}. \tag{A.41}$$

Where $\boldsymbol{q}=(m/2\hbar t)(\boldsymbol{r}-\boldsymbol{r}')$, $\boldsymbol{R}=(\boldsymbol{r}+\boldsymbol{r}')/2$ and like before $\boldsymbol{r}_{\parallel 12}=\boldsymbol{r}_{1,2D}-\boldsymbol{r}_{2,2D}$. In terms of the original variables this is $\boldsymbol{r}=\boldsymbol{R}+C\boldsymbol{q}$, $\boldsymbol{r}'=\boldsymbol{R}-C\boldsymbol{q}$ where $C=(\hbar t/m)$. The Jacobian associated with this transformation is

$$\begin{aligned}\boldsymbol{J}(q_x,q_y,R_x,R_y)&=\begin{bmatrix}\partial x/\partial q_x & \partial x/\partial q_y & \partial x/\partial R_x & \partial x/\partial R_y\\ \partial y/\partial q_x & \partial y/\partial q_y & \partial y/\partial R_x & \partial y/\partial R_y\\ \partial x'/\partial q_x & \partial x'/\partial q_y & \partial x'/\partial R_x & \partial x'/\partial R_y\\ \partial y'/\partial q_x & \partial y'/\partial q_y & \partial y'/\partial R_x & \partial y'/\partial R_y\end{bmatrix}\\&=\begin{bmatrix}C & 0 & 1 & 0\\ 0 & C & 0 & 1\\ -C & 0 & 1 & 0\\ 0 & -C & 0 & 1\end{bmatrix}.\end{aligned} \tag{A.42}$$

So the determinant associated with the coordinate transformation is $4C^2=(\frac{2\hbar t}{m})^2=A^{-2}/\pi^2$ leaving Eq. A.40 in the new variables as

$$\begin{aligned}\tilde{g}_2(\boldsymbol{r}_{\parallel 12},t)=&\frac{1}{(2\pi n_0)^2}\int d^2\boldsymbol{q}\int d^2\boldsymbol{R}\\&\times e^{-i[\boldsymbol{q}\cdot\boldsymbol{r}_{\parallel 12}+\boldsymbol{q}\cdot\boldsymbol{R}]}\\&\times\rho_\varphi(\boldsymbol{R}+\boldsymbol{q}(\hbar t/m),\boldsymbol{R}-\boldsymbol{q}(\hbar t/m))g_{1\theta}(\boldsymbol{q}\hbar t/m)^2.\end{aligned} \tag{A.43}$$

Rewriting the complex exponential using trigonometric functions we get

$$\begin{aligned}g_2(\boldsymbol{r}_{\parallel 12},t)=&\frac{1}{(2\pi n_0)^2}\int d^2\boldsymbol{q}\int d^2\boldsymbol{R}\\&\times(\cos\left(-\boldsymbol{q}\cdot\boldsymbol{r}_{\parallel 12}\right)+i\sin\left(-\boldsymbol{q}\cdot\boldsymbol{r}_{\parallel 12}\right))((\cos(-\boldsymbol{q}\cdot\boldsymbol{R})+i\sin(-\boldsymbol{q}\cdot\boldsymbol{R}))\\&\times\rho_\varphi(\boldsymbol{R}+\boldsymbol{q}(\hbar t/m),\boldsymbol{R}-\boldsymbol{q}(\hbar t/m))g_{1\theta}(\boldsymbol{q}\hbar t/m)^2.\end{aligned} \tag{A.44}$$

The terms containing sines integrate to zero as the bounds are symmetric and the other terms are invariant under a change of sign of $\boldsymbol{q}$ or $\boldsymbol{R}$, leaving

$$\begin{aligned}g_2(\boldsymbol{r}_{\parallel 12},t)=&\frac{1}{(2\pi n_0)^2}\int d^2\boldsymbol{q}\int d^2\boldsymbol{R}\\&\times\cos\left(\boldsymbol{q}\cdot\boldsymbol{r}_{\parallel 12}\right)\cos(\boldsymbol{q}\cdot\boldsymbol{R})\\&\times\rho_\varphi(\boldsymbol{R}+\boldsymbol{q}(\hbar t/m),\boldsymbol{R}-\boldsymbol{q}(\hbar t/m))g_{1\theta}(\boldsymbol{q}\hbar t/m)^2.\end{aligned} \tag{A.45}$$

To show that this agrees with the 1D result we will briefly introduce the notation from the 1D work. Introducing $\boldsymbol{q}_t = \boldsymbol{q}(\hbar t/m)$ this becomes

$$\rho_\varphi(\boldsymbol{R}+\boldsymbol{q}_t, \boldsymbol{R}-\boldsymbol{q}_t) = \left\langle \hat{\boldsymbol{\Psi}}_c^\dagger(\frac{\boldsymbol{R}+\boldsymbol{q}_t}{2})\hat{\boldsymbol{\Psi}}_c^\dagger(-\frac{\boldsymbol{R}+\boldsymbol{q}_t}{2})\hat{\boldsymbol{\Psi}}_c(\frac{\boldsymbol{R}-\boldsymbol{q}_t}{2})\hat{\boldsymbol{\Psi}}_c(-\frac{\boldsymbol{R}-\boldsymbol{q}_t}{2})\right\rangle \tag{A.46}$$

Where we use $\hat{\boldsymbol{\Psi}}_c$ referring to common excitations to mimic the notation in the 1D work. Note that we can perform a change of variables in the integral $\boldsymbol{q} \to -\boldsymbol{q}$, after which we can shift all entries in the density matrix by $(\boldsymbol{R}+\boldsymbol{q}_t)/2$. As the density matrix only depends on relative positions this leaves it invariant. The shift is to set the last entry after the coordinate transform to 0, as in the single-layer work. Finally note that the annihilation operators commute so we see that

$$\rho_\varphi(\boldsymbol{R}+\boldsymbol{q}_t, \boldsymbol{R}-\boldsymbol{q}_t) \overset{\textit{inside integral}}{=} \left\langle \hat{\boldsymbol{\Psi}}_c^\dagger(\boldsymbol{q}_t)\hat{\boldsymbol{\Psi}}_c^\dagger(\boldsymbol{R})\hat{\boldsymbol{\Psi}}_c(\boldsymbol{R}+\boldsymbol{q}_t)\hat{\boldsymbol{\Psi}}_c(0)\right\rangle \tag{A.47}$$

In agreement with the single-layer work. This is just to show that we can use the machinery with the $\mathcal{F}$ functions to reexpress the density matrix giving

$$g_2(\boldsymbol{r},t) \approx \frac{1}{(2\pi)^2}\int d^2\boldsymbol{q}\int d^2\boldsymbol{R}\cos(\boldsymbol{q}\cdot\boldsymbol{r})\cos(\boldsymbol{q}\cdot\boldsymbol{R})\frac{\mathcal{F}^{(\mathrm{com})}(\boldsymbol{q}_t)^2\mathcal{F}^{(\mathrm{com})}(\boldsymbol{R})^2}{\mathcal{F}^{(\mathrm{com})}(\boldsymbol{R}-\boldsymbol{q}_t)\mathcal{F}^{(\mathrm{com})}(\boldsymbol{R}+\boldsymbol{q}_t)}\mathcal{F}^{(\mathrm{rel})}(\boldsymbol{q}_t)^2. \tag{A.48}$$

Where $\mathcal{F}^{(\mathrm{com})}$ and $\mathcal{F}^{(\mathrm{rel})}$ are the correlation functions for the symmetric and anti-symmetric phase fluctuations in both the superfluid and normal regimes.

References

[1] S. N. Bose. "Plancks gesetz und lichtquantenhypothese". In: *Zeitschrift für Physik* 26.1 (1924), pp. 178–181.

[2] A. Einstein. "Quantentheorie des einatomigen idealen gases. zweite abhandlung". In: *Akademie-Vorträge: Sitzungsberichte der Preußischen Akademie der Wissenschaften 1914–1932* (1925), pp. 245–257.

[3] M. H. Anderson, J. R. Ensher, M. R. Matthews, C. E. Wieman, and E. A. Cornell. "Observation of Bose-Einstein condensation in a dilute atomic vapor". In: *Science* 269.5221 (1995), pp. 198–201.

[4] M. Andrews, C. Townsend, H.-J. Miesner, D. Durfee, D. Kurn, and W. Ketterle. "Observation of interference between two Bose condensates". In: *Science* 275.5300 (1997), pp. 637–641.

[5] Z. Hadzibabic, P. Krüger, M. Cheneau, B. Battelier, and J. Dalibard. "Berezinskii-Kosterlitz-Thouless crossover in a trapped atomic gas". In: *Nature* 441.7097 (June 2006), pp. 1118–1121. ISSN: 14764687.

[6] S. Sunami, V. P. Singh, D. Garrick, A. Beregi, A. J. Barker, K. Luksch, E. Bentine, L. Mathey, and C. J. Foot. "Observation of the Berezinskii-Kosterlitz-Thouless Transition in a Two-Dimensional Bose Gas via Matter-Wave Interferometry". In: *Phys. Rev. Lett.* 128 (25 June 2022), p. 250402.

[7] S. H. Simon. *Topological quantum*. Oxford University Press, 2023.

[8] Y. Cao, V. Fatemi, A. Demir, S. Fang, S. L. Tomarken, J. Y. Luo, J. D. Sanchez-Yamagishi, K. Watanabe, T. Taniguchi, E. Kaxiras, et al. "Correlated insulator behaviour at half-filling in magic-angle graphene superlattices". In: *Nature* 556.7699 (2018), pp. 80–84.

[9] G. Homann, M. H. Michael, J. G. Cosme, and L. Mathey. "Dissipationless Counterflow Currents above T_c in Bilayer Superconductors". In: *Phys. Rev. Lett.* 132 (9 Feb. 2024), p. 096002.

[10] J.-i. Okamoto, A. Cavalleri, and L. Mathey. "Theory of Enhanced Interlayer Tunneling in Optically Driven High-T_c Superconductors". In: *Phys. Rev. Lett.* 117 (22 Nov. 2016), p. 227001.

[11] S. Fava, G. De Vecchi, G. Jotzu, M. Buzzi, T. Gebert, Y. Liu, B. Keimer, and A. Cavalleri. "Magnetic field expulsion in optically driven $YBa_2Cu_3O_{6.48}$". In: *Nature* 632 (2024), p. 75.

[12] G. Bertoli, V. P. Michal, B. L. Altshuler, and G. V. Shlyapnikov. "Finite-temperature disordered bosons in two dimensions". In: *Phys. Rev. Lett.* 121.3 (2018), p. 030403.

[13] D. Garrick. "Two-dimensional Bose gases in systems with pointlike disorder". PhD thesis. University of Oxford, 2022.

[14] A. Beregi, C. Foot, and S. Sunami. "Quantum simulations with bilayer 2D Bose gases in multiple-RF-dressed potentials". In: *AVS Quantum Science* 6.3 (July 2024), p. 030501. ISSN: 2639-0213.

[15] B. Sheard. "Magnetic transport and Bose-Einstein condensation of rubidium atoms". PhD thesis. Oxford University, UK, 2010.

[16] T. Harte. "Ultracold atoms in dressed potentials". PhD thesis. University of Oxford, 2017.

[17] E. Bentine, T. L. Harte, K. Luksch, A. J. Barker, J. Mur-Petit, B. Yuen, and C. J. Foot. "Species-selective confinement of atoms dressed with multiple radiofrequencies". In: *J. Phys. B: At. Mol. Opt. Phys.* 50.9 (2017), p. 094002. ISSN: 13616455.

[18] A. Beregi. "Probing universality of 2D quantum systems with bilayer Bose gases". PhD thesis. University of Oxford, Apr. 2024.

[19] E. Bentine. "Atomic mixtures in radiofrequency dressed potentials". PhD thesis. University of Oxford, 2018.

[20] D. A. Steck. *Rubidium 87 D line data*. 2001.

[21] P. D. Lett, R. N. Watts, C. I. Westbrook, W. D. Phillips, P. L. Gould, and H. J. Metcalf. "Observation of atoms laser cooled below the Doppler limit". In: *Phys. Rev. Lett.* 61.2 (1988), p. 169.

[22] P. D. Lett, W. D. Phillips, S. Rolston, C. E. Tanner, R. Watts, and C. Westbrook. "Optical molasses". In: *J. Opt. Soc. Am. B* 6.11 (1989), pp. 2084–2107.

[23] I. Lesanovsky and W. von Klitzing. "Time-averaged adiabatic potentials: versatile matter-wave guides and atom traps". In: *Phys. Rev. Lett.* 99.8 (2007), p. 083001.

[24] M. Gildemeister, E. Nugent, B. Sherlock, M. Kubasik, B. Sheard, and C. Foot. "Trapping ultracold atoms in a time-averaged adiabatic potential". In: *Phys. Rev. A* 81.3 (2010), p. 031402.

[25] O. Zobay and B. M. Garraway. "Two-dimensional atom trapping in field-induced adiabatic potentials". In: *Phys. Rev. Lett.* 86.7 (2001), p. 1195.

[26] R. Dubessy and H. Perrin. "Quantum gases in bubble traps". In: *AVS Quantum Science* 7.1 (2025).

[27] C. J. Foot. *Atomic Physics*. Vol. 7. Oxford university press, 2005.

[28] J. Dalibard and C. Cohen-Tannoudji. "Dressed-atom approach to atomic motion in laser light: the dipole force revisited". In: *J. Opt. Soc. Am. B* 2.11 (1985), pp. 1707–1720.

[29] J. H. Shirley. "Solution of the Schrödinger equation with a Hamiltonian periodic in time". In: *Phys. Rev.* 138.4B (1965), B979.

[30] S. Stellmer, B. Pasquiou, R. Grimm, and F. Schreck. "Laser cooling to quantum degeneracy". In: *Phys. Rev. Lett.* 110.26 (2013), p. 263003.

[31] A. Urvoy, Z. Vendeiro, J. Ramette, A. Adiyatullin, and V. Vuletić. "Direct laser cooling to Bose-Einstein condensation in a dipole trap". In: *Phys. Rev. Lett.* 122.20 (2019), p. 203202.

[32] R. A. Carollo, D. C. Aveline, B. Rhyno, S. Vishveshwara, C. Lannert, J. D. Murphree, E. R. Elliott, J. R. Williams, R. J. Thompson, and N. Lundblad. "Observation of ultracold atomic bubbles in orbital microgravity". In: *Nature* 606.7913 (2022), pp. 281–286.

[33] C. Pelluet, R. Arguel, M. Rabault, V. Jarlaud, C. Metayer, B. Barrett, P. Bouyer, and B. Battelier. "Atom interferometry in an Einstein Elevator". In: *Nature Communications* 16.1 (2025), p. 4812.

[34] E. Rydow, V. P. Singh, A. Beregi, E. Chang, L. Mathey, C. J. Foot, and S. Sunami. "Observation of a bilayer superfluid with interlayer coherence". In: *Nature Communications* 16.1 (2025), p. 7201.

[35] E. Chang, V. P. Singh, A. Beregi, E. Rydow, L. Mathey, C. J. Foot, and S. Sunami. "Coupling-induced universal dynamics in bilayer two-dimensional Bose gases". In: *arXiv preprint arXiv:2510.23600* (2025).

[36] O. Morizot, C. G. Alzar, P.-E. Pottie, V. Lorent, and H. Perrin. "Trapping and cooling of rf-dressed atoms in a quadrupole magnetic field". In: *J. Phys. B: At. Mol. Opt. Phys* 40.20 (2007), p. 4013.

[37] R. K. Easwaran, L. Longchambon, P.-E. Pottie, V. Lorent, H. Perrin, and B. M. Garraway. "RF spectroscopy in a resonant RF-dressed trap". In: *J. Phys. B: At. Mol. Opt. Phys.* 43.6 (2010), p. 065302.

[38] R. Howl and I. Fuentes. "Quantum frequency interferometry: With applications ranging from gravitational wave detection to dark matter searches". In: *AVS Quantum Science* 5.1 (2023).

[39] H. A. Fernandez-Melendez, A. Belyaev, V. Gurzadyan, and I. Fuentes. "Probing lambda-gravity with Bose-Einstein condensates". In: *Phys. Rev. Res.* 7.4 (2025), p. L042051.

[40] S. Ravenhall, B. Yuen, and C. Foot. "High-flux, adjustable, compact cold-atom source". In: *Optics Express* 29.14 (2021), pp. 21143–21159.

[41] K. B. Davis, M.-O. Mewes, and W. Ketterle. "An analytical model for evaporative cooling of atoms". In: *Appl. Phys. B* 60.2 (1995), pp. 155–159.

[42] E. Surkov, J. Walraven, and G. Shlyapnikov. "Collisionless motion and evaporative cooling of atoms in magnetic traps". In: *Phys. Rev. A* 53.5 (1996), p. 3403.

[43] C. J. Pethick and H. Smith. *Bose–Einstein condensation in dilute gases*. Cambridge: Cambridge University Press, 2008. ISBN: 9780511802850.

[44] A. Polkovnikov, E. Altman, and E. Demler. "Interference between independent fluctuating condensates". In: *Proceedings of the National Academy of Sciences* 103.16 (2006), pp. 6125–6129.

[45] N. Metropolis, A. W. Rosenbluth, M. N. Rosenbluth, A. H. Teller, and E. Teller. "Equation of state calculations by fast computing machines". In: *J. Chem. Phys.* 21.6 (1953), pp. 1087–1092.

[46] W. K. Hastings. "Monte Carlo sampling methods using Markov chains and their applications". In: *Biometrika* 57.1 (1970), pp. 97–109.

[47] S. Sunami, V. P. Singh, E. Rydow, A. Beregi, E. Chang, L. Mathey, and C. J. Foot. "Detecting Phase Coherence of 2D Bose Gases via Noise Correlations". In: *Phys. Rev. Lett.* 134 (18 May 2025), p. 183407.

[48] E. Chang. "Non-equilibrium Dynamics in Coupled Bilayer Two-dimensional Bose Gases". PhD thesis. University of Oxford, Mar. 2025.

[49] S. Manz, R. Bücker, T. Betz, C. Koller, S. Hofferberth, I. E. Mazets, A. Imambekov, E. Demler, A. Perrin, J. Schmiedmayer, and T. Schumm. "Two-point density correlations of quasicondensates in free expansion". In: *Phys. Rev. A* 81 (3 Mar. 2010), p. 031610.

[50] A. Imambekov, I. E. Mazets, D. S. Petrov, V. Gritsev, S. Manz, S. Hofferberth, T. Schumm, E. Demler, and J. Schmiedmayer. "Density ripples in expanding low-dimensional gases as a probe of correlations". In: *Phys. Rev. A* 80 (3 Sept. 2009), p. 033604.

[51] I. E. Mazets. "Two-dimensional dynamics of expansion of a degenerate Bose gas". In: *Phys. Rev. A* 86 (5 Nov. 2012), p. 055603.

[52] J.-y. Choi, S. W. Seo, W. J. Kwon, and Y.-i. Shin. "Probing Phase Fluctuations in a 2D Degenerate Bose Gas by Free Expansion". In: *Phys. Rev. Lett.* 109 (12 Sept. 2012), p. 125301.

[53] V. P. Singh and L. Mathey. "Noise correlations of two-dimensional Bose gases". In: *Phys. Rev. A* 89 (5 May 2014), p. 053612.

[54] J. D. Siegl. "Probing coherence properties of strongly interacting 2D Bose gases". PhD thesis. University of Hamburg, Oct. 2018.

[55] A. Perry, S. Sugawa, F. Salces-Carcoba, Y. Yue, and I. Spielman. "Multiple-camera defocus imaging of ultracold atomic gases". In: *Optics Express* 29.11 (2021), pp. 17029–17041.

[56] T. Murtadho, F. Cataldini, S. Erne, M. Gluza, M. Tajik, J. Schmiedmayer, and N. H. Ng. "Measurement of total phase fluctuation in cold-atomic quantum simulators". In: *Phys. Rev. Res.* 7.2 (2025), p. L022031.

[57] M. Gring, M. Kuhnert, T. Langen, T. Kitagawa, B. Rauer, M. Schreitl, I. Mazets, D. A. Smith, E. Demler, and J. Schmiedmayer. "Relaxation and Prethermalization in an Isolated Quantum System". In: *Science* 337.6100 (2012), pp. 1318–1322. ISSN: 0036-8075.

[58] L. Mathey, A. Polkovnikov, and A. H. C. Neto. "Phase-locking transition of coupled low-dimensional superfluids". In: *Eur. Phys. Lett.* 81.1 (Dec. 2007), p. 10008.

[59] L. Benfatto, C. Castellani, and T. Giamarchi. "Kosterlitz-Thouless behavior in layered superconductors: The role of the vortex core energy". In: *Phys. Rev. Lett.* 98.11 (Mar. 2007), p. 117008. ISSN: 00319007.

[60] A. J. Barker, S. Sunami, D. Garrick, A. Beregi, K. Luksch, E. Bentine, and C. J. Foot. "Coherent splitting of two-dimensional Bose gases in magnetic potentials". In: *New J. Phys.* 22 (2020), p. 103040.

[61] T. Langen. "Comment on "Probing Phase Fluctuations in a 2D Degenerate Bose Gas by Free Expansion"". In: *Phys. Rev. Lett.* 111 (15 Oct. 2013), p. 159601.

[62] A. Posazhennikova. "Colloquium: Weakly interacting, dilute Bose gases in 2D". In: *Rev. Mod. Phys.* 78 (4 Oct. 2006), pp. 1111–1134.

[63] N. Prokof'ev, O. Ruebenacker, and B. Svistunov. "Critical point of a weakly interacting two-dimensional Bose gas". In: *Phys. Rev. Lett.* 87 (27 Dec. 2001), p. 270402.

[64] D. R. Nelson and J. M. Kosterlitz. "Universal Jump in the Superfluid Density of Two-Dimensional Superfluids". In: *Phys. Rev. Lett.* 39 (19 Nov. 1977), pp. 1201–1205.

[65] M. Sesodia, S. Sunami, E. Chang, E. Rydow, C. J. Foot, and A. Beregi. "CNN-Based vortex detection in atomic 2D Bose gases in the presence of a phononic background". In: *Machine Learning: Science and Technology* 6.1 (2025), p. 015067.

[66] A. Drenth, A. Huiser, and H. Ferwerda. "The problem of phase retrieval in light and electron microscopy of strong objects". In: *Optica Acta: International Journal of Optics* 22.7 (1975), pp. 615–628.

[67] A. Huiser and H. Ferwerda. "The problem of phase retrieval in light and electron microscopy of strong objects: II. On the uniqueness and stability of object reconstruction procedures using two defocused images". In: *Optica Acta: International Journal of Optics* 23.6 (1976), pp. 445–456.

[68] Y. Makhlin, G. Schön, and A. Shnirman. "Quantum-state engineering with Josephson-junction devices". In: *Rev. Mod. Phys.* 73 (2 May 2001), pp. 357–400.

[69] C. L. Degen, F. Reinhard, and P. Cappellaro. "Quantum sensing". In: *Rev. Mod. Phys.* 89 (3 July 2017), p. 035002.

[70] T. Langen, S. Erne, R. Geiger, B. Rauer, T. Schweigler, M. Kuhnert, W. Rohringer, I. E. Mazets, T. Gasenzer, and J. Schmiedmayer. "Experimental observation of a generalized Gibbs ensemble". In: *Science* 348.6231 (Apr. 2015), pp. 207–211. ISSN: 10959203.

[71] T. Schweigler, V. Kasper, S. Erne, I. Mazets, B. Rauer, F. Cataldini, T. Langen, T. Gasenzer, J. Berges, and J. Schmiedmayer. "Experimental characterization of a quantum many-body system via higher-order correlations". In: *Nature* 545.7654 (May 2017), pp. 323–326. ISSN: 14764687.

[72] V. Berezinskiĭ. "Destruction of Long-range Order in One-dimensional and Two-dimensional Systems Possessing a Continuous Symmetry Group. II. Quantum Systems". In: *Sov. Phys. JETP* 34 (1972), p. 610. ISSN: 1063-7761.

[73] J. M. Kosterlitz and D. J. Thouless. "Ordering, metastability and phase transitions in two-dimensional systems". In: *J. Phys. C Solid State Phys.* 6.7 (1973), pp. 1181–1203. ISSN: 00223719.

[74] A. J. Leggett. "What do we know about high Tc?" In: *Nature Physics* 2.3 (2006), pp. 134–136.

[75] A. Cavalleri. "Photo-induced superconductivity". In: *Contemp. Phys.* 59.1 (2018), pp. 31–46.

[76] M. Gall, N. Wurz, J. Samland, C. F. Chan, and M. Köhl. "Competing magnetic orders in a bilayer Hubbard model with ultracold atoms". In: *Nature* 589.7840 (2021), pp. 40–43.

[77] Z. Meng, L. Wang, W. Han, F. Liu, K. Wen, C. Gao, P. Wang, C. Chin, and J. Zhang. "Atomic Bose–Einstein condensate in twisted-bilayer optical lattices". In: *Nature* 615.7951 (2023), pp. 231–236.

[78] D.-W. Wang. "Quantum phase transitions of polar molecules in bilayer systems". In: *Phys. Rev. Lett.* 98.6 (2007), p. 060403.

[79] A. Macia, G. Astrakharchik, F. Mazzanti, S. Giorgini, and J. Boronat. "Single-particle versus pair superfluidity in a bilayer system of dipolar bosons". In: *Phys. Rev. A* 90.4 (2014), p. 043623.

[80] K. Kasamatsu, M. Tsubota, and M. Ueda. "Vortex Molecules in Coherently Coupled Two-Component Bose-Einstein Condensates". In: *Phys. Rev. Lett.* 93 (25 Dec. 2004), p. 250406.

[81] L. Benfatto, C. Castellani, and T. Giamarchi. "Kosterlitz-Thouless behavior in layered superconductors: The role of the vortex core energy". In: *Phys. Rev. Lett.* 98.11 (Mar. 2007), p. 117008. ISSN: 00319007.

[82] K. Furutani, A. Perali, and L. Salasnich. "Berezinskii-Kosterlitz-Thouless phase transition with Rabi-coupled bosons". In: *Phys. Rev. A* 107 (4 Apr. 2023), p. L041302.

[83] F.-F. Song and G.-M. Zhang. "Phase Coherence of Pairs of Cooper Pairs as Quasi-Long-Range Order of Half-Vortex Pairs in a Two-Dimensional Bilayer System". In: *Phys. Rev. Lett.* 128 (19 May 2022), p. 195301.

[84] M. Tylutki, L. P. Pitaevskii, A. Recati, and S. Stringari. "Confinement and precession of vortex pairs in coherently coupled Bose-Einstein condensates". In: *Phys. Rev. A* 93 (4 Apr. 2016), p. 043623.

[85] M. Eto and M. Nitta. "Confinement of half-quantized vortices in coherently coupled Bose-Einstein condensates: Simulating quark confinement in a QCD-like theory". In: *Phys. Rev. A* 97 (2 Feb. 2018), p. 023613.

[86] V. Karle, N. Defenu, and T. Enss. "Coupled superfluidity of binary Bose mixtures in two dimensions". In: *Phys. Rev. A* 99 (6 June 2019), p. 063627.

[87] G. Bighin, N. Defenu, I. Nándori, L. Salasnich, and A. Trombettoni. "Berezinskii-Kosterlitz-Thouless Paired Phase in Coupled XY Models". In: *Phys. Rev. Lett.* 123 (10 Sept. 2019), p. 100601.

[88] M. Cazalilla, A. Iucci, and T. Giamarchi. "Competition between vortex unbinding and tunneling in an optical lattice". In: *Phys. Rev. A* 75.5 (2007), p. 051603.

[89] A. Masini, A. Cuccoli, A. Rettori, A. Trombettoni, and F. Cinti. "Helicity modulus in the bilayer XY model by the Monte Carlo worm algorithm". In: *Phys. Rev. B* 111.9 (2025), p. 094415.

[90] T. Xiao, Y. Deng, and X.-Y. Dong. "Fate of the Berezinskii-Kosterlitz-Thouless paired phase in coupled XY models". In: *Phys. Rev. B* 112.14 (2025), p. 144420.

[91] R. Gati and M. K. Oberthaler. "A bosonic Josephson junction". In: *J. Phys. B: At. Mol. Opt. Phys.* 40.10 (May 2007), R61.

[92] T. Langen, T. Gasenzer, and J. Schmiedmayer. "Prethermalization and universal dynamics in near-integrable quantum systems". In: *J. Stat. Mech.* 6 (2016), p. 064009. ISSN: 17425468.

[93] S. Sunami, V. P. Singh, D. Garrick, A. Beregi, A. J. Barker, K. Luksch, E. Bentine, L. Mathey, and C. J. Foot. "Universal scaling of the dynamic BKT transition in quenched 2D Bose gases". In: *Science* 382 (6669 Oct. 2023), pp. 443–447. ISSN: 10959203.

[94] N. Navon, R. P. Smith, and Z. Hadzibabic. "Quantum gases in optical boxes". In: *Nature Physics* 17 (17 Dec. 2021), p. 1334. ISSN: 1745-2481.

[95] V. Gritsev, A. Polkovnikov, and E. Demler. "Linear response theory for a pair of coupled one-dimensional condensates of interacting atoms". In: *Phys. Rev. B* 75.17 (2007), p. 174511.

[96] K. Merloti, R. Dubessy, L. Longchambon, A. Perrin, P. E. Pottie, V. Lorent, and H. Perrin. "A two-dimensional quantum gas in a magnetic trap". In: *New J. Phys.* 15.3 (Mar. 2013), p. 033007. ISSN: 13672630.

[97] E. Altman, E. Demler, and M. D. Lukin. "Probing many-body states of ultracold atoms via noise correlations". In: *Phys. Rev. A* 70 (1 July 2004), p. 013603.

[98] L. Mathey, A. Vishwanath, and E. Altman. "Noise correlations in low-dimensional systems of ultracold atoms". In: *Phys. Rev. A* 79 (1 Jan. 2009), p. 013609.

[99] S. W. Seo, J.-y. Choi, and Y.-i. Shin. "Scaling behavior of density fluctuations in an expanding quasi-two-dimensional degenerate Bose gas". In: *Phys. Rev. A* 89 (4 Apr. 2014), p. 043606.

[100] W. H. Zurek. "Cosmological experiments in superfluid helium?" In: *Nature* 317 (1985), p. 505. ISSN: 14764687.

[101] P. Comaron, F. Larcher, F. Dalfovo, and N. P. Proukakis. "Quench dynamics of an ultracold two-dimensional Bose gas". In: *Phys. Rev. A* 100 (3 Sept. 2019), p. 033618.

[102] J. Schole, B. Nowak, and T. Gasenzer. "Critical dynamics of a two-dimensional superfluid near a nonthermal fixed point". In: *Phys. Rev. A* 86 (1 July 2012), p. 013624.

[103] P. Heinen, A. N. Mikheev, C.-M. Schmied, and T. Gasenzer. "Non-thermal fixed points of universal sine-Gordon coarsening dynamics". In: *arXiv preprint arXiv:2212.01162* (2022).

[104] P. Heinen, A. N. Mikheev, and T. Gasenzer. "Anomalous scaling at nonthermal fixed points of the sine-Gordon model". In: *Phys. Rev. A* 107.4 (2023), p. 043303.

[105] B. Zhu, V. P. Singh, J. Okamoto, and L. Mathey. "Dynamical control of the conductivity of an atomic Josephson junction". In: *Phys. Rev. Res.* 3 (1 Feb. 2021), p. 013111.

[106] A. Hu, L. Mathey, E. Tiesinga, I. Danshita, C. J. Williams, and C. W. Clark. "Detecting paired and counterflow superfluidity via dipole oscillations". In: *Phys. Rev. A* 84 (4 Oct. 2011), p. 041609.

[107] E. Bentine, A. J. Barker, K. Luksch, S. Sunami, T. L. Harte, B. Yuen, C. J. Foot, D. J. Owens, and J. M. Hutson. "Inelastic collisions in radiofrequency-dressed mixtures of ultracold atoms". In: *Phys. Rev. Res.* 2 (3 July 2020), p. 033163.

[108] A. J. Barker, S. Sunami, D. Garrick, A. Beregi, K. Luksch, E. Bentine, and C. J. Foot. "Realising a species-selective double well with multiple-radiofrequency-dressed potentials". In: *J. Phys. B: At. Mol. Opt. Phys.* 53.15 (June 2020), p. 155001. ISSN: 0953-4075.

[109] K. Luksch, E. Bentine, A. J. Barker, S. Sunami, T. L. Harte, B. Yuen, and C. J. Foot. "Probing multiple-frequency atom-photon interactions with ultracold atoms". In: *New J. Phys.* 21.7 (July 2019), p. 073067. ISSN: 1367-2630.

[110] T. V. Zache, T. Schweigler, S. Erne, J. Schmiedmayer, and J. Berges. "Extracting the field theory description of a quantum many-body system from experimental data". In: *Phys. Rev. X* 10.1 (2020), p. 011020.

[111] T. Betz, S. Manz, R. Bücker, T. Berrada, C. Koller, G. Kazakov, I. E. Mazets, H.-P. Stimming, A. Perrin, T. Schumm, et al. "Two-point phase correlations of a one-dimensional bosonic Josephson junction". In: *Phys. Rev. Lett.* 106.2 (2011), p. 020407.

[112] G. Hechenblaikner, J. M. Krueger, and C. J. Foot. "Properties of quasi-two-dimensional condensates in highly anisotropic traps". In: *Phys. Rev. A* 71 (1 Jan. 2005), p. 013604.

[113] W. Bao, D. Jaksch, and P. A. Markowich. "Numerical solution of the Gross–Pitaevskii equation for Bose–Einstein condensation". In: *J. Comput. Phys.* 187.1 (2003), pp. 318–342. ISSN: 0021-9991.

[114] D. Ananikian and T. Bergeman. "Gross-Pitaevskii equation for Bose particles in a double-well potential: Two-mode models and beyond". In: *Phys. Rev. A* 73 (1 Jan. 2006), p. 013604.

[115] C. Mora and Y. Castin. "Extension of Bogoliubov theory to quasicondensates". In: *Phys. Rev. A* 67 (5 May 2003), p. 053615.

[116] V. P. Singh, C. Weitenberg, J. Dalibard, and L. Mathey. "Superfluidity and relaxation dynamics of a laser-stirred two-dimensional Bose gas". In: *Phys. Rev. A* 95 (4 Apr. 2017), p. 043631.

[117] V. P. Singh, L. Amico, and L. Mathey. "Thermal suppression of demixing dynamics in a binary condensate". In: *Phys. Rev. Res.* 5 (4 Oct. 2023), p. 043042.

[118] B. Allard, T. Plisson, M. Holzmann, G. Salomon, A. Aspect, P. Bouyer, and T. Bourdel. "Effect of disorder close to the superfluid transition in a two-dimensional Bose gas". In: *Phys. Rev. A* 85.3 (2012), p. 033602.

[119] G. Astrakharchik, K. Krutitsky, and P. Navez. "Phase diagram of quasi-two-dimensional bosons in a laser-speckle potential". In: *Phys. Rev. A* 87.6 (2013), p. 061601.

[120] T. Scoquart, D. Delande, and N. Cherroret. "Dynamical emergence of a Kosterlitz-Thouless transition in a disordered Bose gas following a quench". In: *Phys. Rev. A* 106.2 (2022), p. L021301.

[121] K. T. Geier, J. Maki, A. Biella, F. Dalfovo, S. Giorgini, and S. Stringari. "Superfluidity and sound propagation in disordered Bose gases". In: *Phys. Rev. Res.* 7.1 (2025), p. 013187.

[122] J. Saliba, P. Lugan, and V. Savona. "Superfluid-insulator transition of two-dimensional disordered Bose gases". In: *Phys. Rev. A* 90.3 (2014), p. 031603.

[123] K. D. Bonin and M. Kadar-Kallen. "Simple diffuser for production of laser speckle". In: *Applied Optics* 28.24 (1989), pp. 5293–5297.

[124] B. R. De Abreu, U. Ray, S. A. Vitiello, and D. M. Ceperley. "Properties of the superfluid in the disordered Bose-Hubbard model". In: *Phys. Rev. A* 98.2 (2018), p. 023628.

[125] J. W. Goodman and p. Society of Photo-optical Instrumentation Engineers. *Speckle phenomena in optics : theory and applications*. eng. Second edition. SPIE Press monograph ; PM312. Bellingham, Washington: SPIE Press, 2020. ISBN: 1-5106-3149-6.

[126] M. Beeler, M. Reed, T. Hong, and S. Rolston. "Disorder-driven loss of phase coherence in a quasi-2D cold atom system". In: *New Journal of Physics* 14.7 (2012), p. 073024.

[127] G. Carleo, G. Boéris, M. Holzmann, and L. Sanchez-Palencia. "Universal superfluid transition and transport properties of two-dimensional dirty bosons". In: *Phys. Rev. Lett.* 111.5 (2013), p. 050406.

[128] P. W. Anderson et al. "Absence of diffusion in certain random lattices". In: *Phys. Rev.* 109.5 (1958), pp. 1492–1505.

[129] N. Trivedi and M. Makivić. "Dirty Bosons in 2D: Phases and Phase Transitions". In: *Quantum Monte Carlo Methods in Condensed Matter Physics*. World Scientific, 1993, pp. 317–337.

[130] M. Wallin, E. S. So, S. Girvin, A. Young, et al. "Superconductor-insulator transition in two-dimensional dirty boson systems". In: *Phys. Rev. B* 49.17 (1994), p. 12115.

[131] G. Grynberg, A. Aspect, and C. Fabre. *Introduction to quantum optics: from the semi-classical approach to quantized light*. Cambridge university press, 2010.

[132] W. Krauth, N. Trivedi, and D. Ceperley. "Superfluid-insulator transition in disordered boson systems". In: *Phys. Rev. Lett.* 67.17 (1991), p. 2307.

[133] Ş. G. Söyler, M. Kiselev, N. V. Prokof'ev, and B. V. Svistunov. "Phase diagram of the commensurate two-dimensional disordered Bose-Hubbard model". In: *Phys. Rev. Lett.* 107.18 (2011), p. 185301.

[134] L. Villa. "Out-of-equilibrium dynamics and quench spectroscopy of ultracold many-body quantum systems". PhD thesis. Institut Polytechnique de Paris, 2021.

[135] M. Sbroscia, K. Viebahn, E. Carter, J.-C. Yu, A. Gaunt, and U. Schneider. "Observing localization in a 2D quasicrystalline optical lattice". In: *Phys. Rev. Lett.* 125.20 (2020), p. 200604.

[136] R. Gautier, H. Yao, and L. Sanchez-Palencia. "Strongly interacting bosons in a two-dimensional quasicrystal lattice". In: *Phys. Rev. Lett.* 126.11 (2021), p. 110401.

[137] T. Bourdel. "Phase diagrams of two-dimensional and three-dimensional disordered Bose gases in the local density approximation". In: *Phys. Rev. A* 86.6 (2012), p. 063626.

[138] A. Lunkin, N. S. Ticea, S. Kumar, C. Miao, J. Choi, M. Alghadeer, I. Drozdov, D. Abanin, A. Abbas, R. Acharya, et al. "Evidence for a two-dimensional quantum glass state at high temperatures". In: *arXiv preprint arXiv:2601.01309* (2026).

[139] T. Scoquart. "Out-of-equilibrium dynamics and thermalization of weakly interacting disordered Bose gases". PhD thesis. Sorbonne Université, 2021.

[140] I. Maccari, N. Defenu, L. Benfatto, C. Castellani, and T. Enss. "Interplay of spin waves and vortices in the two-dimensional XY model at small vortex-core energy". In: *Phys. Rev. B* 102 (10 Sept. 2020), p. 104505.

[141] J. A. Nelder and R. Mead. "A simplex method for function minimization". In: *The Computer Journal* 7.4 (1965), pp. 308–313.

[142] A. Beregi, E. Chang, E. Rydow, C. J. Foot, and S. Sunami. "Universal non-Gaussian order parameter statistics in 2D superfluids". In: *arXiv preprint arXiv:2601.16204* (2026).

[143] J. Colbois, N. Chepiga, S. Adam, G. Lemarié, and N. Laflorencie. "Extreme statistics as a probe of the superfluid to Bose-glass Berezinskii-Kosterlitz-Thouless transition". In: *arXiv preprint arXiv:2512.09029* (2025).

[144] H. Meier and M. Wallin. "Quantum critical dynamics simulation of dirty boson systems". In: *Phys. Rev. Lett.* 108.5 (2012), p. 055701.

[145] J. P. Álvarez Zúñiga, D. J. Luitz, G. Lemarié, and N. Laflorencie. "Critical properties of the superfluid—bose-glass transition in two dimensions". In: *Phys. Rev. Lett.* 114.15 (2015), p. 155301.

[146] T. Murtadho, M. Gluza, and N. H. Ng. "Extensive entanglement between coupled Tomonaga-Luttinger liquids in and out of equilibrium". In: *arXiv preprint arXiv:2508.20533* (2025).

[147] V. Gondret, R. Dias, C. Lamirault, L. Camier, A. Micheli, C. Leprince, Q. Marolleau, S. Robertson, D. Boiron, and C. I. Westbrook. "Parametric pair production of collective excitations in a Bose–Einstein condensate". In: *Comptes Rendus. Physique* 25.S2 (2024), pp. 1–15.

[148] M. Tajik, I. Kukuljan, S. Sotiriadis, B. Rauer, T. Schweigler, F. Cataldini, J. Sabino, F. Møller, P. Schüttelkopf, S.-C. Ji, et al. "Verification of the area law of mutual information in a quantum field simulator". In: *Nature Physics* 19.7 (2023), pp. 1022–1026.

[149] N. Goldman and J. Dalibard. "Periodically driven quantum systems: Effective Hamiltonians and engineered gauge fields". In: *Phys. Rev. X* 4.3 (2014), p. 031027.

[150] A. Weinrib and B. I. Halperin. "Critical phenomena in systems with long-range-correlated quenched disorder". In: *Phys. Rev. B* 27.1 (1983), p. 413.

[151] W. Wang, H. Meier, J. Lidmar, and M. Wallin. "Three-dimensional universality class of the Ising model with power-law correlated critical disorder". In: *Phys. Rev. B* 100.14 (2019), p. 144204.